MSc thesis in Materials Science and Engineering

Understanding the corrosion behaviour of 7XXX series aluminium alloys under galvanic corrosion conditions

Tom Hautvast

2021

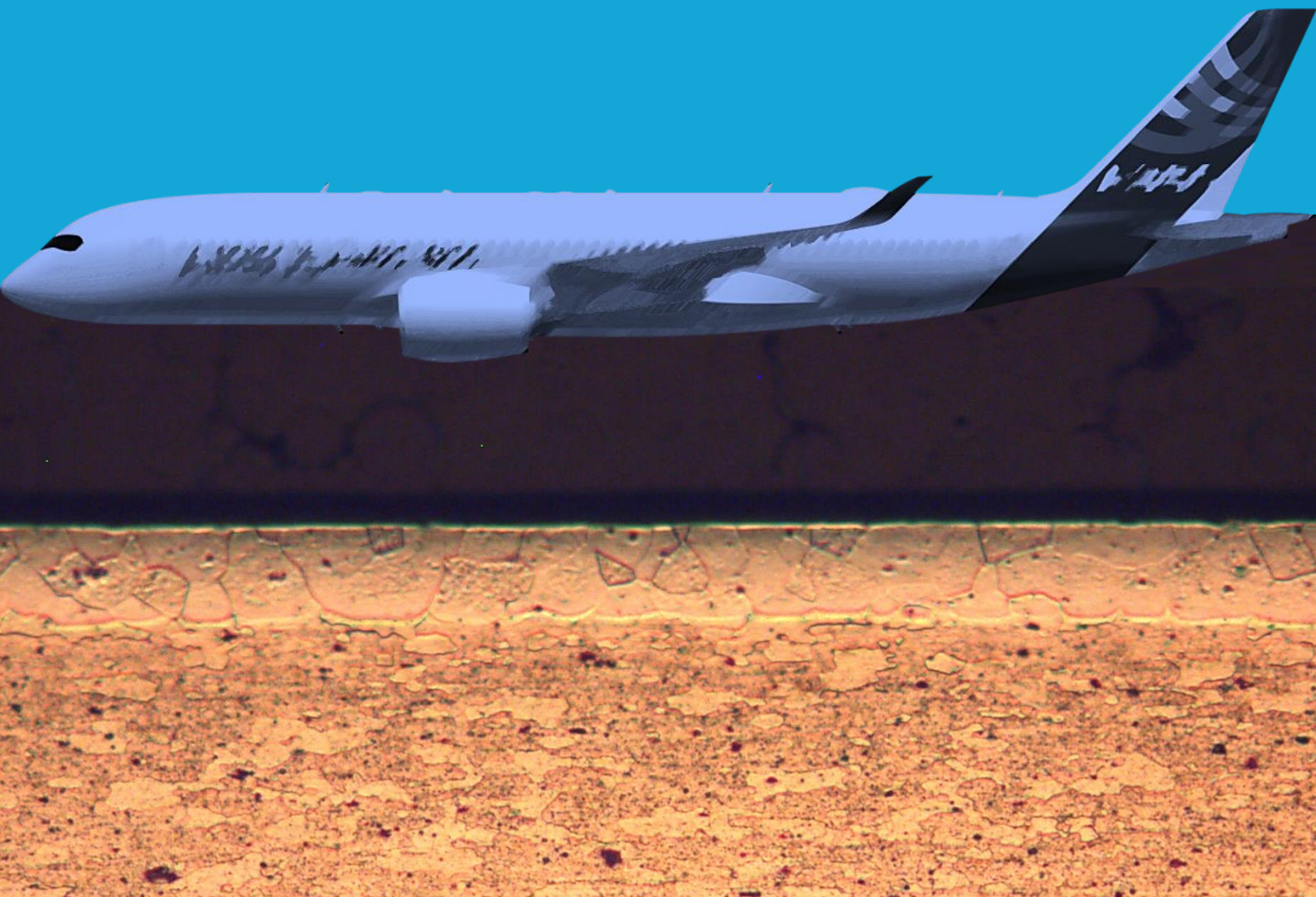

UNDERSTANDING THE CORROSION BEHAVIOUR OF 7XXX SERIES ALUMINIUM ALLOYS UNDER GALVANIC CORROSION CONDITIONS

A thesis submitted to the Delft University of Technology in partial fulfillment of the requirements for the degree of:

Master of Science in Materials Science and Engineering

by

Tom Hautvast

December 2021

Tom Hautvast: *Understanding the corrosion behaviour of 7XXX series aluminium alloys under galvanic corrosion conditions* (2021)
An electronic version of this thesis is available at:
http://repository.tudelft.nl/.

Thesis Committee:	Ir. Can Özkan Dr. Peyman Taheri Dr. Peter Visser Prof. dr. ir. J.M.C Mol
Supervisors:	Dr. Peter Visser Prof. dr. ir. J.M.C Mol

All experiments were performed in:

AkzoNobel
Expertise Center Corrosion,
Rijksstraatweg 31, 2171 AJ Sassenheim,
The Netherlands

Delft University of Technology
Department of Materials Science and Engineering
Merkelweg 2, 2628 CD Delft,
The Netherlands

This research was carried out under a research collaboration agreement between AkzoNobel and Delft University of Technology in the Netherlands.

ABSTRACT

For decades, developments towards a chromate-free protective system have been a crucial quest in the aerospace industry. In this search, innovation starts with a comprehensive understanding of the aircraft complex multi-material structures and the corrosion mechanisms involved. These complex structures, with aluminium being the most dominant substrate, are used to optimize the strength-to-weight ratio, fatigue properties and operational performance in aircraft design. On the other hand, the use of multi-materials can cause an accelerated corrosion attack when two or more dissimilar materials are placed in electrical contact in the presence of an electrolyte. This type of corrosion can be advantageously applied to galvanically protect a material but can also occur undesirably with serious accelerated degradation as result.

This thesis aims to increase our understanding of corrosion on AA7XXXClad alloys as stand-alone material, as well as in configurations relevant for galvanic corrosion with other metals. The understanding of these phenomena should support the definition of new hypotheses on how these alloys can be better protected using chromate-free coating technologies. Two commonly used aluminium alloys in the aerospace industry, AA7075C-T6 and AA7475C-T76, have been investigated in this study because a selective dissolution of the clad layer material was observed under galvanic corrosion conditions. The microstructure was investigated using optical microscopy (OM) and energy dispersive X-ray spectroscopy (EDS). This was combined with electrochemical experiments including open-circuit potential measurements (OCP), potentiodynamic polarization (PP), linear polarization resistance (LPR), electrochemical impedance spectroscopy (EIS), electrochemical noise measurement in zero resistance ammeter mode (ECN-ZRA), potentiostatic polarization (PSP) and galvanostatic polarization (GSP). In addition, Neutral Salt Spray (NSS) tests were used to compare the efficiency of the inhibitor coatings in an artificially created defect area, and in-situ experiments were performed to observe the sequence of dissolution caused by corrosion in detail.

Zinc is the main alloying element in AA7075C and AA7475C, therefore the role of zinc in the clad layer with respect to corrosion initiation and propagation was first investigated. It was shown that zinc in the clad layer decreases the equilibrium potential and increases the corrosion rate. Also, that pure zinc preferentially dissolves when it is placed in electrical contact with pure aluminium in the presence of the electrolyte used. In the clad layer of AA7075C and AA7475C, a distribution of alloying elements from the substrate to the clad surface was measured, with an increased amount of zinc in the region along the substrate and clad layer interface than the theoretical maximum reported. This means that a transition region is present in the clad layer that may be held responsible for the selective dissolution observed. Subsequently, the behaviour of clad alloys under galvanic corrosion conditions was investigated. An experimental procedure was designed to measure the coupled galvanic parameters and to simulate galvanic corrosion degradation. While simulation of the selective dissolution phenomenon has been partially shown with in-situ experiments, it is not fully observed. Finally, it was investigated how inhibition under galvanic conditions can be assessed reliably. To test the performance of corrosion inhibitors, a procedure is developed with and without the use of coatings. Generally, it can be concluded that limiting the cathodic reactions is of paramount importance to reduce the galvanic corrosion current.

PREFACE

Writing this acknowledgment feels like the end of an amazing journey. And truly, this was indeed an unforgettable experience in many ways. On the other hand, it feels like the start of an exciting new adventure and I'm all set to follow this path with the knowledge and experiences I've gained over the years.

First of all, I would like to thank everyone who helped me during this MSc journey and in particular with my graduation project. Especially, my supervisors Arjan Mol and Peter Visser for guiding me through this very interesting experience in both the academic and industrial field. Thank you both for this opportunity, scientific input, interesting discussions, and the always positive support from beginning to end. Besides, I want to thank Peyman Taheri and Can Özkan for joining my thesis committee and the effort they put into my graduation. Furthermore, the employees, lab technicians and colleagues at the Delft University of Technology and AkzoNobel whom helped me with all sort of questions about sample preparations and the experiments performed, but also for the "coffee moments" and conversations about anything and everything.

Also, I would like to thank my friends and roommates for the unforgettable and fantastic moments during this MSc journey. Finally and most of all, I wish to thank my family, my mom, my dad, brothers and sister for the strong, continuous support in my life, and last but not least, my girlfriend, who always supported me no matter how far the travel distance was.

Tom Hautvast
Delft, December 2021

CONTENTS

LIST OF FIGURES

LIST OF TABLES

ACRONYMS

BEC	Backscattered Electron Composition	45
BTA	Benzotriazole	33
CCC	Chromate Conversion Coating	23
CE	Counter electrode	34
ECN	Electrochemical Noise	37
EIS	Electrochemical Impedance Spectroscopy	32
HF	Hydrofluoric acid	26
H_2SO_4	Sulfuric acid	26
KCl	Potassium chloride	33
LPR	Linear Polarization Resistance	32
NSS	Neutral Salt Spray	2
OCP	Open Circuit Potential	25
OP-S	Oxide Polishing Suspension	26
PP	Potentiodynamic polarization	25
RE	Reference electrode	25
SEC	Secondary Electron Composition	83
SEM	Scanning Electron Microscopy	26
SEM-EDS	Scanning Electron Microscopy with Energy Dispersive X-Ray Spectroscopy	3
TSA	Tartaric Sulphuric Acid anodising	2
WE	Working electrode	25
ZRA	Zero Resistance Ammeter	29
2-MBT	2-mercaptobenzothiazole	33

1 INTRODUCTION

1.1 BACKGROUND AND INDUSTRIAL RELEVANCE

High strength aluminium alloys are widely used for the design of aircraft due to their lightweight properties and high strength-to-weight ratio. Especially wrought aluminium alloys, such as AA2024 and AA7075 are commonly used alloys in the aerospace industry. AA2024 for instance, is used for the fuselage skin and frame along with other structural parts. AA7075 mainly for a wide variety of structural parts, such as wing skin panels and extruded stringers in the belly of the aircraft. The desired material properties for a specific structural part can be achieved by the addition of alloying elements in combination with specific mechanical and thermal treatments. However, this addition also makes the material more susceptible to corrosion, because during thermal processes, second phase particles can form from alloying elements and impurities in the material, thereby creating galvanic couplings within the aluminium matrix. In addition, these galvanic couplings can occur on a macro-scale by the use of dissimilar materials, which can be two different alloys or metals, but also a metal and composite (e.g. aluminium and carbon fibre-epoxy laminate). To manufacture an airplane for instance, about 100 different materials are used in the engines and air-frame of an aircraft alone [1]. When two or more of these dissimilar materials come in electrical contact in the presence of an electrolyte, an accelerated corrosion initiation is stimulated.

To protect the aluminium alloy substrate from corrosion, a protection scheme can be used. A protection scheme in the aerospace industry consists of two or three layers, which typically is a pre-treatment on top of the aluminium alloy substrate and an active protective coating system. The primary function of such protection scheme is to act as a passive barrier between the substrate and the environment, but when the protection scheme is damaged it also needs to provide active corrosion protection. This means that when a damaged area occurs and the substrate is exposed to the environment, a corrosion inhibitor will dissolve from the coating due to moisture ingress and will be transported to the exposed area to form a new protective barrier layer.

For more than the last three decades, the aerospace industry has been relying on hexavalent chromate as an active corrosion inhibitor. Chromates have a proven track record of being very versatile and active at low concentrations, various environmental conditions and on different substrates. However, due to their toxic and carcinogenic nature, further use is being restricted by new legislations. In the search of new corrosion inhibitors, more and more environmentally friendly inhibitor strategies have been developed and investigated as an alternative for chromates. Very promising candidates have been identified over years, but the new chromate-free alternative inhibitors are in general not as versatile as the traditional chromate technology. Moreover, this research focused mainly on AA2XXX because of its susceptibility to pitting corrosion. Though, AA7XXX alloys are used in significant quantities as well and the corrosion phenomena are rather different compared to AA2XXX. While new chromate-free technologies perform very well on AA2XXX in a range of tests, results have shown different protective performance on AA7XXX, meaning that the new chromate-free technologies are less robust compared to the benchmark,

chromates. For this reason, it is fundamental to increase the understanding of corrosion degradation and protection on AA7XXXC as stand-alone material as well as in configurations relevant for galvanic corrosion. Finally, the understanding of these phenomena should support the definitions of new hypotheses on how these alloys can be reliable and robust protected by using chromate-free coating technologies.

1.2 RESEARCH OBJECTIVES AND EXPERIMENTAL APPROACH

Corrosion occurs in many forms and combinations on the aircraft structure, e.g. pitting corrosion, intergranular corrosion, exfoliation corrosion, filiform corrosion, crevice corrosion and galvanic corrosion. These complex phenomena, although mechanistically different, are similar in terms of their possible effects in reducing the structural integrity. Lately, an filiform-like corrosion was observed around AA2017A-T4 fasteners on AA7475CTSA-T76 after 3000h of Neutral Salt Spray (NSS) (ASTM B-117), which is shown in Figure 1.1. The material AA7475CTSA consists of AA7475 as bulk material with a AA7072 clad layer on top of the aluminum alloy substrate and a Tartaric Sulphuric Acid anodising (TSA) layer applied on the clad surface.

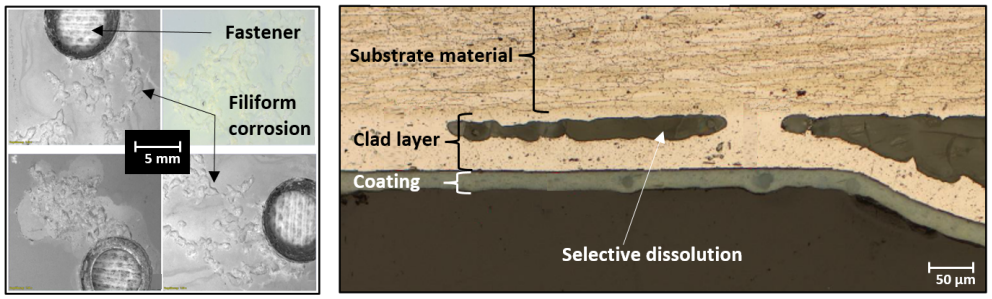

Figure 1.1: Corrosion phenomenon on AA7475CladTSA after 3000h of Neutral Salt Spray test.

On the top view in Figure 1.1 this phenomenon appears as a blister and worm-like degradation, initiating around the fastener heads and propagating away underneath the applied coating. From the cross-section view in Figure 1.1 it becomes clear that this corrosion propagation, and probably also the initiation, takes place through the clad layer especially along the interface of the aluminium alloy substrate. In addition, only selective dissolution of the clad layer is observable, which means that corrosion quickly can propagate through the clad material. Furthermore, with this corrosion process deeper in the clad layer, it is almost impossible to inhibit the corrosion process with the loaded corrosion inhibitors in the active protective coating. By observing this phenomenon, many question remain unclear. Therefore, this thesis aims to investigate three research questions to increase the understanding into the corrosion behaviour of 7XXXClad series aluminium alloys under galvanic corrosion conditions:

- What is the role of zinc in the Clad layer with respect to corrosion initiation and propagation?
- How do 7XXXClad alloys behave under galvanic corrosion conditions?
- How can inhibition under galvanic corrosion conditions be assessed reliably?

The objectives in this thesis were studied using a combination of electrochemical techniques and microscopy analysis to not only measure, but also observe the corrosion behaviour of the 7XXXC series aluminium alloys. In this study, two commonly used aluminium alloys in the aerospace industry, AA7075C-T6 and AA7475C-T76,

have been investigated and will be designated together as AA7X75C.

First the role of zinc in the clad layer was investigated. The electrochemical behaviour of commercially pure zinc and aluminium was measured by electrochemical experiments. Then, the aluminium alloys were investigated by microstructural analysis and the thickness of the clad layer was determined, followed by a line-scan using Scanning Electron Microscopy with Energy Dispersive X-Ray Spectroscopy (SEM-EDS) to examine a zinc distribution.

Second, the behaviour of 7X75C alloys under galvanic corrosion conditions was investigated. The main aim of this part was to measure the coupled parameters when using dissimilar materials, and to reproduce the galvanic corrosion degradation in a representative manner. Also, when accelerated experiments are desired to obtain faster results. This is performed by using a combination of electrochemical techniques and microscopic analysis.

Finally, the inhibition of AA7X75C alloys under galvanic corrosion conditions was investigated with and without the use of coatings. Various inhibiting coatings were applied to aluminum alloys with an artificially damaged area being created. By means of electrochemical experiments, the inhibitor performance in the defect area was examined before and after exposure to a external fastener. In this way, the inhibition performance of the different inhibitor coatings was assessed while being galvanically stimulated. Galvanic inhibition without coatings has been assessed using commonly used solutions of organic inhibitor compounds. The inhibition of the galvanic current was measured by electrochemical experiments. The anodic and cathodic inhibition efficiency were also measured separately using a salt bridge.

1.3 OUTLINE

The outline of this thesis is schematically represented in Figure 1.2, and consists of five chapters in total. An introduction to the background of the research questions and approach is presented in Chapter 1. Chapter 2 provides the reader with fundamental "state of the art" background and theory on the thesis topic. This chapter is divided into five main sections, in which the alloy designation, microstructure, corrosion mechanisms and corrosion protection technologies are discussed and summarized for AA7075 that are relevant to this thesis. Chapter 3 evaluates the materials and methods used in this work, including the sample preparation strategies and parameters relevant to the characterization techniques used. Chapter 4 discusses the results of this study by the three main objectives, as explained in Section 1.2. Finally, this thesis report ends with Chapter 5 that accommodates the conclusions and recommendations for further research of this work.

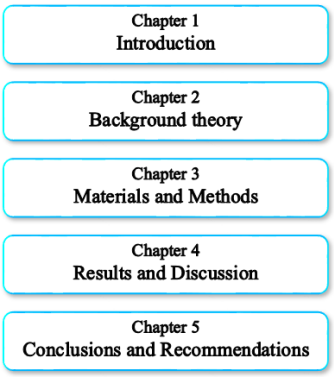

Figure 1.2: Graphic representation of the thesis outline

2 BACKGROUND THEORY

This chapter discusses the "state of the art" background that increases the understanding of AA7075, providing a solid foundation for this thesis. This section starts with an introduction about aluminium alloy designation, followed by an overview of their typical microstructure with the focus on second phase particles, as their influence is the main contributor to the overall corrosion behaviour. Next, the most common corrosion mechanisms are described, both corrosion initiation and propagation. Understanding these mechanisms is essential for the protection of a material when a damaged area is formed. Finally, this chapter evaluates several protective technologies which are relevant for this thesis and summarizes with conclusions the main findings of this literature study.

2.1 ALLOY DESIGNATION

For legacy aircraft, wrought high strength aluminium alloys such as AA2024 and AA7075 are the most commonly used alloys for a wide variety of structural parts [2]. According to the American National Standards Institute (ANSI) standard H35.1 [3], wrought aluminium alloys are classified with a four-digit system. The first digit indicates the main alloying element of the aluminium alloy, as in the case of AA7XXX the element is zinc, whereas for AA2XXX it is the element copper. The second digit from one to nine represents an alloy modification of the original alloy indicated with zero, and the last two digits identify the different alloying elements in the particular aluminium series [4]. After the aluminium alloy designation, a heat treatment (temper) can be indicated. In the case of AA7075-T6 this represents a solution heat treatment followed by an artificially aged temper, whereas for AA2024-T3 this corresponds to a solution heat treated, cold worked and naturally aged temper [4; 2].

2.2 MICROSTRUCTURE

The addition of alloying elements to aluminium significantly improves the strength-to-weight ratio, which is an important term in the design phase of the aerospace industry [5; 6; 7]. Unfortunately, this addition creates a heterogeneous microstructure, inherently making the material more susceptible to localized corrosion phenomena. The corrosion susceptibility increases because second phase particles can form from alloying elements and impurities in the material during thermal processes, thereby creating galvanic couplings in the aluminium matrix. The formed second phase particles differ in size, chemical composition and influence on the microstructure, therefore they are divided into three main groups namely intermetallics, strengthening particles and dispersoids [4]. The intermetallics are also referred as constituent particles in literature. In this study, the term intermetallic is always used.

2.2.1 Intermetallic particles

Intermetallic particles are formed during ingot casting by interaction of alloying elements and impurities (e.g. Fe and Si) present in the aluminium alloy, with a size varying between 1 µm and 20 µm [4]. Intermetallics are insoluble during solution heat treatment and aging processes, meaning that their size, morphology, density and composition does not change [8; 4; 9]. However, they can change their morphology and undergo phase transformation during ingot homogenisation [8; 9].

Over the years, the chemical composition of intermetallics in AA7075 has been studied extensively. Ayer et al. (1985) found in their study the highest abundance for Al_7Cu_2Fe, $(Al,Cu)_6(Fe,Cu)$ and Mg_2Si as intermetallic compounds. In minor amounts, intermetallic particles such as Al_6Fe, $Al_{12}Fe_3Si$ and amorphous silicon oxide were also identified [9]. Gao et al. (1998) found only $(Al,Cu)_6(Fe,Cu)$ (reffered as $Al_{23}CuFe_4$) and small amounts of silicon oxide intermetallics in AA7075-T6 [10]. Later, Andreatta et al. (2003) studied solution heat treated and aged AA7075, and identified three types of intermetallics with a chemical composition of Al_7Cu_2Fe, $(Al,Cu)_6(Fe,Cu)$ / $Al_{23}CuFe_4$ and Mg_2Si, which are shown in Figure 2.1. Among the classified intermetallics in AA7075, the Fe- and Cu-rich intermetallics are observed to be present in higher quantities than the Mg_2Si intermetallics [9; 8]. Birbilis and Buchheit (2005) measured the current of 21 intermetallic compounds at the corrosion potential of AA7075-T651 and found the largest cathodic current among these particles for Al_7Cu_2Fe. They concluded therefore that this particle type should be on the watch list regarding the corrosion kinetics when present in the aluminium alloy [11]. With the use of characterization techniques, Cavanaugh et al. (2009) found that Al_7Cu_2Fe was the most abundant one($>$ 50%) in the overall particle population in AA7075-T651 [12]. Additionally, they found that the rest of the particle population was mainly consisting of Mg_2Si and Al_3Fe, followed by a smaller quantity of Al_2CuMg.

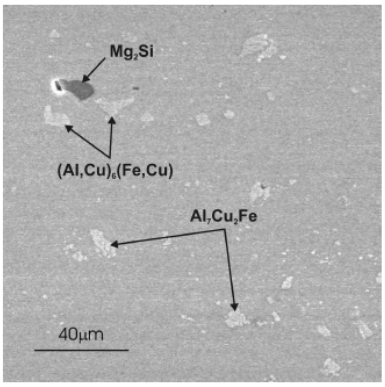

Figure 2.1: The most abundant intermetallics in AA7075 found by Ayer et al. [9]

To investigate the influence of intermetallic particles on the corrosion behaviour of AA7075, Andreatta et al. (2003) studied the galvanic coupling between the most abundant intermetallics and the aluminium matrix by measuring the difference in Volta potential in as received AA7075-T6 and solution heat treated AA7075 [8]. They measured an increase in potential when the material was solution heat treated for Al_7Cu_2Fe, $(Al,Cu)_6(Fe,Cu)$ and Mg_2Si, and explained this by the dissolution of strengthening particles which promotes the anodic behaviour of the matrix, thereby increasing the galvanic coupling between the intermetallic particles and the matrix. The intermetallics that are Fe- and Cu-rich were found to have a positive Volta potential in the as received and solution heat treated aluminium, which corresponds to a cathodic behaviour of these intermetallics with respect to the aluminium matrix. Moreover, the greater amount of Cu in Al_7Cu_2Fe results in the strongest galvanic

coupling among the intermetallics and the aluminium matrix, because Cu is found to be more noble than Fe. Furthermore, a shift from a negative- to a positive potential with respect to the matrix is measured at Mg_2Si, which means that this type of intermetallic can change its electrochemical behaviour during the solution heat treatment from anodic to cathodic [8]. In a subsequent research, Andreatta et al. (2003) studied the local electrochemical behaviour of intermetallics by using SKPFM and a micro-capillary cell [13]. A similar trend was found in the galvanic coupling between the intermetallics and the matrix, and the local electrochemical behaviour of the intermetallics during potentiodynamic polarisation. It was concluded that the Volta potential difference between the intermetallics and the surrounding matrix is related to the breakdown potential of areas containing these intermetallic particles. More specifically this means that a higher Volta potential difference between the intermetallic and the matrix causes a more cathodic breakdown potential in both solution heat treated and aged AA7075.

2.2.2 Strengthening particles

Strengthening particles are strongly affected by heat treatments and various tempers, which are used to improve the mechanical properties of AA7075 [4; 3]. For instance, the tensile properties of an aluminium alloy in a given temper are strongly dependent on the type, size and distribution of these particles. However, as mentioned before, these characteristics and compositional changes significantly affects the galvanic couplings in the aluminium matrix and thus the overall corrosion behaviour of the aluminium alloy [14].

Strengthening particles are a collection of precipitates that form during decomposition of a supersaturated solid solution in age hardenable aluminium alloys [14]. The sequence of decomposing in AA7075 is as followed [14; 15; 16; 17]:

$$\alpha_{ss} \rightarrow \alpha_1 + GPzones \rightarrow \alpha_2 + \eta' \rightarrow \alpha_{eq} + \eta \tag{2.1}$$

In this sequence, α_{ss} is the initial supersaturated solid solution. α_1 and α_2 are solid solutions with intermediate solute levels between α_{ss} and α_{eq}, where α_{eq} is the equilibrium solid solution. The first decomposition products are Guinier-Preston (GP) zones, which are nano-scaled fine solute rich clusters that are fully coherent with the matrix. These clusters are the first decomposing products that provides physical impediment to the movement of dislocations. Subsequently, η' and η phases are formed. Where η' is a metastable phase with metastable precipitates that is mostly semi-coherent with the matrix, whereas the η phase is the stable phase with equilibrium precipitates. This equilibrium phase is incoherent with the matrix and has a stoichiometric composition of $MgZn_2$ in AA7075-T6, while the stoichiometric composition of η' closely approximates this composition [16].

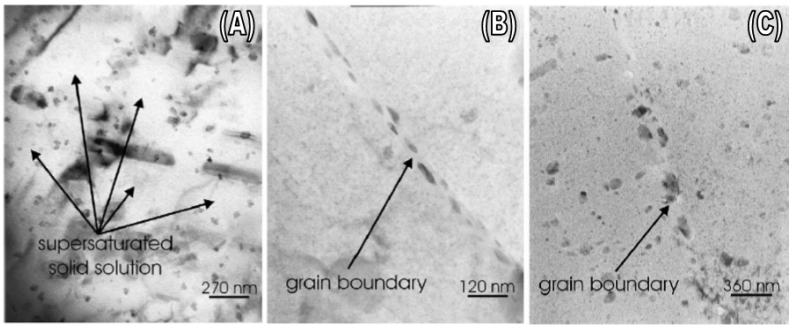

Figure 2.2: Strengthening particles in: (A) Solid solution AA7075, (B) Aged AA7075-T6, and (C) Overaged AA7075-T76. [18]

The influence on the microstructure by strengthening particles during heat treatments is explained with Figure 2.2. In this figure, three TEM micrographs of AA7075 with different tempers are presented. In Micrograph (A) the supersaturated solid solution is shown, which can be recognized by the relatively large areas without particles. In these regions, the supersaturated solid solution of the elements Mg and Zn results from the dissolution of the strengthening particles, $MgZn_2$, during the solution heat treatment. The supersaturation of Mg and Zn in the matrix causes segregation of these specific elements towards the grain boundaries, which in turn are preferential nucleation sites for these particles. The particles that are still visible around the areas without precipitates are probably intermetallic or dispersoids, which are not affected during heat treatments. Micrograph (B) shows AA7075 with an aged (T6) temper. During aging processes, high concentrations of very fine strengthening precipitates form in the matrix with sizes of a few nanometers [15]. In this temper, these precipitates are homogeneous distributed in the aluminium matrix and are mainly η' particles [16]. At the grain boundaries there are predominantly larger η phase particles present, with a size of approximately 50nm and an interparticle distance of roughly 30nm [18]. Micrograph (C) shows the strengthening particles of an overaged (T76) temper. Overaging causes coarsening of the strengthening particles in the matrix and at the grain boundaries, and reduces their overall concentration when compared to the T6 temper. Also, it increases the interparticle spacing.

The influence of strengthening particles on the electrochemical behaviour was studied by Andreatta et al. (2004) [18]. In Figure 2.3, an OCP graph is shown for three different tempers, namely solution heat treated AA7075 (SW60), aged AA7075-T6 and overaged AA7075-T76 in 3.5% NaCl solution with pH 4. The solution heat treated aluminium alloy after 10 minutes of measurement shows the most negative OCP (-0.810V) of all tempers measured. This observation can be explained by the presence of Zn and Mg in supersaturated solid solution, which shifts the OCP to a negative direction. By aging and overaging of the aluminium alloy, strengthening particles precipitate and causes a shift to a more positive potential. The OCP measured after 10 minutes for the aged T6 and overaged T76 temper is -0.790V and -0.770V, respectively. The largest positive shift caused by overaging is explained by the higher amount of Zn and Mg precipitates in the T76 temper compared to the aged T6 temper.

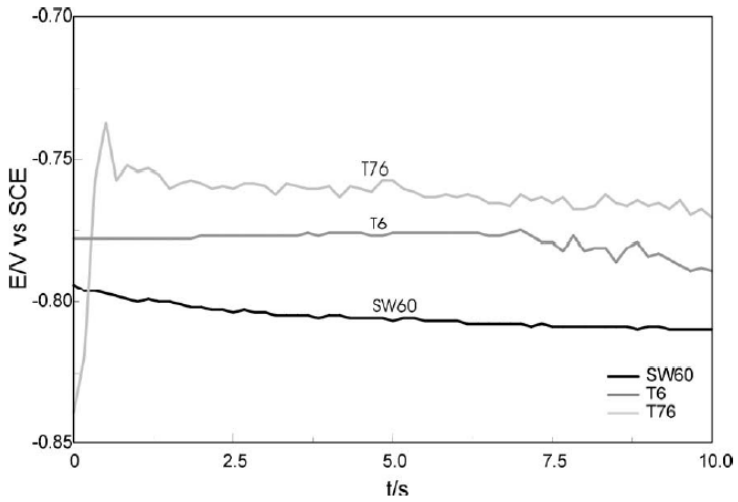

Figure 2.3: OCP measurement: for solution heat treated AA7075 (SW60), aged AA7075-T6 and overaged AA7075-T76. [18]

2.2.3 Dispersoids

Dispersoids are formed in 7xxx alloys during ingot homogenisation. Their formation takes place through the interaction of additives, such as Cr, Ti, Zr and Mn with alloying elements that are present in the aluminium alloy [4; 11]. When dispersoids precipitate, they are present to control the grain size and degree of recrystallization of the aluminium alloy [19; 9; 4]. According to Andreatta et al. (2004), dispersoids appear in typical sizes between 10 nm and 2 µm [4], while Birbilis and Buchheit (2005) describe the particle size more precise, ranging from 50 nm to 0.5 µm [11]. Ayer et al. (1985) found in Cr containing aluminium alloys, such as AA7075 and AA7475, dispersoids with a composition of $Al_{18}Mg_3Cr_2$. These dispersoids can slightly change their composition during heat treatments, because during overaging of AA7075 a decrease of zinc and a corresponding increase of aluminium in this type of dispersoid was observed [9].

The distribution of dispersoids is not completely clear from literature. Andreatta et al. (2004) report that dispersoids are not uniformly distributed in the microstructure because they precipitate directly from the as cast microstructure, which is characterised by the heterogeneous distribution of the elements forming dispersoids [4]. According to Birbilis and Buchheit (2005), dispersoids are homogeneously distributed in the aluminium matrix, because these particles form at high temperatures and control the grain size and recrystallization behavior of the alloy [11]. Therefore, no consensus has been found on the distribution of dispersoids between these studies.

Considering the influence on the electrochemical behaviour, dispersoids do not appear to have a significant direct effect on localized corrosion susceptibility in high-strength aluminium alloys due to their small size and comparative electrochemical inertness [11]. The second phase particles of particular interest are those which appear in the greatest proportion, either in frequency or by size. With regards to AA7X75 these particles have been identified as strengthening particles and intermetallics. Therefore, the affect of dispersoids on the electrochemical behaviour of AA7075 will not be discussed further in this report.

2.3 CORROSION MECHANISMS

Corrosion degradation is influenced by many metallurgical factors, for example the chemical composition of the alloying elements, heat treatments and material discontinuities, as well as environmental factors such as temperature, humidity, pH, time of exposure and type of electrolyte. In addition, rolling and extruding processes can create an elongated and anisotropic microstructure that may affect the corrosion kinetics [20]. A combination of these factors determines the dominant corrosion mechanisms for a specific alloy, which can eventually lead to failure of the material. Especially when chlorides are present, high strength aluminum alloys are susceptible to severe localized corrosion types, such as pitting, intergranular and exfoliation corrosion [21; 22; 4; 18]. Therefore, this chapter starts with a general discussion on the electrochemical behaviour of these corrosion types by means of potentiodynamic polarization curves. Followed by a more detailed review of these specific corrosion mechanisms. This chapter concludes with a brief study on filiform and galvanic corrosion, which are both common types of corrosion in aircraft structures when a coating is applied. It is important to mention that all metals, alloys and microstructural phases have a specific potential depending on the environmental conditions [23; 11; 24; 25]. The relative potential difference is the driving force behind the corrosion reactions and determines the direction of the reactions involved. When two metals or alloys are in electrical contact in the presents of an

electrolyte, the more noble material will act as the cathode and the more active material as the anode, causing it to dissolving preferentially. This can be observed in the galvanic series as shown in Figure 2.9.

The general discussion in this paragraph will mainly focus on the change in composition that causes differences in breakdown potentials. Heterogeneity that affects breakdown potentials such as surface roughness is discussed in a different study by [26], and the effect of various grain sizes was investigated by [20] and [27]. Further heterogeneity in the microstructure caused by crystallography features or residual stresses that can affect the corrosion behaviour is beyond the scope of this literature review, because the focus of this review part is on the galvanic interactions caused by second phase particles present in the microstructure.

Andreatta et al. (2004) investigated the initiation and propagation of localized corrosion mechanisms by means of breakdown potentials in a 3.5% NaCl solution (pH=4) [18]. The polarisation curves for solution heat treated AA7075 (SW60), aged AA7075-T6 and overaged AA7075-T76, are shown in Figure 2.4. The letters A through E in this figure correspond to the SW60 curve.

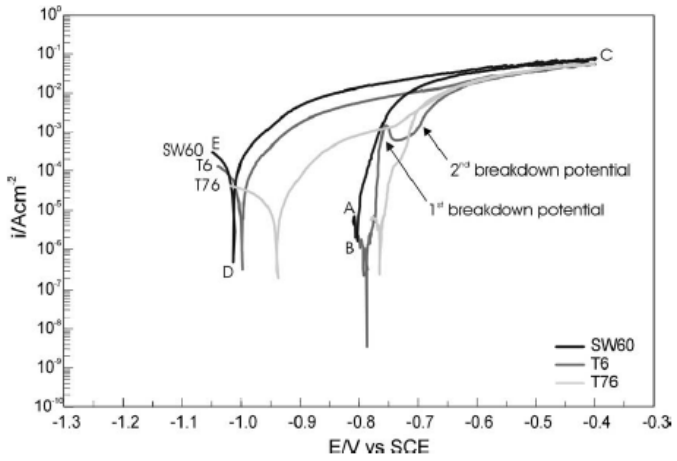

Figure 2.4: Potentiodynamic polarisation curves after ten-minutes of OCP measurement for: Solution heat treated AA7075 (SW60), aged AA7075-T6 and overaged AA7075-T76. [18]

In Figure 2.4, point B is the measured OCP of the solution heat treated AA7075 alloy with a value of -0.810V. Immediately after this point, a strong increase in current density is observed until the breakdown potential of AA7075 is reached. The measured OCP for AA7075-T6 and AA7075-T76 is -0.790V and -0.770V respectively. Unlike AA7075, two breakdown potentials are visible for aged AA7075-T6 and overaged AA7075-T76. In general, a breakdown potential corresponds to the dissolution potential of a phase in the aluminium alloy [28; 29]. More specifically, this means that when two breakdown potentials are observed, two phases with different dissolution potentials are present in the aluminium alloy microstructure, responsible for two forms of localized corrosion.

At the first breakdown potential of AA7075-T6, localized attack around Fe- and Cu-rich intermetallic particles was observed as a result of matrix dissolution. Larger pits were also found, probably formed by intermetallic particles that dropped out the surface or dissolved selectively (eg. Mg_2Si). After the second breakdown potential in this T6 temper, the presence of intergranular corrosion was observed which can turn into exfoliation corrosion during further polarisation. The high susceptibility to intergranular corrosion is caused by the high density of segregated particles

to the grain boundaries, as discussed in Section 2.2. Overaging to the T76 temper coarsens the strengthening particles and decreases their overall concentration, resulting in a higher resistance to intergranular corrosion and to possible exclusion of exfoliation. Since solution heat treated AA7075 contains only one breakdown potential, it would be expected that only dissolution of the matrix around the intermetallic particles will occur. However, this temper has been observed to have the highest susceptibility to intergranular and exfoliation corrosion, which means that probably both breakdown potentials are superimposed.

Above all breakdown potentials in Figure 2.4, the current density becomes fairly constant, indicated with point C. This point corresponds to the maximum dissolution rate of the aluminium alloys, which is known as the limit anodic current density. At this point, it can be observed that the anodic current density for AA7075 is slightly higher than that of the T6- and T76 temper. During the polarisation backwards scan, the current density is also the highest for solution heat treated alloy, and the OCP in the backwards scan (point D) is more negative than the OCP in the forward scan for all tempers caused by the amount of corrosion degradation of the alloys during the forward scan. Moreover, the most negative OCP in the backward scan is observed for the solution heat treated temper. Therefore, the authors suggested that the solution heat treated AA7075 has the highest susceptibility to localised corrosion compared with the T6 and T76 tempers.

Micrographs and cross-sections of the exposed area after a complete potentiodynamic polarisation measurement (Figure 2.4: point E) were created, and are shown in Figure 2.5 for solution heat treated (A and B), aged (C and D) and overaged (E and F) AA7075. These images show in all tempers severe localised corrosion attack. Especially, in the solution heat treated alloy where the most severe degradation can be observed. According to the article, the overaged T76 temper (image F) became immune to exfoliation corrosion and underwent intergranular corrosion, while AA7075 and AA7075-T6 are highly susceptible to exfoliation corrosion [18].

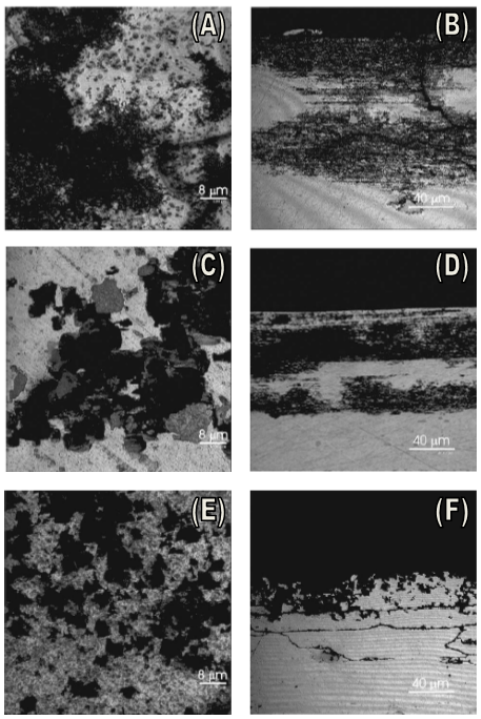

Figure 2.5: Micrographs (A,C,E) and cross-sections (B,D,F) of the exposed area after potentiodynamic polarisation for solution heat treated AA7075 (A and B), aged AA7075-T6 (C and D) and overaged AA7075-T76 (E and F). [18]

2.3.1 Pitting corrosion

Pitting corrosion is a severe form of localized attack that occurs when a passive film breaks down in the present of an electrolyte [30]. This results in local dissolution and pit formation of the metallic surface, which can appear in many forms as can be seen in Figure 2.6a. In AA7075, pitting corrosion initiates around local intermetallic particles, as shown in Figure 2.6b [21; 31]. Intermetallic particles are able to form galvanic couplings with the surrounding aluminium matrix and are either cathodic or anodic with respect to the matrix [8]. As discussed in Section 2.2, Fe- and Cu-rich intermetallics are cathodic in both solution heat treated and aged AA7075, thereby promoting dissolution of the aluminium matrix. The intermetallic particles consisting of Mg_2Si also behave cathodically with respect to the matrix during solution heat treatment, but becomes anodic upon precipitation of the strengthening particles during aging, causing them to preferentially dissolve [22].

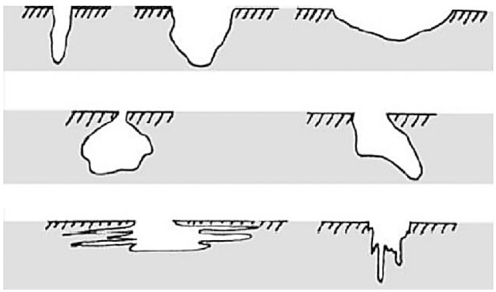

(a)

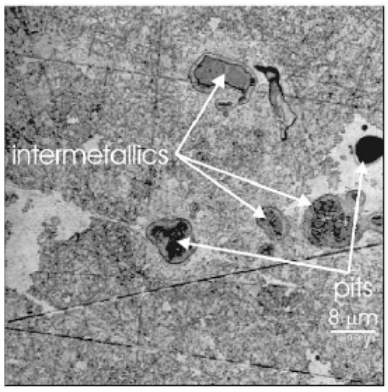

(b)

Figure 2.6: (a) Various forms of pitting corrosion [32]; (b) Pitting and dissolution of the AA7075-T6 matrix around intermetallic particles at the first breakdown potential (Figure 2.4) after 10 min of OCP measurement in 3.5% NaCl [18].

In general, the potential difference between the intermetallic particles and the matrix is the driving force behind the development of pitting corrosion [4; 33]. The current path involves electron exchange across the intermetallic/matrix interface by metallic conduction, and ionic exchange through the electrolyte. The current between the intermetallic particles and the matrix due to the galvanic coupling depends on the cathodic to anodic ratio between the intermetallics and the matrix, which is strongly determined by the size of surface areas [22]. The area of the intermetallic particles relative to the matrix is small. This means that the cathodic to anodic ratio is small too. Hence, the current in the galvanic coupling between the intermetallics and the matrix in AA7075 is limited by the cathodic current density. When the intermetallic particles grow in size, the cathodic current also increases, resulting in an increase of dissolution rate of the matrix around the intermetallic particles. According to Wei et al. (1998) this localized corrosion attack around the intermetallic particles can exceed a radius of 5 times the intermetallic particle size and is therefore able to expose other intermetallics to the electrolyte, resulting in more severe pitting corrosion [21]. Moreover, this means that if the density of intermetallic particles (e.g. closely spaced or clusters) is high, large and severe pitting may occur more easily.

The galvanic behaviour of various intermetallic particles is also studied by Cavanaugh et al. (2009), where pitting corrosion is investigated on AA7075-T651 and key parameters of the predominant intermetallic particles regards localized corrosion were measured in a 0.1M NaCl solution [12]. In this study, the intermetallic Al_7Cu_2Fe is considered as the primary contributor to large pits formation, because

of its electrochemical characteristics and high abundance in the aluminium matrix. In addition, the active particles relative to the matrix (e.g. Mg_2Si and $MgZn_2$) were found to dissolve fast, thereby leaving small but passivated pits that are not deeply penetrated into the substrate.

Birbilis and Buchheit (2005) investigated corrosion potentials and electrochemical characteristics for second phase particles in high-strength aluminium alloys [11]. The average current of the tested particles was measured at the corrosion potential of AA7075-T6 in 0.1M NaCl. The largest anodic current among the investigated particles was detected at $MgZn_2$, and the largest cathodic currents at Al_7Cu_2Fe and Al_2Cu. Therefore, these particles should be the watch list with regard to the corrosion kinetics when they are present in the aluminium alloy. Other commonly intermetallic particles in AA7075, as discussed in Section 2.2 were also found and measured by Birbilis and Buchheit. In addition, it was concluded that the corrosion of intermetallic particles cannot be described by the measured corrosion potential alone, but a complete electrochemical characterization needs to be developed. The traditional concept of relative activity (active/noble) between two constituents is therefore insufficient enough to describe the total damage accumulation. Furthermore, Birbilis and Buchheit (2008) investigated for several of those intermetallics the corrosion potentials and electrochemical characteristics in 0.1 M NaCl solution at varying pH [24], and in 2014 together with Cavanaugh and Li, the same electrochemical characteristics in 0.1M NaCl by variation in temperature [34]. Results show that electrochemical behaviour of such intermetallics varies markedly with pH and is heavily dependent on temperature, which influences the localized corrosion (and protection) in aluminium alloys.

2.3.2 Intergranular- and exfoliation corrosion

The susceptibility to intergranular and exfoliation corrosion is mainly determined by the segregation of solute atoms and the precipitation of strengthening particles at the grain boundaries in AA7075. Moreover, the formation of precipitate free zones (PFZ) plays a role in the corrosion susceptibility [4].

Strengthening particles are anodic with respect to the aluminium matrix [35; 11]. During solution heat treatments, these compounds dissolve and segregate to the grain boundaries due to supersaturation of the elements Zn and Mg, resulting in an anodic increase. At the grain boundaries this provides an anodic path for localized corrosion, which increases the susceptibility to intergranular corrosion in the aluminium alloy (Figure 2.7; left and middle image). With aging processes, these elements precipitate and grow at the grain boundaries, which initially provides strength to the aluminium alloy and partially reduces the susceptibility to intergranular corrosion. However, the susceptibility to corrosion remains overall quite high in a T6 temper, as precipitates form a fine and almost continues anodic deposition at the grain boundaries. In overaging tempers (e.g. T76), the size of the particles and interparticle spacing increases and the overall concentration of the precipitates decreases, resulting in a higher resistance to intergranular corrosion compared to the the aged, T6, temper [18]. Furthermore, Ramgopal et al. (2001) investigated the influence of copper and aluminium in the η phase strengthening particles, since this phase contains a high solubility for these elements [35]. Although, the amount of copper was quite high, they found that incorporation of Cu in the $MgZn_2$ above 17 atom% increases the breakdown potentials beyond the one of $MgZn_2$, as it reduces the potential difference with the cathodic areas. Moreover, they found that the addition of aluminium up to 10 atom% did not change the behaviour of $MgZn_2$ significantly [35].

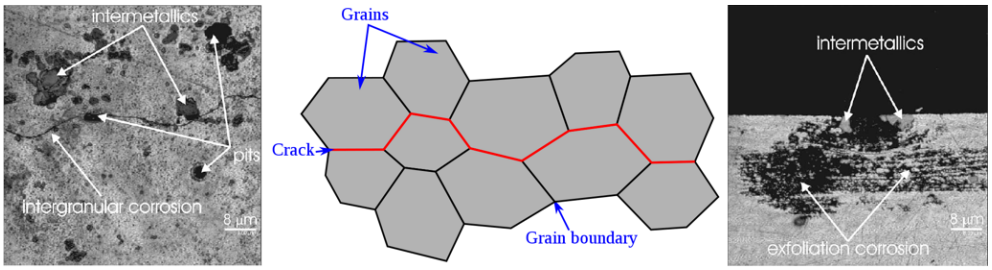

Figure 2.7: Middle: Illustration of intergranular corrosion; Left and Right: Intergranular and exfoliation corrosion of the AA7075-T6 matrix at the second breakdown potential (Figure 2.4) after 10min of OCP measurement in 3.5% NaCl. [18]

When strengthening particles precipitate at the grain boundaries, the diffused solute atoms leave a depleted zone adjacent to the grain boundaries [4]. This depleted zone is called the precipitation free zones (PFZ) and has a different electrochemical behaviour with respect to the matrix and grain boundaries. Consequently, this region contributes to the corrosion degradation along the grain boundaries. Fourmeau et al. (2015) confirmed that PFZs are depleted with solute atoms (Zn, Mg and Cu) compared to the aluminium matrix, but still contains a certain amount of alloying elements in solid solution [36]. Their results indicate that the material in the PFZ is somewhere in-between pure aluminium and aluminium in solid solution, where the concentration of alloying elements is in supersaturated solid solution. The width of the PFZ has found to be approximately 20-70nm on either side of the grain boundary [37; 38; 36], and [37] found that during overaging a small increase in width of this region was noticeable. However, the influence of the size and composition of this region on the intergranular corrosion behaviour is not yet fully understood.

Exfoliation corrosion is a form of intergranular corrosion common in wrought high strength aluminium alloys with a typical appearance as shown in Figure 2.7 (right image) [39]. The corrosion products formed by intergranular corrosion usually have a larger volume than the original aluminium alloy. This creates an expansion of corrosion products, resulting in stresses that can lift the surface grains and thereby removing non-corroded material. These anodic pathways, parallel to the working direction of the alloy create a typical layered type of attack, which is stimulated by the presence of Cu- and Fe-rich intermetallics along these paths. Therefore, an important requirement for exfoliation corrosion is the elongated grain structure along the working direction of the alloy. Excluding this structure protects the material from exfoliation, however to some extent the appearance and degradation can also be controlled by using heat treatments as explained previously.

2.3.3 Filiform corrosion

In aircraft structures, a common localized type of corrosion under thin films is filiform corrosion that occurs at the interface of the aluminium alloy substrate and an applied coating [6; 40]. On coated aluminium alloys, filiform corrosion is a complex phenomenon where many individual influences on filiform propagation are interactively coupled, such as influences of the environment, the aluminium alloy substrate microstructure, the coating–substrate interface (i.e. natural oxides or pretreatments) and the applied organic coating properties. Also, the presence of oxygen is essential for this type of corrosion, since it provides the primary reactant for the cathodic reaction [41].

Filiform corrosion is in principle a type of oxygen concentration cell whereby differential aeration results in spatial separation of the anodic area, the ”head”, and

the surrounding cathodic area, the "tail", which appears as a typical worm-like structure [40]. Aluminium dissolves in the anodic site, whereas oxygen reduction takes place to form hydroxyl ions at cathodic site [42]. In addition, the presents of chloride ions is needed to provide electrolyte conductivity and to stimulate corrosion initiation. The filiform process is shown in Figure 2.8. Intermetallic particles present in the aluminium alloy substrate have a pronounced effect on the propagation behaviour of filiform corrosion. This means, that aluminium alloys of the 1000-series, which contain low contents of alloying elements, show very good filiform resistance [43; 42]. Additionally, for the Al-Cu and Al-Zn model alloys used in [42], it has been found that filiform corrosion initiation characteristics are related to the passive range of the alloy. In other words, to the ease of pitting. Therefore, a smaller passive range corresponds to a higher filiform site density for both model alloys.

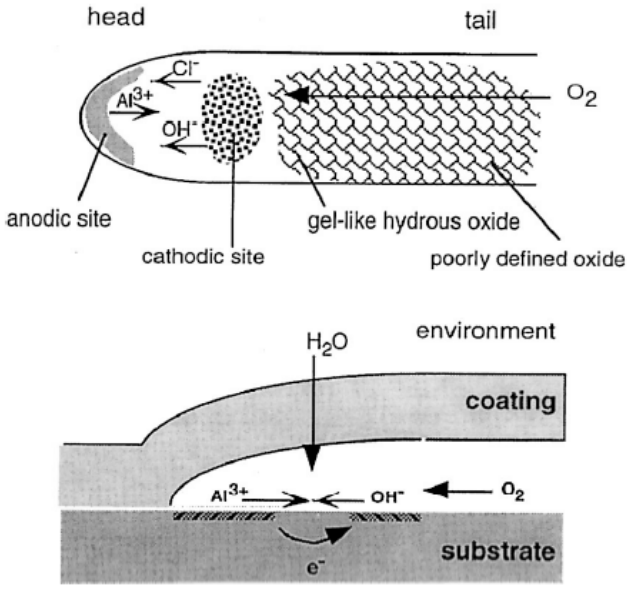

Figure 2.8: The propagation of filiform corrosion on aluminium according to the anodic undermining mechanism. [42]

Furthermore, filiform corrosion initiates at crevices like a crack or rupture that can occur around rivet heads, fastener holes or lap joints especially under chlorine rich, acidic and humidity conditions [43]. Paint blistering around these structural components is a typical appearance of this corrosion type.

2.3.4 Galvanic corrosion

Galvanic corrosion is an electrochemical process whereby one metal preferentially corrodes when it is in electrical contact with another metal. Not only the electrical contact is essential for this type of corrosion, but also the ion exchange through an electrolyte which prevents charge build-up that would otherwise block the ongoing reactions. Metal consist of a specific electrode potential depending on the metallurgical factors and environmental conditions. This means that when two dissimilar metals are connected to each other, a potential difference is created between those materials. The metal with the most negative potential (most reactive) behaves as the anode, while the other metal (less reactive) acts as the cathode. In such a galvanic cell, the potential difference is the driving force for an accelerated corrosion attack on the anodic metal. This leads to dissolution of the anodic metal into the electrolyte and inhibition of corrosion on the cathode. By measuring the potentials

of various metals and alloys in the desired conditions, the galvanic series can be created as shown in Figure 2.9.

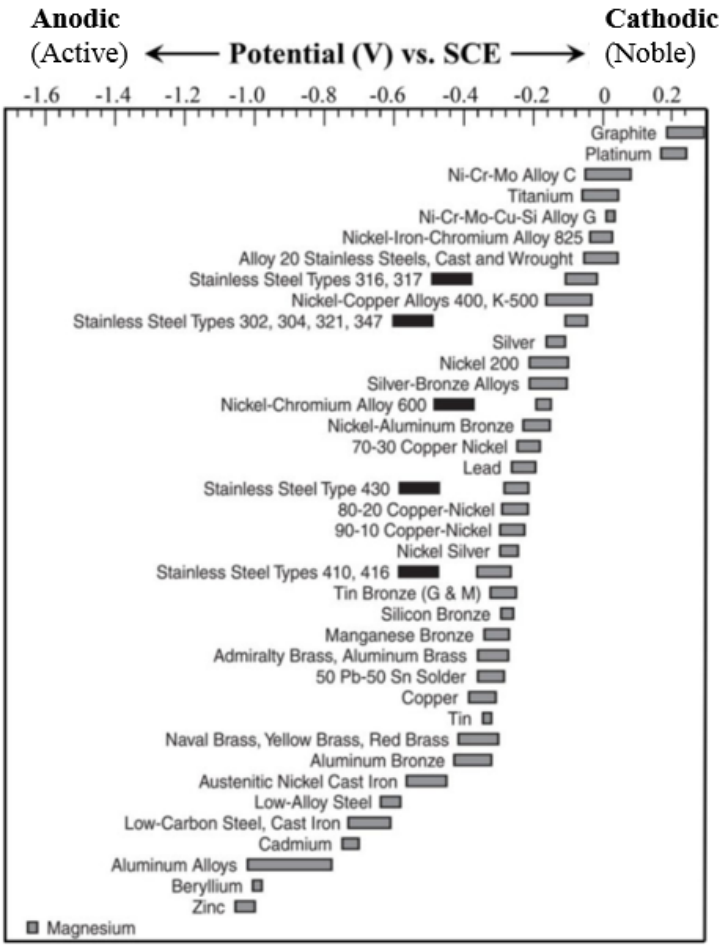

Figure 2.9: Galvanic series of some metals in ambient seawater. [23]

Galvanic cells can be used deliberately, for example to generate electricity in a battery or to cathodically protect structures with sacrificial anodes. However, it can also appear undesirably, resulting in accelerated degradation of the metal which can lead to catastrophic failures. The galvanic coupling can occur macroscopically, for example when a bolt is connected without sealing to a flange of another material, but also microscopically e.g. between second phase particles and the bulk aluminium matrix[8]. To protect the material from galvanic corrosion, it is therefore essential to understand the most critical cathode and anode present in a possible galvanic system.

2.4 CORROSION PROTECTION

To protect aluminium alloys from corrosion on an aircraft, a protection scheme is used which usually consist of a pre-treatment and a coating system [6]. The first layer of a protection scheme is a pre-treatment, such as a chemical conversion coating, an anodizing layer or a wash primer. On top of the pre-treatment mainly an organic coating is applied, which can be a primer or a primer-topcoat system. Its primary function is to act as a passive barrier between the substrate and the environment, but when the protection scheme is damaged it must also provide active corrosion protection. This active corrosion protection can be implemented in the primer and can be achieved with various corrosion inhibiting strategies, such as inhibition through leaching, galvanic inhibition and by smart and self-healing coating technologies. Inhibition through leaching and galvanic inhibition have already been introduced to the aerospace market, where in the aerospace industry this leaching strategy currently forms the basis of aerospace specifications [6].

In addition, a layer of a different aluminium alloy, known as an clad layer, can be applied on the aluminium alloy substrate to enhance the protective properties of the aluminium alloys. This layer contains higher corrosion resistance properties due to the absence of microstructural phases and acts as a sacrificial layer when the aluminium alloy substrate is damaged. Therefore, the protection performance and properties of an clad layer will be discussed first in this chapter, followed by the inhibition through leaching technique by inorganic inhibitors. Finally, this section ends with the inhibition performance of various organic compounds that have excellent inhibition performance but are not as efficient when implemented in a coating due to their different protective mechanism and irreversibility [44].

2.4.1 Alclad

In the aerospace industry, protection schemes are used to protect the aluminium alloy substrate against environmental influences. A simple but very effective way to protect the aluminium alloy surface is to make use of a cladding technique, known as Alclad. This clad layer can be a component of such protection scheme and is nowadays a general term to describe sheet material produced by metallurgically bonding of high-purity aluminium surface layers to high-strength aluminium alloy substrate material [25]. An clad layer thickness is typically in the range between 2-10% of the substrate thickness, because it needs to provide a sufficient absolute thickness of the overall structure [25; 40]. Generally, a composition of 99%Al and 1%Zn (e.g. AA7072) is used on aluminium alloys in the 7XXX series [25], however, also different clad compositions can be used on AA7075, such as AA7008, AA7011 and AA7001 [45; 46; 40].

The corrosion resistance of Alclad is mainly due to the absence of microstructural secondary phases in the clad layer, and therefore contains higher corrosion resistance properties than the underlying aluminium alloy substrate [25]. The most severe localized corrosion types on AA7075, as discussed in Section 2.3 are pitting, intergranular- and exfoliation corrosion. Pitting corrosion is relatively the least damaging and most easily controlled corrosion mechanism on AA7075. Intergranular corrosion generally causes more severe damage to the material and is much more difficult to detect compared to pitting corrosion. However, by the same procedures both mechanisms can be minimized by the use of an clad layer, and as a result this may also minimizes the appearance of exfoliation corrosion [19].

Alclad not only possesses higher corrosion resistance due to its relative pure form, but it also acts as a sacrificial layer when the aluminium alloy substrate is exposed to an electrolyte in a damaged area [40]. The potential difference between the alu-

minium alloy substrate and the clad alloy is usually designed so that the clad layer is approximately 80 to 100mV anodic with respect to the aluminium alloy substrate [40]. In Figure 2.10, electrochemical potentials are displayed of various aluminium alloys and constituents. It can be concluded from this figure, that the presence of copper in the solid solution increases the potential cathodically, whereas the addition of magnesium and zinc in solid solution reduces the potential of purely 99.95% aluminium to more anodic values [5]. In addition, Askari-paykani et al. (2012) found that dissolution of the clad layer in an acidic media increased the pH value of the solution, which transferred the aluminium alloy specimen to the passivation region, protection it from further corrosion degradation [45].

The protection performance of an clad layer depends on the optimum values of current (affected by the potential difference between the clad layer and substrate material), conductivity of the electrolyte, polarization and film formation.

Solid Solution Composition	Potential, Volts, 0.1N Calomel Scale[b]
α (Ag-Mg) (Mg_5AL_8)	−1.24
Al + Zn + Mg (4% $MgZn_2$ Solid Solution)	−1.07
Al + Zn (4% Zn Solid Solution)	−1.05
β (Zn-Mg) ($mmgZn_2$)	−1.05
Al + Zn (1% Zn Solid Solution)	−0.96
Al + Mg (7% Mg Solid Solution)	−0.89
Al + Mg (5% Mg Solid Solution)	−0.88
Al + Mg (3% Mg Solid Solution)	−0.87
α (Al-Mn) ($MnSi_6$)	−0.85
Aluminum (99.95%)	−0.85
Al + Mg + Si (1% $MgSi_2$)	−0.83
Al + Si (1% Si Solid Solution)	−0.81
Al + Cu (2% Cu Solid Solution)	−0.75
(Al - Cu) ($CuAl_2$)	−0.73
Al + Cu (4% Cu Solid Solution)	−0.69
α (Al-Fe) (Fe-Al_3)	−0.56
$NiAl_3$	−0.52
Silicon	−0.26

[a]Data from ALCOA Research Laboratories.
[b]Measured in aqueous solution of 53 g NaCl + 3 g H_2O_2 per liter at 25°C

Figure 2.10: Electrode Potentials of Aluminium Solid Solutions and Constituents. [5]

The use of heat treatments affects the corrosion resistance properties of AA7075 significantly. This also applies to clad layers, especially at longer heat treatment times. Therefore, shorter annealing times are required when an clad material is to be annealed. This reduces the the amount of alloying elements that can diffuse into the clad layer, because when this diffusion occurs, the corrosion resistance of the clad layer is reduced. During solution heat treatments of an clad alloy, even the shortest possible time at these temperatures should be used. This avoids the diffusion of solute elements into the clad layer, which also decreases the corrosion resistance of the material. Moreover, due to the risk of solute diffusion, reheating treatments on clad materials are limited to a maximum of three times. In the 2xxx series of aluminium alloys this is especially important because the diffusion of copper to the clad materials makes the clad layer less anodic. However, in alloys containing magnesium and zinc it is less important, as these elements increase the anodic potential in the clad material which is in favour for galvanic protection [40].

2.4.2 Corrosion inhibitors

Corrosion inhibitors are organic or inorganic substances that can prevent or inhibit corrosion of the protective material in a corrosive environment. When considering leachable inhibitors, the inhibitor must be (sparsely) soluble, provide fast and effective inhibition, whereby the inhibition must be irreversible [44]. Lithium based inhibitors have proven to be excellent on these four key criteria and will therefore be discussed first [47]. Subsequently, several organic inhibitors will be discussed as high efficiency has been found in many of them compared to the benchmark, chromates.

Inorganic inhibitors

Many studies have shown that lithium-based inhibitor coatings provide fast and effective corrosion protection on high strength AA2024-T3 [48; 49; 50; 44; 51; 52]. Recently, Visser et al. (2019) investigated with a scanning electron microscopy and electrochemical techniques, the active corrosion behaviour of lithium inhibitor coatings on various aluminium alloys, including AA7075-T6 [47]. A Neutral Salt Spray test (ASTM B-117) was performed for different coated aluminium alloy substrates, with and without lithium inhibitors. AA7075-T6 coated without lithium inhibitor showed severe corrosion after 168 hours exposure, while AA7075-T6 coated with lithium inhibitor showed almost pristine scribes. Moreover, a three-layered morphology was observed with an approximate thickness of 1 µm on AA7075-T6 that was coated with lithium inhibitor primer. This polycrystalline layer is typical for the formation of the protective layer in the lithium leaching technology and is the basis of the overall protection mechanism [53; 54]. Electrochemical impedance spectroscopy (EIS) with equivalent electric circuits (EC) measurements, confirmed this increase in protective performance due the formed polycrystalline layer, however slightly less protective properties were measured compared to AA2024-T3 [50; 53].

Furthermore, "corrosion resistant" alloys such as AA6014-T4 and AA5083-H111 were analysed according to the same procedure as for AA7075-T6 and AA2024-T3. The corrosion inhibiting effect of the lithium-leaching coatings seems to be more pronounced on the alloys with relatively large amounts of alloying elements and higher electrochemical activity. Also, in the alloys AA6014-T4 and AA5083-H111, lithium leaching suppressed localized corrosion attack and increased the corrosion resistance by forming a similar three-layered protective layer. Therefore, it can be concluded that lithium-based inhibitor coatings provide active protective behaviour to the aluminium alloys tested, independent of their metallurgy [47].

Organic inhibitors

Harvey et al. (2011) reported the corrosion inhibitor effectiveness of several structurally related organic compounds on AA2024 and AA7075 in 0.1 NaCl solution by means of mass loss experiments [55]. The effect of the inhibitor structures is expressed in inhibitor efficiency (I%), with a value of 100% when no weight loss was recorded as in the case of Cr(VI). The compounds chosen, are likely to formed metal-organic surface complexes because such surface complex is able to provide a mechanical and electrochemical barrier on the substrate that inhibits corrosion reactions [56]. The most effective corrosion inhibitors on AA7075 in order of decreasing inhibitor efficiencies are displayed in Table 2.1.

Table 2.1: Inhibitor efficiency of the compounds studied by Harvey et al. (2011).

Corrosion inhibitors	Inhibitor efficiency (%)
Na-(diethyl(dithiocarbamate))	96 ±4
6-amino-2-mercaptobenzothiazole	94 ±1
Benzotriazole	92 ±4
2-mercaptobenzothiazole	91 ±3
Na-(6-mercaptonicotinate)	86 ±0
2-mercaptobenzimidazole	84 ±5
4,5-diaminopyrimidine	84 ±2
Na-mercaptoacetate	83 ±0
4,5-diamino-2,6-dimercaptopyrimidine	80 ±0
Na-2-mercaptobenzoate	80 ±0
Na-4-mercaptobenzoate	76 ±1
Na-2-mercaptonicotinate	70 ±4

According to AA7075, several components had a strong influence on the corrosion inhibition, for example, the addition of a thiol group (-SH), which strongly increases the corrosion inhibition. However, compared to AA2024, thiol-containing compounds were less effective on AA7075, which is believed to the higher amount of Cu present in AA2024. Moreover, ortho- and para- positions to a carboxylate group on a monoaromatic ring strongly inhibits corrosion, as well as the substitution of N for C in an aromatic ring where it can form a coordinating site with a carbonyl or nitrogen. In addition, the effect of the amino group (-NH_2) was not extensively investigated by the authors. However, the most beneficial effects by adding this group were observed on AA7075, probably due to the higher Zn content and the presence of high Zn containing precipitates (e.g. $MgZn_2$) in AA7075.

Bereket and Yurt (2001) found that the addition on 0.01M hydroxy carboxylic acids or amino acids to a 0.05 NaCl solution on AA7075 causes a shift to more noble E_{pit} values. They concluded that in acidic solutions, amino acids are more effective in shifting the pitting potential to noble values, while in neutral and basic solution, hydroxy carboxylic acids is the most effective in shifting E_{pit} to a more noble value. Moreover, they found that the addition of 0.01M $NaNO_3$ in combination with hydroxy carboxylic acids also caused a pitting potential shift to more noble directions, however, 0.01M $NaNO_3$ in combination with amino acids had no influence on the passivation of AA7075 [57]. In a later study, Yurt et al (2005) investigated further the inhibitor effect of amino- and hydroxy carboxylic acids on AA7075 in 0.05M NaCl, with quantum chemical studies[58]. The amino acids tested were glycine, aspartic acid, valine, alanine, phenylalanine, and glutamic acid at a pH of 5, while the hydroxy carboxylic acids studied were glucolic acid, malic acid, lactic acid, mandelic acid, benzylic acid, and citric acid at a pH of 8. They found that both chemical and physical adsorption played a major role in the inhibition of pitting corrosion on AA7075.

Liu et al. (2014) studied the inhibitor efficiency of 8-Hydroxyquinoline (8-HQ) for AA7075 in 3.5% NaCl and ethanol 3.5wt.% NaCl solutions by using electrochemical techniques [59]. 8-Hydroxyquinoline is an organic compound with C9H7NO as molecular formula and is commercially used around the world under various names. The authors found an increase in inhibitor efficiency due to an increase in its concentration, with a maximum inhibition efficiency value of 96%, obtained at 5.52mmol/L 8-HQ solution. According to the potentiodynamic polarization measurements, the conclusion was made that the 8-HQ acts as a cathodic and anodic inhibitor. Scanning electron microscopy (SEM) and scanning electrochemical mi-

croscopy (SECM) confirmed the adsorbed film formation on the aluminium alloy surface. However, when comparing the results of the Tafel polarization and electrochemical impedance spectroscopy measurements, a very poor correlation is shown between the results at lower concentrations. Although, on higher concentration the results are more or less in line.

2.5 SUMMARY AND CONCLUSION

Intermetallic particles are insoluble during heat treatments and subsequently aging processes. Cu- and Fe rich intermetallics are found to be cathodic relative to the aluminium matrix, whereas Mg-rich intermetallic can change their potential from anodic to cathodic when the aluminium alloy undergoes solution heat treatments. This change in potential during solution heat treatments is explained by the dissolution of strengthening particles. Strengthening particles are strongly affected by heat treatments and subsequent aging processes. When these particles dissolve, they create a supersaturated solid solution of the elements Zn and Mg in the aluminium matrix. This dissolution results in an anodic increase of the matrix and promotes the galvanic coupling between the intermetallic particles and the aluminium matrix. Although these particles affect the corrosion susceptibility, they also increase the strength of the aluminium alloy when precipitated during aging processes. Furthermore, dispersoids are formed in the aluminium alloy microstructure during ingot homogenisation. Precipitated dispersoids mainly control the grain size and the degree of recrystallization of the aluminium alloy and may slightly change their composition during heat treatments. However, because of their comparative electrochemical inertness and insignificance proportion, these particles are not of particular interest in regards to localized corrosion. Therefore, the type, concentration, and distribution of intermetallics and strengthening particles in the aluminium matrix, including the specific temper, mainly determines the electrochemical properties and corrosion susceptibility of AA7075. In addition, a relation was found between the Volta potential of intermetallics and the aluminium matrix, and the breakdown potentials, which can be of particular importance to understand the galvanic corrosion behaviour.

In AA7075, corrosion initiates around cathodic intermetallic particles by dissolution of the aluminium matrix. In a study to pitting corrosion, the intermetallic Al_7Cu_2Fe appears to be the main contributor to large pits formation and contains the highest "cathodic" current at the corrosion potential of AA7075 among the tested second phase particles. The cathodic intermetallic particles also support the oxygen reduction reaction, resulting in locally formed hydroxides around those particles. The passive film on aluminium is unstable with the presence of these ions, causing film degradation around the intermetallics before film degradation occurs in the rest bulk aluminium matrix. The active particles (e.g. Mg_2Si and $MgZn_2$) present in AA7075 appear to dissolve fast, thereby leaving small but passivated pits that are not deeply penetrated into the aluminium alloy substrate. Dissolution of the active particles and aluminium matrix increases the cathodic surface area, which means that the cathodic current density increases and as a result the dissolution rate of the active regions. Pitting corrosion can propagate and evolve into intergranular- and exfoliation corrosion. The susceptibility to these types of corrosion are mainly affected by the transformation of strengthening particles during heat treatments and the different tempers used on AA7075. In addition, an elongated grain structure along the working direction of the alloy is required for exfoliation corrosion. When a coating is applied on the aluminium alloy substrate, filiform corrosion may occur. The initiating characteristics of this corrosion type are related to the ease of pitting of the aluminium alloy. Moreover, intermetallic particles contain a pronounced effect on the propagation behaviour of filiform corrosion, because these particles are

able to favour the oxygen reduction reaction. All of the mentioned above corrosion mechanisms can be stimulated by an galvanic effect, whereby the potential difference is the driving force for an accelerated corrosion attack. Therefore, it is always essential to understand the most critical cathode an anode in a specific material or structure.

In order to protect AA7075 from corrosion, it is important to inhibit the oxygen reduction reaction on the cathodic areas. In the aerospace industries this is achieved by the use of protection schemes. Such protection scheme primarily acts as a barrier layer, but also provides active corrosion protection in a damaged area by leaching or galvanic inhibition which can be implemented in the coating primer. For instance, corrosion inhibition through leaching can be achieved by using many different materials, usually divided into two main groups, namely inorganic and organic inhibitors. The inhibition performance of inorganic inhibitors, such as lithium salts is mainly based on the formation of hardly soluble salts or oxide films on the aluminium alloy surface. Organic compounds, usually based their inhibiting mechanism on adsorption on the oxide film. Although both types of inhibitors show high inhibiting efficiencies, only inorganic inhibitors such as lithium salts are suitable for implementation in a coating due to their irreversible film formation. Furthermore, part of such a protection scheme can be an clad layer. The clad layer contains higher corrosion resistance properties compared to the aluminium alloy substrate due to the absence of microstructural phases and is designed to act as a sacrificial layer when the aluminium alloy substrate is exposed in a damaged area. In addition, corrosion inhibitors in combination with clad can alter the solution potential relationships between clad and core material and heat treatments can affect the corrosion resistance of clad by diffusion of alloying elements from the aluminium alloy substrate into the clad layer.

3 MATERIALS AND METHODS

This chapter describes the materials and methods used in this thesis. First, the as received materials will be described, followed by their chemical composition. Then, the sample preparation per experiment is discussed in the same order as shown in Chapter 4. This chapter concludes with the experimental techniques used in this thesis, with an emphasis on the experimental set-up and relevant parameters.

3.1 MATERIALS

The materials used in this thesis were acquired from various sources, as shown in Table 3.1. Aluminium, zinc, AA7075C and AA7475C are all sheet metal. The fasteners are made of AA2017A and were Chromate Conversion Coating (CCC) stripped before receipt.

Table 3.1: Materials used in this study.

Materials	Temper	Thickness	Supplier
Aluminium	As rolled	1.0 mm	Goodfellow
Zinc	As rolled	0.7 mm	Salomons
AA7075C	T6	1.0 mm	Thyssen-Krupp
AA7475C	T76	1.6 mm	Customer
AA2017A	T4	N/A	Customer

The chemical composition of the materials and alloys used is summarized in Table 3.2. Both AA7075C and AA7475C alloys consist of a sandwich-structure containing two different aluminium alloys, as shown in Figure 3.1. The clad layer of AA7X75C is known as AA7072 and is therefore added separately to the Table 3.2. In this thesis AA7X75C is used to indicate the sandwich-structure, AA7072 only for the clad layer on both substrates, which are designated AA7075B and AA7475B.

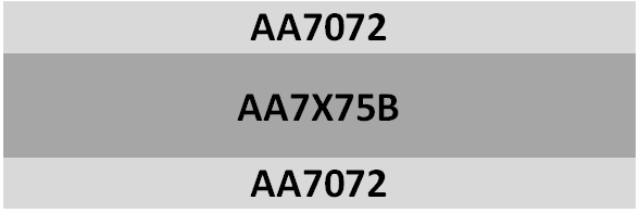

Figure 3.1: Schematic illustration of AA7X75C

Table 3.2: Chemical composition of the materials with maximum values when no range is added [60].

Materials	Si	Fe	Cu	Mn	Mg	Cr	Zn	Ti (+Zr*)	Others	Al
Aluminium	-	-	-	-	-	-	-	-	-	99.99
Zinc	-	-	-	-	-	-	>99.95	-	-	-
AA7075-T6	0.4	0.5	1.2-2.0	0.3	2.1-2.9	0.18-0.28	5.1-6.1	0.2	0.15	rest
AA7475-T76	0.1	0.1	1.2-1.9	0.1	1.9-2.6	0.18-0.25	5.2-6.2	0.1	0.15	rest
AA7072	0.3	0.4	0.1	0.1	0.1	0.1	0.8-1.3	0.1	0.15	rest
AA2017A-T4	0.2-0.8	0.7	3.5-4.5	0.4-1.0	0.4-1.0	0.1	0.25	0.25*	0.15	rest

3.2 SAMPLE PREPARATION

This chapter evaluates all sample preparations required in this thesis. The sample preparation is discussed per experiment in the same order as the results are evaluated in Chapter 4.

3.2.1 The role of zinc

To study the role of zinc in the clad layer, three main topics are investigated. The electrochemical behaviour, the microstructure and a zinc distribution. Specific sample preparations have been used for each topic and will therefore be discussed separately in the mentioned sequence.

Electrochemical behaviour of the clad layer

The electrochemical behaviour of AA7072, aluminium and zinc was performed by Open Circuit Potential (OCP) and Potentiodynamic polarization (PP) measurements. The setup en experimental parameters of these techniques is explained in Section 3.3. Each sheet metal was cut into 10 by 2 cm strips and degreased with cleaning solvent to remove surface contamination. Zinc was wet abraded with 800-1200-2000-4000grid sanding paper, while AA7072 and aluminium were only sanded from 2000 to 4000grid. This difference in sample preparation process was selected to prevent sanding away the AA7072 clad layer on AA7X75B, and because aluminium cannot be abraded with coarser grains due to its softness. After sanding, the materials were rinsed with distilled water. Then, reproducible area's were punched in polyester tape that determined a constant exposed area of $1.2cm^2$ during the measurements, as shown in Figure 3.2. The small black line above the tape indicates the fixed height of all samples used, so that the Working electrode (WE) and the tip of the Reference electrode (RE) could be placed on the same horizontal level.

Figure 3.2: An example of a specimen used for the OCP and PP measurements.

The microstructure and clad layer thickness

To observe the microstructure and clad thickness under an optical microscope, cross-sections were embedded in cold non-conductive epoxy resin as shown in Figure 3.3. Hot embedding was tried first, but caused a lot of contamination after sanding on the aluminium surface, visible as dark spots, as shown in Figure 3.4. Probably longer sanding times would excluded this contamination, however for some experiments in Section 4.2, only a small maximum height was allowed for sanding and polishing to observe a specific degradation spot in the material. Therefore, cold embedding was used with a 2:1 ratio of Struers ClaroCit powder and liquid. After curing for approximately 2 hours in a pressure pot, the samples were mechanically

sanded from 80 to 2000grid (10μm) and polished with polishing abrasive of 3μm and 1μm in size. To obtain a completely shiny and scratch-free surface, the final polishing step is performed for approximately 5 minutes with an Oxide Polishing Suspension (OP-S), consisting of colloidal silica abrasive with grain sizes of 0.25 μm. After the last polishing step, the samples were rinsed, cleaned in an ultrasonic bath and blown dry with cold air.

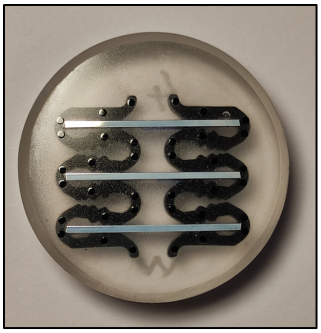

Figure 3.3: Example of cold embedded samples.

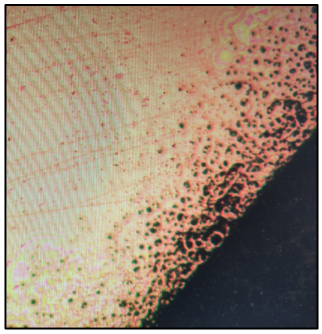

Figure 3.4: Example of surface contamination.

Etching the samples was achieved with a dilute mixture of Sulfuric acid (H_2SO_4) and Hydrofluoric acid (HF). First a mixture of 90ml distilled water and 10ml H_2SO_4 (96%) was made, followed by a mixture of 95ml distilled water with 5ml of HF (40%). Then, both mixtures were added in a 1:1 ratio by volume. To observe the clad layer thickness on AA7075C, 20 seconds etching time was needed and to observe the microstructure, 60 seconds of etching time was necessary. AA7475C(TSA) was etched for 20 seconds, enough to accentuate both the microstructure and clad thickness. The clad thickness was measured with the supported software on a digital optical microscope (Keyence VHX-5000). A total of twenty measurements were taken per sample at two different locations. For each aluminium alloy three samples cut from different panels were used in order to obtain the most representative value possible.

Determination of an element distribution

The zinc distribution in AA7X75C was measured using SEM-EDS. Conductive samples are required to perform this experiment, either by using conductive tape or by using conductive resin. The latter was chosen to exclude as many electron noise as possible during the measurement. To embed the alloys, cold conductive Kemet Acrylic CLB powder and liquid was used in a 1:1 ratio. After the samples were cured in a pressure pot for approximately 2 hours, the samples were mechanically sanded from 80 to 2000grid (10μm) and polished with polishing abrasive of 3μm and 1μm in size. To observe the microstructure and the difference between the substrate and the clad layer, the final polishing step was performed with OP-S for approximately 25-30min. The OP-S suspension reacts chemically with the surface of the specimen, whereby the microstructure becomes accentuated and appears while using the Scanning Electron Microscopy (SEM). After polishing with OP-S, a white slushy layer remains on top of the surface. Cleaning this layer, without inducing scratches to the surface, can be a huge challenge on aluminium alloys. The best results have been achieved by lightly buffing the sample on a clean polishing cloth using only a generous amount of iso-propanol. Cleaning the OP-S slush with dishwashing fluid in the ultrasonic bath for a certain amount of time was not an option, because this created an alkaline environment in which aluminium corroded too severely. The last step was to ungas the samples, which took approximately 45 min before it reached low vacuum ($< 1,0x10^{-1}$ mbar).

3.2.2 The galvanic corrosion behaviour

The sample preparation for the experiments performed in Section 4.2 can be divided into five main sections. First, the sample preparation required to reproduce the galvanic effect is discussed. Second, the electrochemical behaviour by means of OCP and PP measurements, followed by the galvanic corrosion experiments. Lastly, the sample preparation required for the galvanic corrosion experiment in-situ is evaluated and the adjustments for the SEM-EDS analysis.

Reproduction of the galvanic effect

Reproducing the galvanic effect requires samples with a constant cathode and anode area. This section explains the reproducible scribed area of the AA7X75C anode, followed by the constructed constant area of the fasteners that behaves as the cathode when both are combined in a galvanic cell. To reproduce the anodic area, the following steps were performed:

1. Application of the coating
   Multiple AA7X75C panels were degreased with cleaning solvent to remove surface contamination and lightly abraded with Scotch-Brite^{TM} to increase the coating adhesion. A clearcoat model formulation based on epoxy-amine chemistry was designed with an 1.0 stoichiometric ratio between the epoxy and amine resin. The paint was applied on the alloy substrates by a pressurised automatic spray machine and cured in an AL-KO furnace at 80°C for about an hour, followed by 50°C overnight. After this procedure, the film thickness was measured with an average thickness as shown in Table 3.3

2. Cutting of the samples into the desired dimensions
   The coated samples were cut with a guillotine shear in the desired dimensions, depending on the experiments performed. The samples exposed to the NSS test for various periods from 168h to 504h were cut in two different dimensions. The first one is used to compare the coating efficiency in Section 4.3. For this, panels of 15 by 8cm were cut. As for the NSS test prior to the cyclic measurements in Section 4.3, panels were cut to sizes of 7 by 7cm. The rest of electrochemical experiments performed in Section 4.2 and Section 4.3 using a coated AA7X75C specimen were cut in dimensions of 10 by 2cm. The various samples with their dimensions are shown in Figure 3.5.

3. Milling of the defect area
   To create a constant exposed area, a horizontal milling machine was used with a milling-head width of 1mm. Depending on the various sample dimensions, different scribe sizes were milled, as presented in Figure 3.5. The scribes were all milled 250 $-$300 µm in depth.

4. Taping the undesired exposed areas
   The last step before the samples could be used for the experiments was to tape all the edges with polyester tape so that only the scribed area was exposed to the electrolyte. This was done in the same way as in Figure 3.2, only with a rectangular erased area around the scribe instead of a hole.

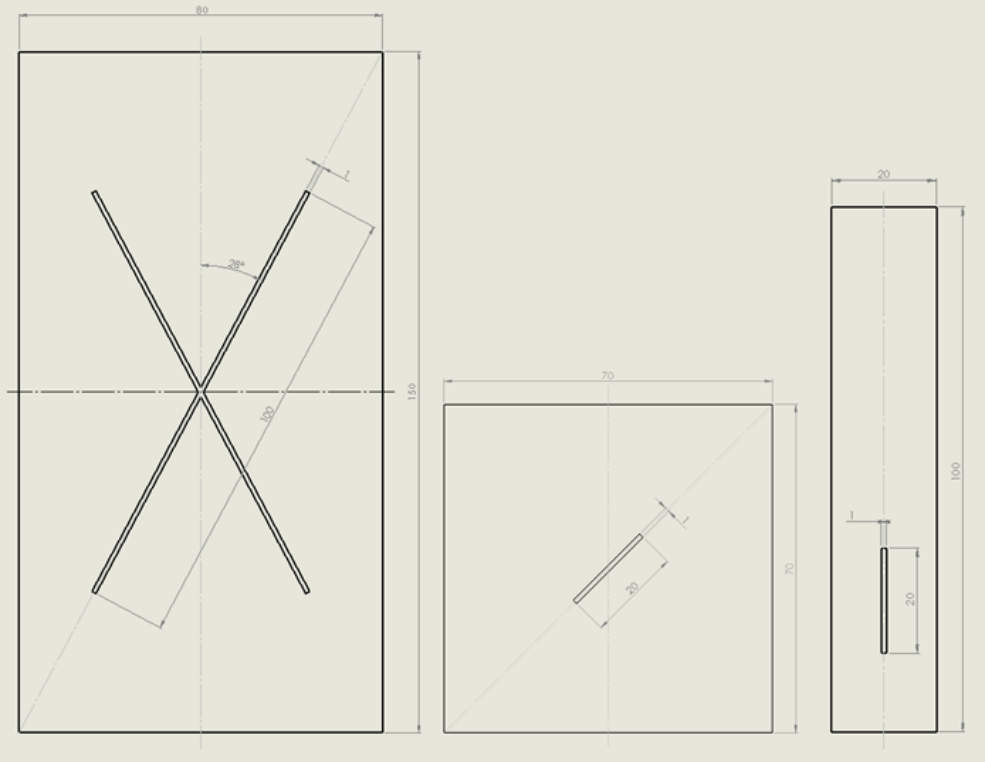

Figure 3.5: Schematic illustration of the various samples used with corresponding dimensions.

To reproduce the cathodic area, fasteners were embedded in epoxy resin so that a constant region is exposed to the electrolyte, whereby electrical connection with the fastener is still possible. This is conceived by using the following procedure, as shown and explained in Figure 3.6:

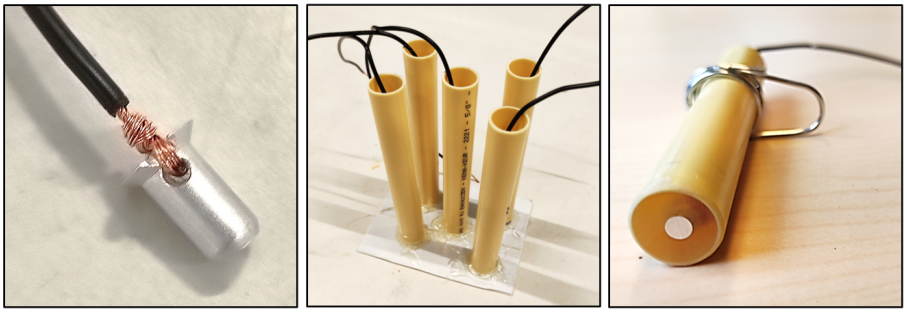

(a) (b) (c)

Figure 3.6: The first step is to drill a 1mm hole on the side of the fastener, as shown in Figure 3.6a. Next, the overhanging chamfer should be filed around the hole to facilitate winding of the electrical wire. After the electrical wire was added, silver paste is used to increase the electrical connection between the copper wire and the fastener. Finally, the electrical connection between the start of the copper wire and the tip of the fastener was tested with a multimeter. If electrical connection was measured, the fasteners could be used. Then, as shown in Figure 3.6b, the fastener tip was glued to a piece of cardboard with a PVC pipe concentrically glued around the fastener. When everything was fixed, a cold embedding mixture with a 2:1 ratio of Struers ClaroCit powder and liquid can be made and added, which takes approximately 2 hours to cure in a pressure pot. The last step is shown in Figure 3.6c, where the sample was mechanically abraded over the curvature of the fastener tip from 80 to 4000grid. In addition, a handle was attached to achieve always the same depth in the electrolyte while performing the experiments.

After the fasteners were produced according to the explained procedure, the resistance of the samples was measured with a multimeter. This, to confirm that the resistance of the new electrode did not change during the manufacturing process, which otherwise gives erroneous results during the electrochemical experiments.

Electrochemical behaviour of a galvanic couple

In the OCP and PP experiments, the 10 by 2cm AA7X75C specimens were used. To measure the OCP and PP of AA2017A, multiple fasteners were embedded in epoxy resin disks to lesser the distance between the WE and RE, as shown in Figure 3.7. The disks were made with a cold embedding of Struers ClaroCit powder and liquid in a 2:1 ratio mixture. After curing, the specimens were mechanically sanded from 80 to 4000 grid. To achieve electrical conductivity, a copper tape was attached to the fastener underneath the disk. Also, prior to these measurements the resistance of the new created WE was checked. Note that the same exposed area is created for the fastener as explained in Figure 3.6. This has also been checked after polishing using a digital optical microscope (Keyence VHX-5000).

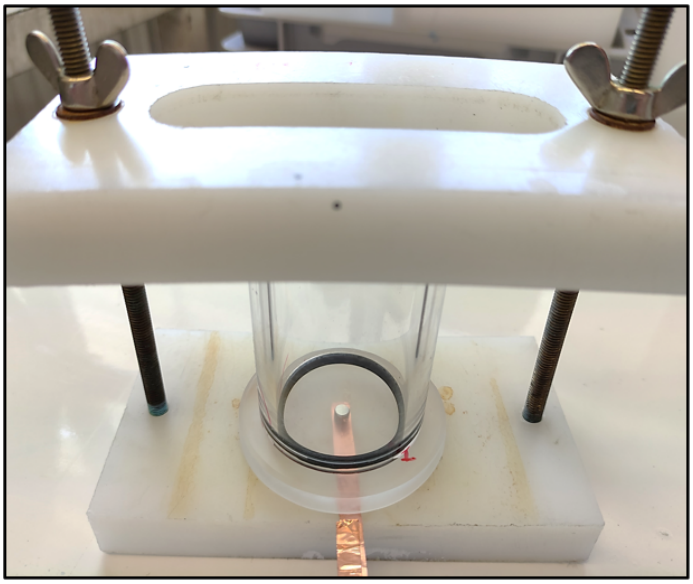

Figure 3.7: The OCP and PP set-up of an embedded fastener.

Galvanic corrosion experiments

The galvanic electrochemical measurements, such as Zero Resistance Ammeter (ZRA), potentiostatic and galvanostatic measurements were performed with the same 10 by 2cm AA7X75C specimens as explained by the step-by-step procedure in paragraph "Reproducing the galvanic effect". The fasteners used were made as explained in Figure 3.6. In addition to the ZRA measurement with one fastener, the effect of increased cathodic surface area was tested using multiple fasteners. Since many single fasteners became to sizable together, a new sample was created which could be used in the same way as shown in Figure 3.7, The sample preparations steps are listed in Figure 3.8.

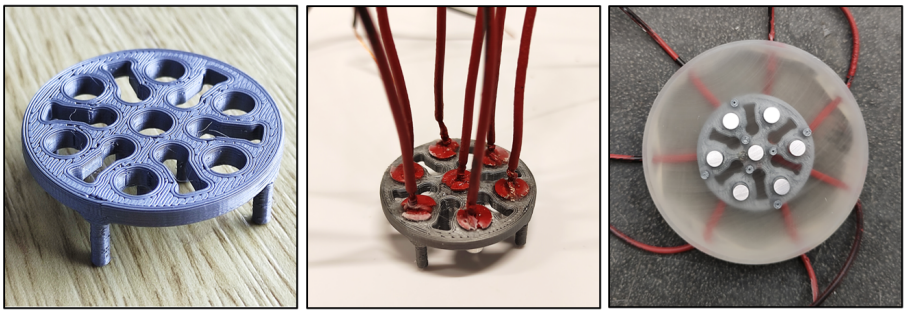

(a) (b) (c)

Figure 3.8: A model of a multiple fastener holder has been designed and constructed in SolidWorks [61], and produced on a Prusa MK3s 3D printer, as shown on Figure 3.8a. This holder is designed to increase the cathodic area six times while still fitting under the electrochemical cell, as shown in Figure 3.6. Moreover, as much free space as possible was designed to increase the epoxy volume and eliminate potential mutual interaction. Figure 3.8b shows how seven fasteners are attached, which are made in the same procedure as explained in Figure 3.6a. The red coating on top on the fastener is an anti-corrosion paint, however this is completely optional to use. After the wires were bent 90°, a cold non-conductive embedding mixture with a 2:1 ratio of Struers ClaroCit powder and liquid was made which took approximately 2 hours to cure in a pressure pot. The last step is shown in Figure 3.8c, where the sample surface is mechanically abraded from 80 to 4000grid.

The observation of galvanic corrosion in-situ

To observe corrosion in-situ through the clad layer, specimens were prepared as shown in Figure 3.9a. The sample preparation for these measurements was the same as evaluated in the paragraph "Microstructure", only a 0.5mm hole was punched in polyester tape with a biopsy needle to delineate the exposed area (indicated by the red arrow). Unexpected, as shown in Figure 3.9b, corrosion started to develop at the intermetallic particles in the substrate material instead of the desired propagation through the clad layer. Moreover, galvanic stimulated corrosion was not possible with the use of this sample in combination with an external cathode.

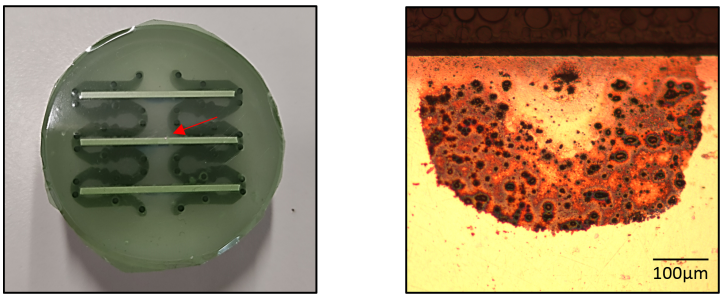

(a) (b)

Figure 3.9: (a) First constructed in-situ specimen. The exposed area is indicated by the red arrow. (b) First in-situ result where corrosion initiates only on the AA7075B substrate material.

Therefore, new samples had to be designed to observe the degradation of the clad material in the required direction (e.g. horizontally on the image view). This was achieved by the following procedure, as explained in Figure 3.10. Note that for Figure 3.10b and Figure 3.10c not the same sample is used, though the manufacturing procedure is identical.

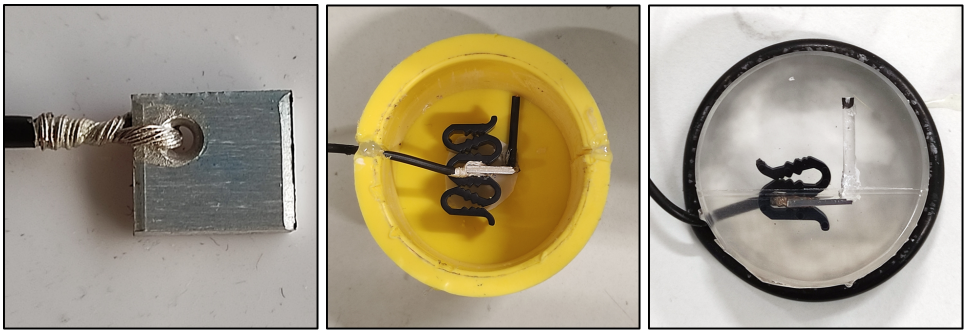

(a) (b) (c)

Figure 3.10: Figure 3.10a shows a scribed 1 by 1cm piece of AA7X75C, which is connected and tested by the same procedure as the fasteners in Figure 3.6a. Then, as shown in Figure 3.10b, the specimen is placed in a holder and glued to the bottom of a mould. To create a slot for the electrolyte, a small tube is added with silicone paste around it to ensure no epoxy can reach the scribed area and electrolyte interface. After the mold was sealed, a cold non-conductive embedding mixture with a 2:1 ratio of Struers ClaroCit powder and liquid was mixed which took approximately 2 hours to cure in a pressure pot. The final steps are shown in Figure 3.10c, where the sample surface is mechanically abraded from 80 to 2000grid and polished from 3μm to 1μm, so that still the difference between the substrate and clad layer is visible without etching. The specimen was then taped with transparent PTFE 5490 tape (3M Ltd) so that only a part of the scribed area is exposed to the electrolyte. In addition, a rubber band is added around the sample to hold it in place in a petri dish.

Characterization of elements in the clad remnants

SEM-EDS was used to characterize the elements present in the remnant regions after dissolution of the clad layer on AA7075. The analysis was performed after the in-situ measurement (i.e. after ungassing of the sample). Since non-conductive epoxy was used in Figure 3.10 for the sample preparation, conductive carbon tape was applied to make the sample electrically conductive.

3.2.3 Corrosion inhibition

The sample preparations for Section 4.3 will be evaluated in this section. This section begins by explaining the production of the accelerated corrosion test samples, followed by the sample preparation for the cycle measurements, whereby OCP, Linear Polarization Resistance (LPR) and Electrochemical Impedance Spectroscopy (EIS) are measured over time. This section concludes with the formation of the corrosion inhibitor solutions and production of the salt bridges both of which are used in the to test the protection of aluminium alloys under galvanic corrosion conditions.

Accelerated corrosion test

Samples used for the NSS (ASTM-B117) test were prepared as explained in the paragraph "Reproducing the galvanic effect". In addition to the clearcoat panels, various coatings with corrosion inhibitors were prepared and tested. These coatings are shown in Figure 3.11 and have been applied four times each to AA7075C, AA7475C and AA7475CTSA.

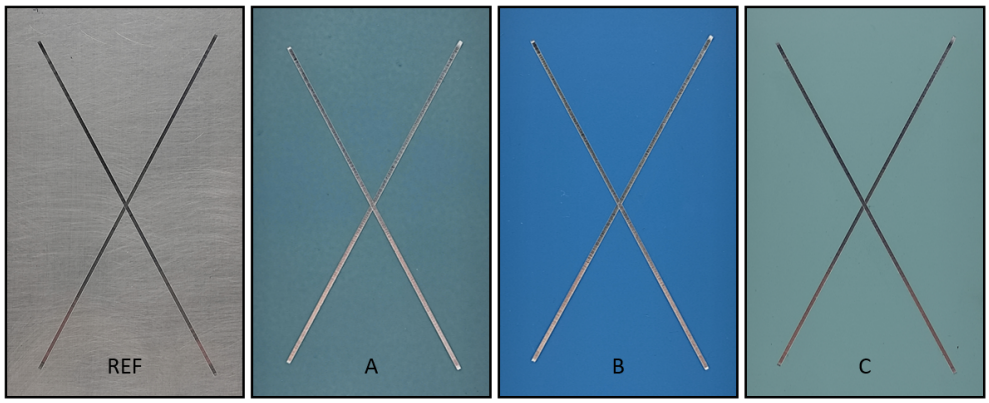

Figure 3.11: A reference clearcoat (REF) and various coatings with corrosion inhibitor (A,B, and C) applied on AA7075C, AA7475C and AA7475CTSA with pristine scribes

Coating A and B are lithium-based coatings containing different lithium salts. Coating C does not contain lithium, but another corrosion inhibitor. Further, to observe the influence of a thicker film, coating B was sprayed with different settings on AA7475C and AA7475CTSA, which is indicated with B2t. The thickness and standard deviation of the applied coatings is displayed in Table 3.3.

Table 3.3: Film thickness(t) and standard deviation(s).

	REF	A	B	C	B2t
AA7075C	t=12.3;	t=22.3;	t=24.5;	t=23.1;	-
	s=0.7	s=1.7	s=1.2	s=0.9	-
AA7475C	t=12.9;	t=25.8;	t=27.9;	t=24.1;	t=38.2;
	s=0.5	s=1.6	s=1.3	s=1.0	s=1.2
AA7475CTSA	t=16.3;	t=28.5;	t=30.5;	t=26.8;	t=37.8;
	s=0.9	s=1.2	s=1.4	s=1.0	s=1.7

Electrochemical measurements over time

The procedure of the measurements is explained in Figure 3.18, whereby the OCP, LPR and EIS is measured over time. A total of 36 samples were produced and tested in the cyclic measurement: four AA7075C panels per coating: REF, A, B and C and

four AA7475C panels per coating: REF, A, B, C and B2t. Prior to the measurements, 7 by 7cm samples were placed in the NSS for 168 hours to activate the corrosion inhibitors. The production of these panels were made according to the same procedure as explained in paragraph "Reproducing the galvanic effect". In addition, the same inhibitor coatings were applied with the same thickness and standard deviation as shown in Table 3.3. After the measurements over time, the panels were cut into pieces of approximately 8 by 2 cm to maintain the same mutual distance between the three electrodes during the ZRA measurement.

Corrosion protection of aluminium alloys under galvanic corrosion conditions

Inhibitor solution were made of Benzotriazole (BTA) and 2-mercaptobenzothiazole (2-MBT), as their inhibitor efficiencies have been shown to be higher than 90% on AA7075-T6 [6]. The corrosion inhibitors were obtained from Sigma-Aldrich: BTA (99%) and 2-MBT (97%). The inhibitor solutions were prepared in an aqueous 3.5% NaCl solution with the following concentrations: no inhibitor, 5mM BTA and 1mM 2-MBT. The concentration of 5mM is the minimum concentration needed to obtain reproducible corrosion inhibition with BTA, and due to the low solubility of 2-MBT in water, this concentration is limited to 1mM. The solubility in water of both inhibitors is 0.1mM/100mL for 2-MBT and 1.7mM/100mL for BTA [44].

To test the efficiency of the inhibitor separately on the cathode and the anode, galvanic cells were made. A requirement to split the cells and maintain conductivity is a salt-bridges, which had to be produced and tested prior to the measurements. The gel salt-bridges were made according to the procedure as explained in [62]. The following supplies were used for the production of the salt bridges:

- Flexible silicon tubes: 15cm x 1cm x 0.7cm (length x D_{out} x D_{in});
- 3M Potassium chloride (KCl) ;
- 4%(w/v) Agar ;
- 250mL borosilicate beaker ;
- A hot plate with magnetic stirrer ;
- Saturated KCl solution to store the Salt-bridges.

To produce circa four salt-bridges, 22.35g of KCl was first dissolved in 100mL of distilled water during heating. After boiling, 4.45g Agar was added while stirring the solution. The solution was then poured into the silicon tubes and cooled for about 1 hour before being placed overnight in the saturated KCl solution.

The salt-bridges produced were tested according to three different measurements. First, a quick and easy measurement was performed by measuring the potential difference that can be caused by the added resistance of the salt bridge. According to Ohm's law, if the resistance increases as the current remains the same, the potential also increases. Subsequently, if the potential difference was within an acceptable range, the solution resistance was measured at high frequency with an EIS measurement, whereby only the first x-axis intersections (solution resistance) in the Nysquist plot was relevant and used as a result (f=10^5-10^0Hz; 6points/decade). The change in solution resistance was measured when a salt-bridge was added, which is essentially a measure of the impedance of the salt-bridge itself. To check the acceptability of the measured impedance, a ZRA measurement was conducted with and without salt-bridge to test if the measured potential and current were in line. If this was the case, the rest of the salt-bridges were only tested by the first and second experiment, which increased the testing period without the need of different materials and sample preparations. In addition, prior to each experiment

the salt-bridge was freshly-cut at its tip by at least 5mm to eliminate its potential solution-history-dependent effect.

1. Potential difference
   The potential difference was first measured as a reference measurement with a multimeter between two Ag/AgCl (Sat'd KCl) RE in 3.5%NaCl, as shown in Figure 3.12a. Then, both RE were separated by a salt-bridge and the potential was measured as shown in Figure 3.12b. All salt-bridges tested obtained acceptable agreement within ± 0.5mV of the reference measurement.

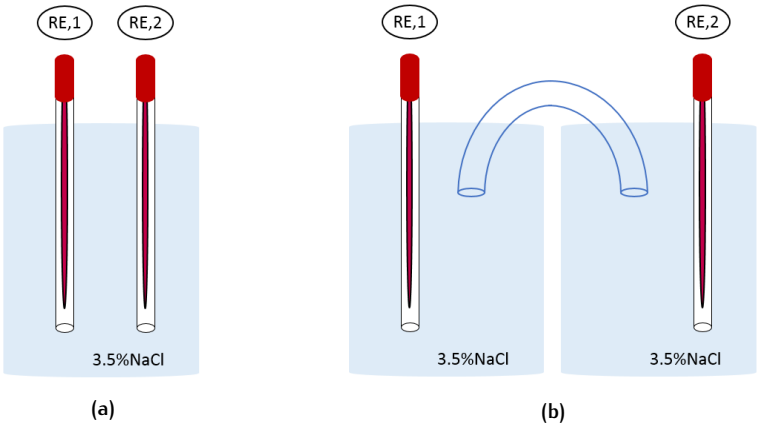

Figure 3.12: (a) Potential difference between two reference electrodes in the same solution. (b) Potential difference between two reference electrodes separated with a Salt-bridge.

2. Solution Resistance
   A solution resistance measurement was performed to determine the impedance of the salt-bridges. The experimental set-up is displayed in Figure 3.13a and Figure 3.13b. Both WE and Counter electrode (CE) are graphite electrodes where the CE electrode contains a larger surface area, inducing a current flow from the WE to the CE. For salt-bridges tested, an impedance of less than 260 ohms was measured.

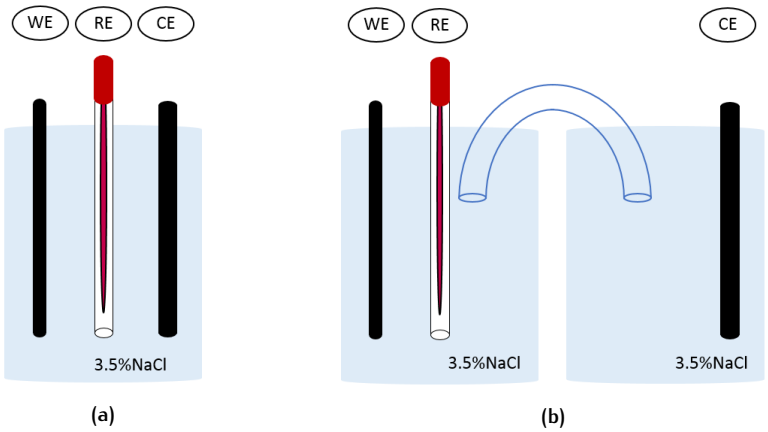

Figure 3.13: (a) Solution resistance measurement set-up in one cell. (b) Solution resistance measurement set-up in two cells with a salt-bridge.

3. Galvanic current measurement
   To check whether the impedance below 260 ohms is acceptable, a 16 hours ZRA experiment was performed with the experimental setup as shown in Figure 3.14a and Figure 3.14b. As WE a scribed AA7475C panel was used, and an embedded fastener as CE. First, the galvanic current and the mixed potential were measured with all electrodes in one cell. Thereafter, both parameters were measured in a two-cell setup, whereby the CE was separated from the RE and WE. The results are shown in Table 3.4, from which can be concluded that the measured parameters are in excellent agreement.

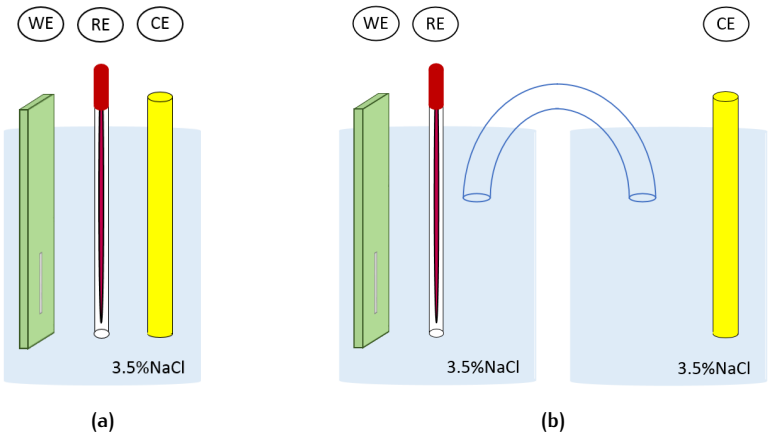

Figure 3.14: (a) ZRA measurement set-up in one cell. (b) ZRA measurement set-up in two cells with a salt-bridge.

Table 3.4: Salt-bridge check; ZRA results.

	I_{mean} (μA)	I_{rms} (μA)	V_{mean} (V vs. SHE)
Without Salt-bridge	1.02	0.07	-0.562
With Salt-bridge	1.05	0.08	-0.566

3.3 EXPERIMENTAL TECHNIQUES

This chapter evaluates the experimental techniques used in this thesis, with emphasis on the experimental set-up and relevant parameters.

Optical microscope

To observe the morphology and microstructure of the materials a digital optical microscopy (Keyence VHX-5000) with a 18 megapixel CCD camera is used. The scribe depth and clad thickness were both measured using the supported VHX-5000-900F software.

Open Circuit Potential and Potentiodynamic Polarization measurements

The OCP and PP measurements were performed using a potentiostat (Gamry Interface 1000) and an electrochemical cell with a three-electrode arrangement. The WE (samples) had various exposed area's, depending on the measured material, as displayed in Figure 3.5. The RE used is an Ag/AgCl (Sat'd KCl) electrode, and the CE is made of graphite. The mutual distance between the three electrodes was kept constant by a mold that was placed on top of the electrochemical cell. Moreover, the WE and RE were placed together as close as possible, to minimize the the affect of the solution resistance. Also, the WE was attached vertical to avoid salt formation or oxide accumulation on the exposed surface, as shown in Figure 3.15 when the sample was placed horizontally. Further, the potentiostats and RE were periodically calibrated and all measurements were performed with a constant amount of electrolyte and at an average temperature of 23°C.

Figure 3.15: A pure zinc sample after potentiodynamic polarization when placed horizontally.

In this thesis, OCP measurements have been performed for two specific purposes. The first to determine the equilibrium potential for each individual material, followed by potentiodynamic polarization measurements to determine the corrosion kinetics. These measurement were performed in 3.5% NaCl solution on the same potentiostat-cell for the best possible reproducibility. The most materials obtained a consistent OCP value within 2 hours of measurement. Except pure aluminium, which became stable after approximately 10 hours of measuring. All original materials were stable within $\pm 5mV$, and the potentials of the mixed materials within $\pm 10mV$. Anodic potentiodynamic polarization started 0.025V below the OCP and ended 0.25V above the OCP. Cathodic potentiodynamic polarization curves vice versa. Both potentiodynamic polarization measurements were performed at a scan rate of 0.167 mV/s, and were repeated at least three times per material.

The second OCP measurements were performed prior and during the cyclic measurements in 0.05M NaCl for screening. To start the cyclic measurement in equilibrium, the OCP was measured for 1 hour, and to check the stability before each individual cycle, OCP measurements of 900s were performed.

Scanning Electron Microscopy with Energy Dispersive X-Ray Spectroscopy

A Jeol JSM-IT100 Scanning Electron Microscope (SEM) was used to characterize the microstructure and to measure the chemical composition of the sample surfaces using the Energy Dispersive X-Ray Spectroscopy (EDS) probe. Both secondary and backscattered electron micrographs were taken in high vacuum to observe the microstructure. The SEM-EDS analysis was carried out with backscattered electrons to measure deeper into the bulk material and to avoid erroneous results due to a potential oxide layer or surface contamination. The micrographs and the EDS spectra were obtained with electron beam energy of 10keV and 20keV with a probe current between 62 and 82nA, depending on the image quality and the desired elements to detect. The working distance was kept constant at 10mm.

In-situ measurements

To observe the corrosion initiation and propagation in-situ, the experimental set-up as shown in Figure 3.16a was used. This set-up consists of two main parts, namely a LEICA DMLM optical microscope with an INFINITY1 Lumenera camera and a PC with INFINITY Analyse and Capture software. To observe corrosion in-situ on AA7X75C, a time-laps mode was used with an image taken every 20 seconds. After corrosion initiated and propagated, all images were compressed into a 1 minute video.

(a) (b)

Figure 3.16: (a) In-situ measurement set-up. (b) The red built-in cap and galvanic connected fastener.

A waterproof built-in cap with a thin microscope slide glued to one end was used as a protective cover for the microscope lens to prevent contamination from the electrolyte and maintain good resolution and focus of the sample. Any air bubble appeared on the sample's surface was removed with the aid of a pipette. In addition, to galvanically stimulate the corrosion on AA7X75C, a fastener was attached as shown in Figure 3.16b whereby the connection was controlled several times with a multimeter. In both in-situ experiments, a 3.5%NaCl solution was used as the conductive electrolyte.

Zero Resistance Ammeter: Electrochemical Noise

The galvanic current and mixed potential between the AA7X75C and fasteners were measured using a potentiostat in ZRA mode Electrochemical Noise (ECN). For this measurement, a potentiostat (Gamry Interface 1000) was used with an electrochemical cell in a three-electrode arrangement, as shown in Figure 3.14a. Hereby, it measures the galvanic current flowing between two electrodes, WE1 and WE2(=CE), which act as if they are coupled by a zero resistance wire. At the same time, the

potential of the galvanic couple is measured between the two working electrodes and the reference electrode. Since the galvanically coupled current and potential is dependent on the amount of cathode/anode area, it is important to keep both WE1 and WE2 exposed surfaces constant, which is achieved according to the procedure as explained previously in Figure 3.5 and Figure 3.6. Moreover, since a mixed potential of two dissimilar materials is measured, the result was declared valid only if the potential was between the two equilibrium potentials of both metals.

To obtain a continuous ECN measurement, the block time and repeat time were set equal. The measurements using single and multiple fasteners were performed with a duration of 4 hours. The corrosion inhibitor coatings were measured for 2 hours and the experiments with corrosion inhibitor solutions for 16 hours. The amount of solution was kept constant per experiment conducted.

Potentiostatic and Galvanostatic Polarization

In a laboratory setting, degradation of a material can be simulated by potentiostatic and galvanostatic polarization experiments. For this measurement, a potentiostat (Gamry Interface 1000) was used with an electrochemical cell in a three-electrode set-up. The RE used is an Ag/AgCl (Sat'd KCl) electrode, the WE a scribed AA7X75C specimen and the CE a graphite electrode as shown in Figure 3.17. In a potentiostatic polarization experiment, the desired potential between the WE and RE is kept constant by controlling the current across the WE and CE. In a galvanostatic polarization experiment, the applied current between the WE and CE is kept constant by controlling the potential across the WE and RE. In both experiments the initial values for current, potential and time were set to zero and only the final values were set. In addition, a 3.5%NaCl solution was used as electrolyte, and the experiments were performed from 24h to 168h.

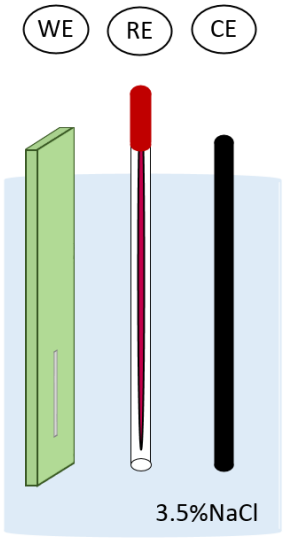

Figure 3.17: Potentiostatic and Galvanostatic polarization experimental set-up.

Electrochemical measurements over time procedure

The measurement procedure was performed to analyze the performance and galvanic corrosion protection of the inhibitor coatings when a damaged area was artificially created. The experimental procedure is displayed in Figure 3.18 and was also performed in this sequence.

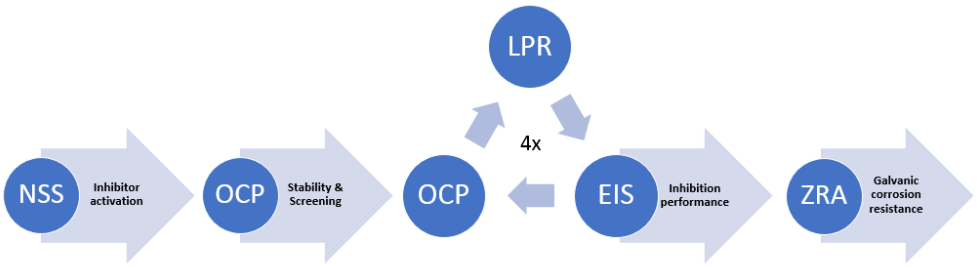

Figure 3.18: Full procedure of the electrochemical measurements conducted.

The full procedure is conducted four times for AA7075C with coatings: REF, A, B and C, and four time for AA7475C with coatings: REF, A, B, B2t and C, which means that in total 36 samples were tested. First, all panels were placed in the NSS (ASTM-B117) for 168 hours to activate the corrosion inhibitors in the coatings around the artificially damaged area. Then, one hour of OCP was performed in 0.05M NaCl to start the cyclic measurement at equilibrium. This OCP measurement and all experiments in the cycle were performed on a Gamry Interface 1000 potentiostat, using a three-electrode set-up equipped with a Ag/AgCl (Sat'd KCl) RE electrode and a graphite CE.

The measurements over time were repeated a total of four times per sample in 0.05M NaCl and started with a 900 seconds OCP measurement for screening. Next, a LPR measurement was performed with the initial potential of 10mV below the measured OCP, and with a final potential at 10mV above the previously measured OCP. The LPR was performed with a scan rate 0.125mV/s. The last experiment in the cycle is a EIS measurement, performed in a frequency range from 10^{-2} to 10^{5} Hz with a sinusoidal amplitude of 10mV. Each decade was split into 10 data points and each data point was determined as the average over two consecutive measurements. If the OCP values were aligned throughout the cycle, every fourth cycle was taken as the result.

At the end of the measurements over time, the inhibited scribed area's were monitored with a potentiostat in ZRA mode ECN. The procedure has been previously explained in more detail in the paragraph "Zero Resistance Ammeter: Electrochemical Noise" with the experimental set-up is shown in Figure 3.14b. The measurements were first conducted in 3.5% NaCl and then in 0.05M NaCl. Furthermore, ZRA measurement were performed with only 1/10th of the cathodic exposed area, in order to investigate the galvanic corrosion protection of the various coatings at lower cathodic currents.

4 RESULTS AND DISCUSSION

4.1 THE ROLE OF ZINC

The corrosion resistance of a clad layer is mainly due to the absence of secondary phases with different electrochemical properties than the aluminium matrix and therefore contains higher corrosion resistance properties than the underlying aluminium alloy substrate. It also acts as a sacrificial layer when the aluminium alloy substrate is exposed to an electrolyte in a damaged area. Specific to AA7X75C this clad layer is AA7072, with zinc being the most abundant alloying element. Although the general function of such a clad layer is well-known, the precise role of certain alloying elements is not yet fully understood on the corrosion initiation and propagation. Therefore, this chapter discusses the first main objective of this thesis, namely:

- What is the role of zinc in the Clad layer with respect to corrosion initiation and propagation?

A first impression of the corrosion behaviour of metals and alloys can be obtained by observing the Electrochemical series, which shows the order of standard electrode potentials of chemical elements in fixed standard conditions [63]. Pure zinc in this series has a more positive reduction potential than pure aluminium, meaning that when both materials are placed in an electrochemical cell, zinc tends to gain electrons, while aluminium tends to lose them. Beside the Electrochemical series, there is also a Galvanic series that shows the order of nobility of metals and semi-metals in a specific environment. For instance in seawater [64; 65; 66], where aluminium and zinc alloys have been widely measured and indicated in a wide potential range. In this series, the aluminium alloys generally have a higher potential than zinc, which means that zinc will corrode preferentially when both alloys are placed in an electrochemical cell. Since both series explain contrary behaviour and this mainly depends on specific metallurgical characteristics and environmental parameters, first the electrochemical behaviour of AA7072 and purely aluminium and zinc in 3.5% NaCl is measured and discussed by means of OCP and PP measurements.

Furthermore, Section 2.2 explained that in AA7075 the strengthening particles, $MgZn_2$, can dissolve during solution heat treatments, which causes a supersaturation of the elements Mg and Zn in the aluminium matrix. These elements can segregate toward the grain boundaries and are able to nucleate there, as these are preferential nucleation sites for the strengthening particles. Besides, the clad material is applied on AA7X75C by a hot rolling process which may allow diffusion of certain elements to or even in the clad layer [25; 67]. These processes arose a hypothesis for the phenomenon in Figure 1.1, because the selective corrosion degradation suggest that alloying elements, and especially zinc as the main contributor, could be heterogeneously distributed across the clad layer. Therefore, the microstructure of AA7075C and AA7475C(TSA) is exposed to an etchant to measure the exact thickness of the clad layer, followed by a SEM-EDS line scan to identify an element distribution across the substrate and clad layer.

4.1.1 Electrochemical behaviour of the clad layer

The electrochemical behaviour of AA7072, pure aluminium and zinc is investigated by means of OCP and PP measurements. The graph in Figure 4.1 displays the open circuit potentials of the tested materials, which is a measure of the corrosion thermodynamics. This provides a basis for the understanding of the energy changes associated with the corrosion reaction, which means in general, that it can predict when corrosion is possible. The rate at which the reactions proceed is governed by the corrosion kinetics, which is displayed in Figure 4.2 by means of anodic polarization curves. The open circuit potential (E_{ocp}), corrosion potential (E_{corr}) and current density (i_{corr}) values were derived from both graphs and are summarized in Table 4.1. To explain the role of zinc on the electrochemical behaviour of AA7072, it is assumed that the clad layer in AA7075C and AA7475C is equal in terms of these electrochemical parameters. Specific additional information of AA7072 per alloy is added to Appendix A.

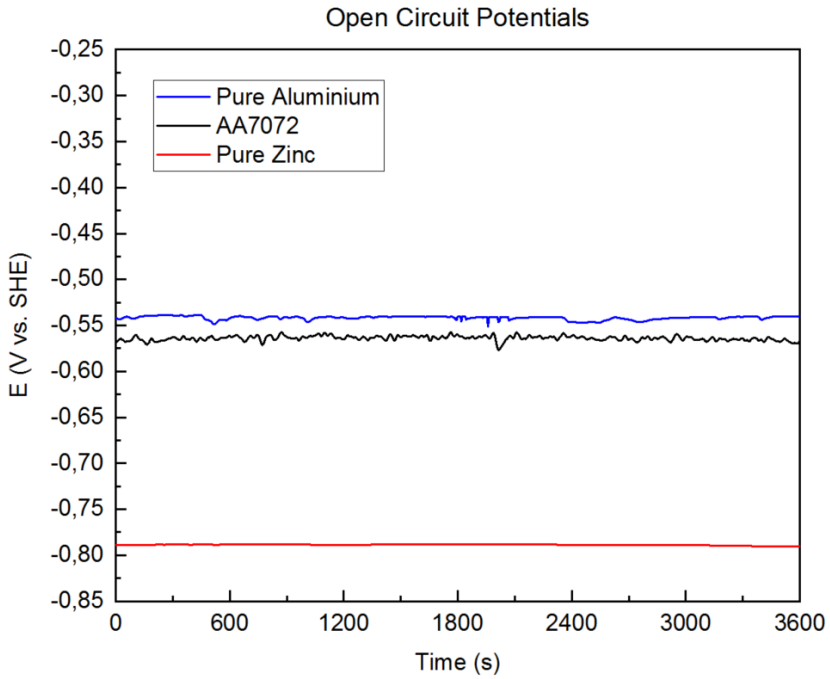

Figure 4.1: Open circuit potentials of AA7072, pure aluminium and zinc in 3.5% NaCl.

The last stable hour of the open circuit potentials is displayed in Figure 4.1. Pure aluminium exhibits the highest OCP among the metals tested with a value of -0.54V, followed by AA7072 with a value of -0.56V, and lastly pure zinc with a OCP of -0.79V. This means that when both pure metals are electrically connected in a galvanic cell, aluminium will behave as the cathode and zinc as the anode, causing it to dissolve preferentially. Further, it is known that the clad material is roughly made from 99%Al and 1%Zn. According to the equilibrium potentials this means that the addition of zinc decreases the equilibrium potential of AA7072, which is in agreement with the findings in Figure 2.10. Note that both pure metals contain a rather straight horizontal line, while in AA7072 more activity is ongoing between the alloying elements in the clad layer and therefore fluctuates around a constant OCP value.

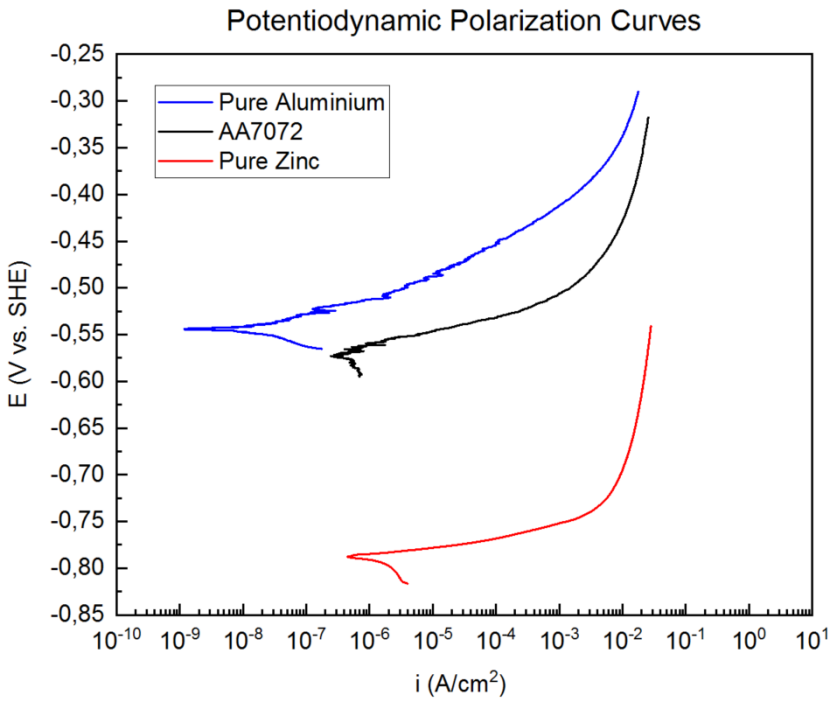

Figure 4.2: Anodic potentiodynamic polarization curves of AA7072, pure aluminium and zinc in 3.5% NaCl.

To get a complete perception of the electrochemical behaviour, anodic potentiodynamic polarization curves were conducted and are shown in Figure 4.2, with the corresponding derivative values in Table 4.1. The polarization curve of zinc and AA7072 clearly exhibits an active behaviour where pitting starts immediately. Aluminium also shows active behaviour, however it is less aggressive behaviour compared to the curve of AA7072 and pure zinc. It is obvious that a generous difference can be observed in the current density between the measured metals. Especially between aluminium and zinc, where zinc has a current density approximately 80 times higher than that of aluminium. This means that not only zinc will dissolve preferentially upon coupling, but also at a much higher rate than aluminium. Hence, zinc is the main potential contributor to the increase in corrosion rate of AA7072.

Table 4.1: Electrochemical parameters obtained from OCP and PP measurements of AA7072, pure aluminium and zinc with standard errors

	Eocp (V)	Ecorr (V)	icorr (A/cm^2)
Aluminium (99.99%)	-0.54 $\pm$0.01	-0.54 $\pm$0.01	2.1 $\pm$0.7 x 10^{-8}
AA7072	-0.56 $\pm$0.00	-0.57 $\pm$0.00	4.8 $\pm$0.3 x 10^{-7}
Zinc (>99.95%)	-0.79 $\pm$0.00	-0.79 $\pm$0.00	1.7 $\pm$0.1 x 10^{-6}

4.1.2 The microstructure and clad layer thickness

The microstructure was studied to find the clad thickness of the as received aluminium alloys. To highlight the microstructure of AA7075C, AA7475C and AA7475CTSA the samples were exposed to an etchant for a certain time period as explained in Section 3.2. The microstructure and surface characteristics of the alloy substrates are indistinguishable from each other, as shown in Figure 4.3b, Figure 4.3d and Figure 4.3f, and all contain an elongated microstructure in the rolling direction of the panels. In addition, the substrates contain clearly a polycrystalline

microstructure, while in the clad layer this microstructure is not observed. This makes the alloys obvious to distinguish after using the appropriate etchant. Additional information about the particles present on the substrate surface is added to Appendix B.

The clad thickness on all alloys differ is size, because it is typically between 2-10% of the substrate thickness as it needs to provide a sufficient absolute thickness of the overall structure [25; 40]. The AA7475C(TSA) panel thickness is 60% more than that of the AA7075C panels, which makes the clad layer in general also thicker. Although, this is not always the case as can be seen in the micrographs. The clad thickness, as shown in Figure 4.3a, Figure 4.3c and Figure 4.3e is an average of a total of 60 measurements on three different samples per alloy to obtain the most representative values as possible. The thickness of the clad layer measured in AA7075C is 48 µm ± 4 µm, in AA7475C it is 50 µm ± 4 µm and in AA7475CTSA it has a thickness of 76 µm ± 6 µm.

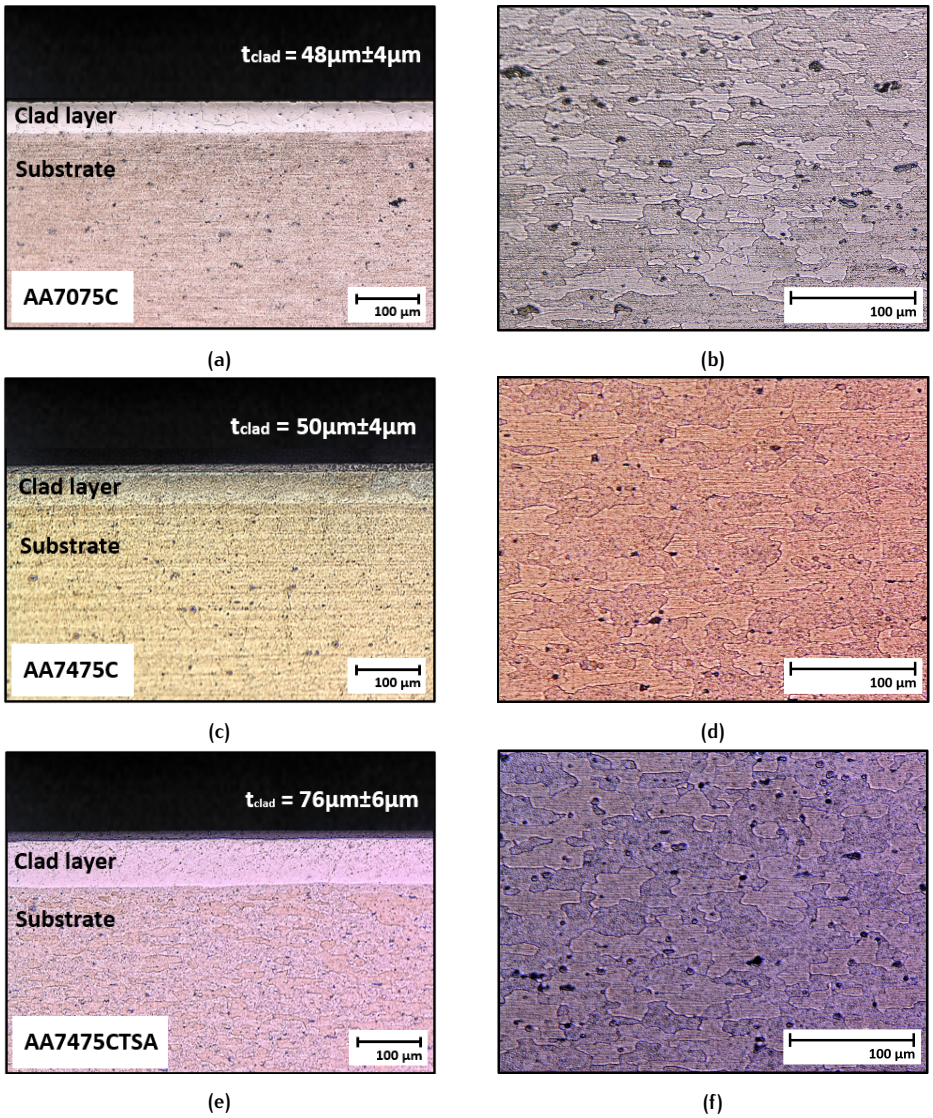

Figure 4.3: Micrographs (a) and (b) show the clad layer thickness of AA7075C and the microstructure of AA7075B, respectively. Micrographs (c) and (d) show the clad layer thickness of AA7475C and the microstructure of AA7475B, respectively. Micrographs (e) and (f) are the clad layer thickness of AA7475CTSA and the microstructure of AA7475BTSA, respectively.

4.1.3 Determination of an element distribution

The zinc distribution along AA7X75C is measured with SEM-EDS in Backscattered Electron Composition (BEC) mode. This measurement was performed with a probe current between 78-82nA and an accelerating voltage of 10keV to exclude potential overlapping between ZnKα and CuKβ [68]. Note, that the maximum amount of both elements therefore could not be detected. The detected elements per point are added in Appendix C.

The SEM-EDS line scan on AA7075C is shown in Figure 4.4. A total of five lines with 10 data points per horizontal line were measured, but to find a potential distribution of certain elements over the AA7075C material, an average value of the five vertical points was calculated and displayed in Table 4.2. From the SEM image, a clear distinction can be observed between the substrate material and the clad layer, in which no grain boundaries and a much darker appearance is visible. Since no hard transition line can be seen, the minimum and maximum clad thickness as measured in Figure 4.3a is delineated with a grey dashed frame. Further, the amount of zinc in the substrate material should have a theoretical value between 5.1 and 6.1 wt%, which corresponds at least to the vertical lines (Vline) from 1 to 3. Vline 5 to 10 corresponds at least to the AA7072 clad material with a theoretically maximum amount of 1.3 wt%Zn.

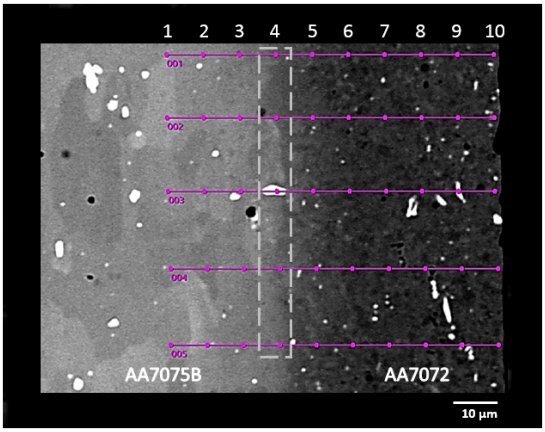

Figure 4.4: SEM-EDS linescan on AA7075C.

The measured amount of oxygen across all data points is fairly constant and can be attributed to the oxide layer on the alloy surface. The amount of aluminium gradually increases from the Vline 1 to 10, with some exceptions where a peak in Fe and Cu is detected. Especially, in the transition region (Vline 4, line 003), a large amount of Fe and Cu is detected, indicated with a white spot in Figure 4.4, which is most likely a measured Fe and Cu-rich intermetallic particle. In addition, in Vline 10, an unexpected increase in Fe is detected that is only measured at a single point (on purple line 005). No clear explanation can be found for this result. Further, the average amount of Mg detected in the substrate materials agrees well with the theoretical values. In Vline 4 and 5 only a slight increase in the transition region and the clad layer is observable, which is actually only caused by the detected Mg elements in the first horizontal line (001). On this line, point 4, 5 and 6 contains a Mg content of 1.6, 0.8 and 0.3 wt%, respectively. This means that a higher amount of Mg on this line is detected in the transition and clad region than theoretically reported.

The element zinc has only been detected in the Lα shell, and shows a gradual distribution along the AA7075C material. On average the amount zinc detected in the substrate material between Vline 1 and 2 corresponds to the theoretical minimum

value, likewise the measured values in the clad material between Vline 7 and Vline 10. However, between Vline 3 and 6 there is a transition in the amount of zinc detected along all the individual measured lines. This means, especially considering Vline 5 and 6, which are undoubtedly the clad layer, that there is an area in the clad layer of AA7075 where the zinc content is generously higher than the claimed theoretically value. In addition, the Na(K) characteristic X-rays can interfere with Zn(L) and Cu(L) and thereby increase the detected amount of zinc if Na was excluded during the measurement [68]. Since Na is not present in the polishing paste or solvent.

Table 4.2: Average mass% of elements detected by SEM-EDS of the 10 vertical regions. The transition region in the clad layer is indicated between the dashed lines.

	O(K)	Al(K)	Fe(L)	Cu(L)	Si(K)	Mg(K)	Zn(L)	Na(K)
Vline 1	0.3	92.0	0.0	0.0	0.0	2.3	5.2	0.1
Vline 2	0.2	91.2	0.0	0.8	0.0	2.2	5.1	0.4
Vline 3	0.6	92.2	0.0	0.3	0.0	2.0	4.4	0.5
Vline 4	0.4	87.3	7.3	1.4	0.0	0.3	3.7	0.3
Vline 5	0.7	96.0	0.3	0.1	0.2	0.2	2.3	0.3
Vline 6	0.5	97.9	0.0	0.1	0.0	0.1	1.5	0.0
Vline 7	0.6	98.3	0.0	0.0	0.0	0.0	1.1	0.0
Vline 8	0.4	98.6	0.0	0.0	0.0	0.0	1.0	0.0
Vline 9	0.5	98.5	0.0	0.0	0.0	0.0	1.0	0.0
Vline 10	0.7	97.2	1.1	0.0	0.0	0.0	1.0	0.0

The linescan performed on AA7475C is shown in Figure 4.5. A total of five lines with 11 data points per horizontal line were measured, but to find a potential distribution of certain elements over the AA7475C material, an average value of the five vertical points was calculated and displayed in Table 4.3. In the SEM image, a clear distinction can be made between the substrate material and the clad layer but no hard transition line can be observed. Therefore, the minimum and maximum clad thickness as measured in Figure 4.3c is delineated with a grey dashed frame. Further, the amount of zinc in the substrate material should have a theoretical value between 5.2 and 6.2 wt%, which corresponds to the vertical lines (Vline) from 1 to 5, whereby Vline 5 is on the edge of the maximum measured clad layer thickness. Vline 6 to 11 corresponds to the AA7072 clad material with a maximum amount of 1.3 wt%Zn, with Vline 6 on the minimum measured clad thickness.

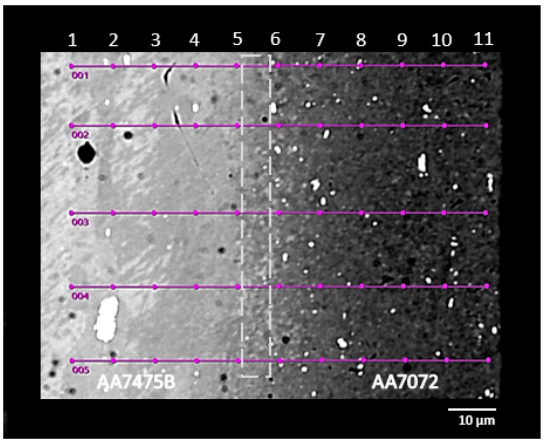

Figure 4.5: SEM-EDS linescan on AA7475C.

In Table 4.3 the average mass% of the elements detected by the linescan is displayed. Note that other elements, including Na and O, are excluded during the measurement, which are therefore counted at the closest peak of a detected element. The amount of aluminium shows a stable increase across the AA7475C surface. The amount of alloying elements in the substrate material are in good agreement with the theoretically reported values. However in the clad layer, a similar transition region as in AA7075C is measured, with the amount of certain elements (i.e. Cu, Mg and Zn) exceeding the theoretically reported values. Especially in the region between Vline 7 to Vline 9, a marked increase in the amount of Mg and Zn is detected, which is undoubtedly the material of the clad layer.

Table 4.3: Average mass% of elements detected by SEM-EDS of the 11 vertical regions. The transition region in the clad layer is indicated between the dashed lines.

	Al(K)	Fe(L)	Cu(L)	Si(K)	Mg(K)	Zn(L)
Vline 1	89.0	0.1	2.0	0.1	2.4	6.5
Vline 2	89.1	0.0	2.1	0.2	2.3	6.4
Vline 3	89.5	0.1	2.0	0.0	2.2	6.1
Vline 4	90.4	0.1	1.8	0.0	2.0	5.7
Vline 5	91.6	0.1	1.5	0.1	1.8	5.0
Vline 6	93.2	0.1	1.1	0.1	1.4	4.2
Vline 7	95.2	0.1	0.5	0.1	0.9	3.2
Vline 8	96.5	0.2	0.3	0.1	0.5	2.5
Vline 9	97.7	0.0	0.1	0.1	0.3	1.8
Vline 10	98.1	0.1	0.1	0.1	0.1	1.5
Vline 11	98.3	0.1	0.1	0.1	0.1	1.4

This means that on both aluminium alloys in the clad layer a transition region of zinc is present along the substrate and clad layer interface. This region suggest to be the selective dissolution path observed in the phenomenon in Figure 1.1.

4.1.4 Discussion

Given the results of the OCP and PP experiments, zinc is the preferred element that dissolves when coupled to aluminium in 3.5% NaCl solution. Also, it has been found that zinc dissolves much faster than aluminium. The clad layer contains a higher corrosion resistance than the core alloy due to the absence of microstructural phases such as intermetallic particles in the microstructure[25]. Therefore, zinc is probably present as a substitutional atom in the aluminium matrix [69]. Dissolution of zinc in the aluminium matrix causes an increase in the amount of aluminium on the exposed surface. After the PP measurements of AA7072, a pH of around 5.5 was measured in the solution, which suggests that aluminium is still in the passivation range [70]. Therefore, the aluminum will try to passivate at the same time as zinc dissolves and reduces the corrosion rate of the clad layer. However, it will not completely inhibit the corrosion degradation due to the presence of chlorides, which are known to weaken the oxide layer formed, causing pitting [71]. Moreover, other alloying elements in AA7072, such as Cu, Fe and Mg, can be exposed to the electrolyte and accelerate the corrosion rate of the aluminium matrix or preferably dissolve on its own. In this way, new galvanically coupled zinc atoms will be repeatedly exposed to the electrolyte, continuing the dissolution of the clad layer.

A distribution of the element zinc has been measured in the AA7072 clad material. Also, a higher content of this element has been found in AA7072 than theoretically reported. This means that diffusion has taken place from the core alloy to the clad material, which is known of the elements Zn and Mg in AA7075-T6 during solution heat treatments when a supersaturated solution in the aluminium matrix is reached. Diffusion of these elements could have occurred during the application of the clad layer by the hot-rolling process, or when a specific temper was applied [67; 72]. In addition, the distribution of zinc is measured across the entire measured surface, which creates an anodic path in the clad layer material. Therefore, the increase of zinc in this transition region can be the main contributor to the selective dissolution of the clad layer that is observed in the phenomenon.

Further, a clear variation in amount of certain elements can be observed in AA7072 when applied on AA7075B or AA7475B. This means that while AA7072 should be the same aluminium alloy on both substrates, its composition can change due to diffusion processes. It is therefore possible that dissolution of this clad layer is also different on different substrates.

4.2 THE GALVANIC CORROSION BEHAVIOUR

The selective dissolution phenomenon in Figure 1.1 occurred under galvanic corrosion conditions. Gaining knowledge about this corrosion process in general, and this selective dissolution phenomenon in particular, is essential and forms the foundation for the protection of the aluminium alloys against this type of degradation. Therefore, in this chapter the second main objective of this thesis is discussed:

- How do 7XXXC alloys behave under galvanic corrosion conditions?

The first step to actually simulate a representative galvanic effect is to determine all dissimilar materials involved into a galvanic system. Depending on the potential differences between them, which is the driving force for accelerated corrosion attack, one materials will behave as the anode, preferentially sacrificing itself, and the other as the cathode where the galvanic effect is inhibited. In a galvanic system the surface ratio of materials that share a common electrolyte is important, which predominantly determines the rate of corrosion attack on the anode material. Therefore, the reproduction of a representative galvanic system with a constant cathode-to-anode ratio is first evaluated. Subsequently, the electrochemical behaviour of the materials is determined by means of OCP and PP with the verified constant cathode-to-anode ratio. Although an estimation of the coupled parameters can be obtained from these measurements, the precise galvanic parameters are also measured by an ECN experiment in ZRA mode.

Simulating the galvanic corrosion degradation requires experiments that are as representative as possible with the reality. Nowadays, several test are used as standards, but no conventional tests can reproduce the exact environmental conditions, i.e. temperature and UV-light fluctuation, dry and wet cycles, and other phenomena of nature. Therefore in order to reproduce the galvanic corrosion degradation, electrochemical laboratory tests are performed, whereby repeatedly a constant galvanic degradation of the clad layer material can be simulated. In addition, it is known that natural corrosion processes can initiate and propagate over years, which consumes generally too much valuable time for research. Therefore, in order to obtain quick yet representative result, the galvanic corrosion experiments are performed in several practical useful time frames.

The last experiments in this chapter involves monitoring the galvanic corrosion in-situ. This is done to further enhance the understanding of the behaviour of AA7X7C alloys under galvanic corrosion conditions by visually observing the continuous galvanic corrosion process in detail. After this experiment, increased understanding is obtained about the galvanic corrosion behaviour in AA7X75C alloys, which forms the basis to create reliable and robust galvanic corrosion protection technologies.

4.2.1 Reproduction of the galvanic effect

The galvanic effect is reproduced according to a realistic application in the aerospace industry. The fasteners as received are measured and constructed in SolidWorks [61], as illustrated in Figure 4.6. In this situation the worst case scenario is illustrated if no sealant is left between the fastener and the panel surface. The beneficial effect of a corrosion inhibitor coating is also excluded and the fasteners are CCC striped before used. This created a reference model to determine the cathode-to-anode ratios, which is displayed in the column "Reference" in Table 4.4. First, the cathode-to-anode ratio in the reference model between the substrate material and the clad layer in AA7X75C(TSA) was measured, which can differ due to the difference in panel thickness. Then, it was assumed that the exposed area of the fastener is equal to the exposed area of the alloy and that both cathodes (e.g. substrate materials and the fastener) collaborate with the galvanic acceleration on the clad layer. This worst case cathode-to-anode ratio was calculated and has been added to the table for the aluminium alloys used.

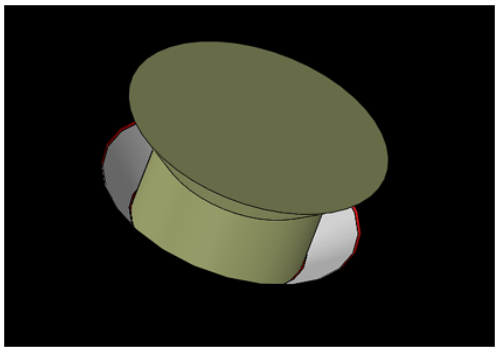

Figure 4.6: Schematic illustration of the reference model.

Reproduction of the reference model makes it possible to perform electrochemical experiments with the desired cathode-to-anode ratio, and is explained in Chapter 3. The created cathode-to-anode ratio per alloy material are shown in Table 4.4 in the column "Reproduction". From this table it can be seen that the produced ratios of AA7075C are in good agreement with the reference ratios. The produced cathode-to-anode correlations of AA7475C(TSA) are approximately half of the values with respect to the reference. The reproduced cathode-to-anode ratio of AA7075C and AA7475C is similar, therefore the degradation of both aluminium alloys can be compared.

Table 4.4: Cathode-to-anode ratios of the reference and the reproduction models of AA7X75C(TSA) with a scribe depth between 250-300μm.

Cathode/Anode ratios	Reference	Reproduction
AA7075C	20	16-18
AA7475C	32	16-17
AA7475CTSA	21	10-11

4.2.2 Electrochemical behaviour of a galvanic couple

The electrochemical behaviour of AA2017A and the scribed specimens: AA7075C and AA7475C, is investigated by means of OCP and PP experiments. Figure 4.7 displays the open circuit potentials of the tested materials. The potentiodynamic polarization curve can be observed in Figure 4.8. In addition, the values of open circuit potential (E_{ocp}), corrosion potential (E_{corr}) and the measured current (Im) were derived from both graphs and are summarized in Table 4.5.

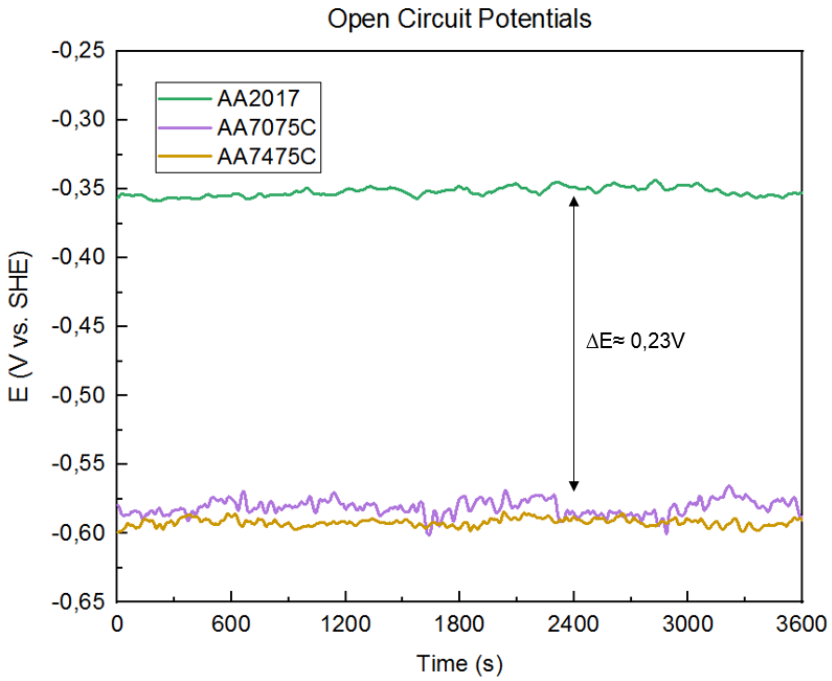

Figure 4.7: Open circuit potentials of AA2017A, AA7075C and AA7475C in 3.5% NaCl. The potential difference between AA2017 and AA7X75C is approximately indicated in the graph.

Figure 4.7 shows a clear distinction between the potential of the fasteners and both scribed aluminium panels. The OCP of AA2017A is -0.35V, and for AA7075C and AA7475C a value of -0.58V and -0.59V is measured, respectively. The potential difference between dissimilar materials is the driving force for an accelerated corrosion attack on the anodic material. When coupled, the metal with the most negative potential behaves as the anode while the other metal acts as the cathode. This leads to dissolution of the anodic metal into the electrolyte and inhibition of corrosion on the cathode. In this case roughly a potential difference of 230mV is measured between the fastener and aluminium scribed panels, meaning the fastener will behave as the cathode and the scribed panels as the anode upon coupling. Note that the OCP of the alloys AA2017A is rather constant, whereas the OCP of both mixed materials fluctuates around a constant value. This means that there is more activity in the mixed samples during measuring, which was expected because a certain ratio of the exposed areas of two different alloys is measured.

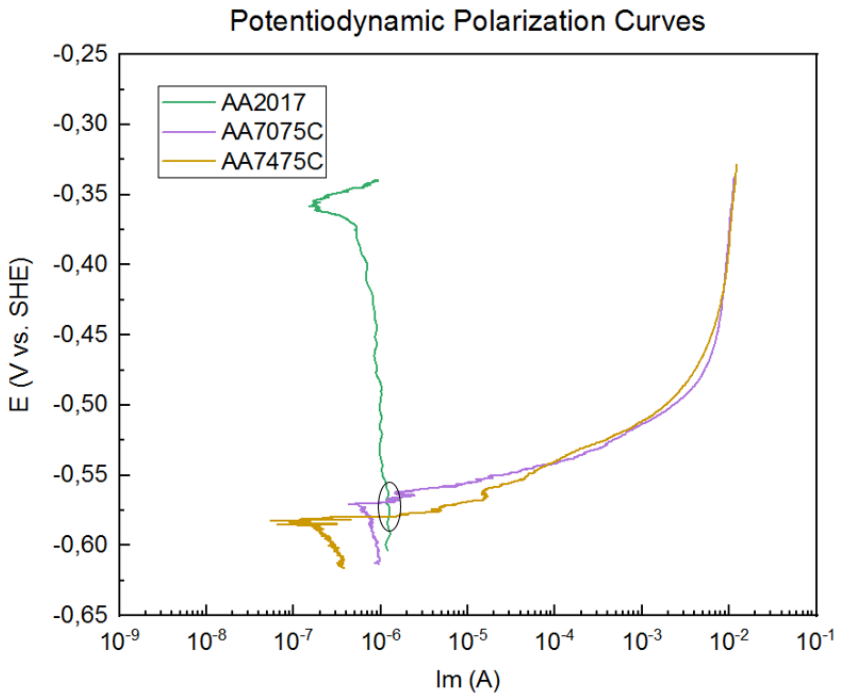

Figure 4.8: Potentiodynamic polarization curves of AA2017A, AA7075C and AA7475C in 3.5% NaCl. The intersections between the cathodic branch of AA2017 and the anodic branches of AA7X75C is indicated by the circle.

To observe the corrosion kinetics, PP curves are created as shown in Figure 4.8 with the corresponding values displayed in Table 4.5. Note that only the cathodic branch is plotted for AA2017A, whereas the anodic branch is shown for both mixed materials. This is done deliberately to find the intersection of those branches through Tafel extrapolation. The intersection between a cathodic branch and an anodic branch of two dissimilar metals is an estimation of the coupled parameters in a galvanic system, which is of particular interest in this case. On the x-axis, where usually the current density plotted, currently the measured current (Im) is shown. This measured current is determined by the exposed areas in the cathode-to-anode ratio as displayed in Table 4.4. This means that when the fastener is coupled with AA7X75C under the specified ratios, the galvanic coupling parameters can be estimated from the intersections of both curvatures. The intersection area defined by the maximum and minimum intersection values of multiple measurements is for AA7075C: -0.56 $\leq$ Potential(V) $\leq$ -0.57 and 1.0 $\leq$ Current(μA) $\leq$ 1.5, and considering AA7475C: -0.56 $\leq$ Potential(V) $\leq$ -0.60 and 1.0 $\leq$ Current(μA) $\leq$ 1.6.

Table 4.5: Electrochemical parameters obtained from OCP and PP measurements of AA2017A, AA7075C and AA7475C with standard errors

	Eocp (V)	Ecorr (V)	Im (A)
AA2017A	-0.35 $\pm$0.00	-0.36 $\pm$0.00	3.8 $\pm$0.5 x 10^{-7}
AA7075C	-0.58 $\pm$0.00	-0.57 $\pm$0.00	6.8 $\pm$0.0 x 10^{-7}
AA7475C	-0.59 $\pm$0.01	-0.58 $\pm$0.01	2.3 $\pm$0.6 x 10^{-7}

4.2.3 Measuring the coupled galvanic parameters

The potentiodynamic polarization curves as shown in Figure 4.8 give a first perception of the galvanically coupled parameters, indicated by the intersections of the anodic and cathodic curves. However, the range created by taking minimum and maximum values between multiple measurements is too large if an accelerated reproduction of the galvanic effect is required in a laboratory setting. Therefore, a measurement was established to find the galvanic current and the mixed potential of the galvanic system. These coupled parameters are measured by an ECN experiment in ZRA mode. Hereby, the galvanic current is measured between the WE,1 (Scribed AA7075C sample) and WE,2 (Fastener) in the ratio explained in Table 4.4. The mixed potential is measured between both working electrodes and the RE.

This measurement is only performed on AA7075C, because the cathode-to-anode ratio is the most representative one among the different aluminium alloys. In addition, the measurements are also conducted with larger cathode area's (e.g. 2x and 4x), to find the effect of a greater cathodic area when larger fasteners are used. The measurements are performed on various fasteners and combinations, as shown in Figure 3.8. At least three measurements were executed for each number of fasteners with a duration of 4 hours. As a reference measurement, all fasteners were taped, measuring a coupled galvanic current of zero and a mixed potential in line with the potential of AA7075C. The average of the most representative values are summarized in Table 4.6.

Table 4.6: Galvanic coupled parameters measured with the Electrochemical noise experiment in ZRA mode.

AA7075C	Current (μA)	Irms (μA)	Mixed potential (mV)	Vrms (mV)
+ 1 fastener	1.4	0.1	-562	2
+ 2 fasteners	3.0	0.2	-554	1
+ 4 fasteners	6.9	0.4	-552	1

From Table 4.6 it can be concluded that the measured current and mixed potential is in excellent agreement with the intersection range of the potentiodynamic polarization curves. The addition of second fastener doubled the exposed cathodic surface. This results in an induced current that is also about twice as large. By then adding two more fasteners, the induced cathodic current is again increased by more than 4 times the cathodic current induced by one fastener. Note that by increasing the number of fasteners also the root mean square (Irms) of the current increases, meaning that more noise is measured when more fasteners are used. This can be contributed to the mutual interaction of the fasteners, as they can behave slightly anodic or cathodic with respect to each other. According to Feng and Frankel [73], and because this mutual interaction between the fasteners, doubling the amount of exposed cathodic area should actually increase the cathodic current by slightly less than double. However, between all measurement, the sample is lightly sanded with 2000 and 4000grid sanding paper. This increased the amount of exposed surface by about 10% from the first to the last measurement, which is the reason that some measurements of the coupled current can be slightly more than twice. Furthermore, the addition of multiple fasteners increased the measured mixed potential. This trend was expected, because as the cathodic area increases, the cathodic branch in Figure 4.8 will shift to the right. This results in an intersection of the AA7075C branch at a higher potential, which becomes approximately the new mixed potential of the galvanic coupled system.

4.2.4 Simulation of galvanic corrosion

In this section, the galvanic corrosion is simulated in laboratory conditions while immersed in 3.5%NaCl solution. First, a reference experiment is performed by mechanically coupling the fasteners to the scribed panels for 168h. Subsequently, the galvanic parameters are applied experimentally after determining the coupled parameters in the previous section. The galvanic corrosion is induced with electrochemical experiments on AA7075C to find whether the same corrosion degradation occurs as in the reference model while being forced. Finally, the corrosion mechanism is observed in-situ to evaluate the corrosion process in detail.

Reference measurement when coupled with a fastener

The galvanic effect can be most representatively simulated in fully immersed condition when the actual materials are connected in a particular exposed cathode to anode ratio. In this way, the natural interaction between the alloys is preserved, meaning that fluctuating, unconstrained galvanic parameters cause the corrosion degradation. Therefore, as a reference measurement, scribed panels of AA7075C, AA7475C and AA7475CTSA were mechanically coupled with a fastener in a 3.5% NaCl solution for 168 hours. The cross-sections of the main blister formed per alloy are shown in Figure 4.9. In Figure 4.9a, AA7075C is shown which clearly exhibits the most corrosion degradation among the aluminium alloys. However, it is not entirely clear how corrosion initiated and propagated, as the degree of degradation quickly became too severe. Figure 4.9b shows less degradation compared to AA7075C. Only a few corrosion spots in the clad layer are observed here. This selective degradation is more similar to the degradation mechanism observed in the phenomenon, as in some spots corrosion is clearly found only in the transition regions. The aluminium alloy with the least degradation is visible in Figure 4.9c, where only a minor amount of corrosion appears at the clad layer and electrolyte interface. This can be explained by the fact that the TSA layer increases the adhesion of the coating to the substrate, allowing a small amount of solution and accumulation of chlorides to penetrate between the coating and the clad layer.

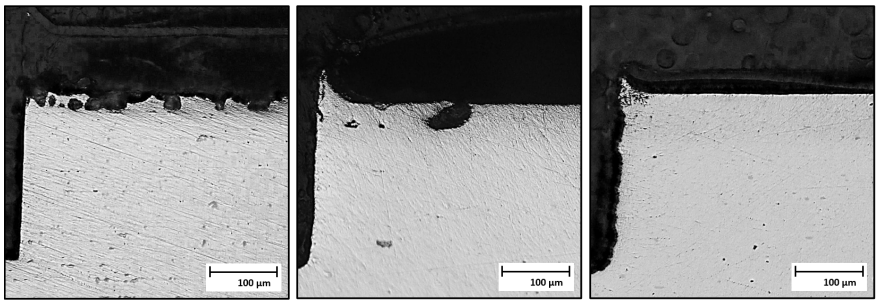

Figure 4.9: Scribed samples fully immersed in 3.5%NaCl while coupled with a fastener for 168h: (a) AA7075C; (b) AA7475C; (c) AA7475CTSA.

Electrochemically induced galvanic current

As discussed in the previous section, the galvanic effect can be most representatively simulated in fully immersed condition when the materials themselves are connected. However, this takes weeks in measuring time and sample preparation. Therefore, electrochemical experiments have been investigated which are potential experiments in simulating the galvanic effect.

Two well-known experiments have been performed on AA7075C, namely potentiostatic polarization and galvanostatic polarization. The experimental setup is for

both experiments the same, as explained in Section 3.3. In the first experiment, the potential of the WE can be set to a desired constant value, by automatically adjusting the current between the WE and CE. In this measurement, the sample is polarized till the mixed potential for 72h, which is approximately 15mV above the OCP of AA7075C. The results showed that the current required to maintain this constant potential difference were unexpected negative currents at certain time intervals, meaning that at these intervals only corrosion degradation on the cathode (CE) occurred. This unrealistic current direction can be explained by the combination of the relatively small potential difference applied to the anode and the fluctuation range in potential of AA7075C during the potentiostatic polarization experiment. In addition, a slight increase in the potential difference resulted in a fast increase in current and degradation of the clad layer due to the anodic behaviour of AA7075C, as shown in Figure 4.8. As a result, the galvanic degradation cannot be reproduced with repeated experiments. Therefore, galvanostatic polarization experiments have been tested and applied to simulate the galvanic effect. To show the working principle of a clad layer, first AA7075B and AA7075C were tested. The sacrificial protecting effect of a clad layer is shown in Figure 4.10, whereby it dissolves preferentially and protects the substrate material.

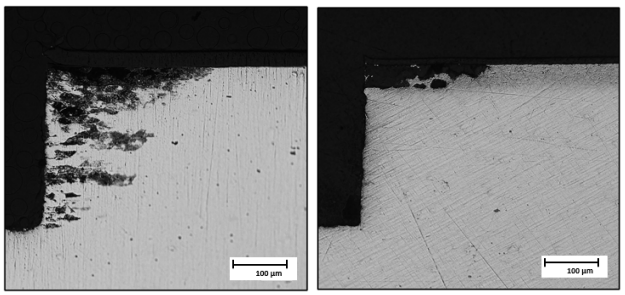

Figure 4.10: Galvanic corrosion degradation of the defect area: (a) without, and (b) with clad layer on AA7075 in 3.5%NaCl.

In galvanostatic polarization experiments, the current between WE and CE can be kept constant by adjusting the potential between the WE and RE. First, a constant current of 1 μA was applied for 168h, as shown in Figure 4.11a. To accelerate the galvanic corrosion degradation, experiments were also performed with 50 μA for 72 hours and even with 100 μA for 24 hours experiment, as shown in Figure 4.11b and Figure 4.11c, respectively. In all three experiments comparable degradation of the clad layer can be observed, which corresponds to the reference experiment in Figure 4.9a. Therefore, it can be concluded that simulation of galvanic corrosion in the clad layer can most representatively be achieved by galvanostatic polarization, even in applied accelerated conditions.

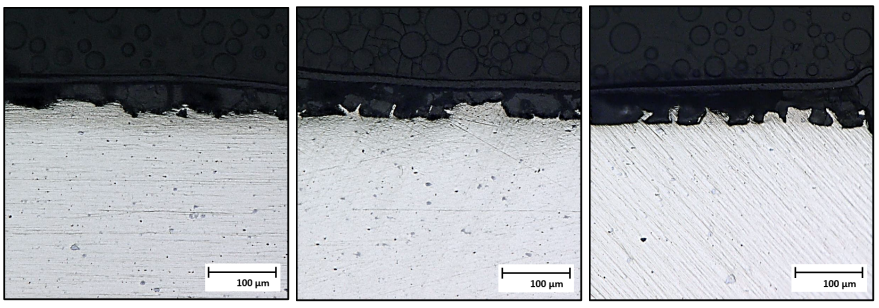

Figure 4.11: Galvanostatic polarization AA7075C: (a) 1μA for 168h; (b) 50μA for 72h; (c) 100μA for 24h.

The observation of galvanic corrosion in-situ

In the previous section it was discussed how the galvanic corrosion degradation can be simulated repeatably in the clad layer material. Also, it can be observed that the corrosion process is still too fast, causing in some spots the entire clad thickness to dissolve instead of the selective propagation as observed in the phenomenon. In addition, corroded samples can only be observed at the end of an experiment where many important information about the process has not yet been observed. Therefore, an experimental set-up was made to observe the corrosion process through the clad layer material in-situ. In this way, the corrosion process can be followed step by step because pictures are taken at specified intervals during the entire experimental time. After the experiment, the pictures are combined in a video to follow the exact order of degradation. The first scribed material monitored is AA7075C, as shown in Figure 4.12. A cathodic current with an external fastener is applied for approximately 6.5 hours, with a current slightly fluctuating around 50μA.

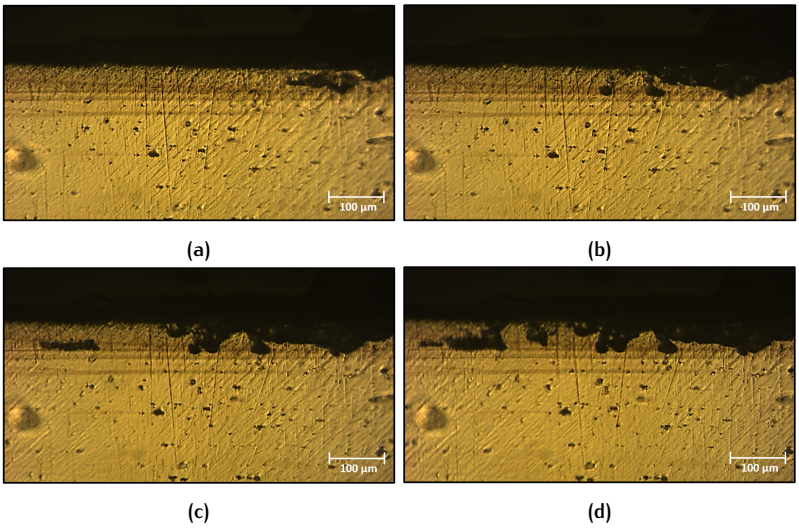

Figure 4.12: Galvanic corrosion of AA7075C monitored in-situ while stimulated with 50μA for 6.5h. Sequence of degradation after: (a) $\pm$2h, (b) $\pm$3h, (c) $\pm$5h and (d) $\pm$6h. By abrading the sample to 1μA sandpaper, the clad layer is still distinguishable from the substrate material, without the use of an etchant. The horizontal lines are caused by the applied tape on the surface.

In Figure 4.12a it can be observed that corrosion initiates at the interface of the coating and clad layer, and propagates towards the substrate material. Arriving around the substrate material, corrosion propagates through the clad layer as observed in the phenomenon. However, instead of propagating further in this transition region, the clad layer dissolves until the coating is reached as shown in Figure 4.12b. Again, corrosion starts at the coating and clad interface before it propagates towards the substrate, suggesting that crevice corrosion plays a dominant role in initiating corrosion in the clad layer. Then, as shown in Figure 4.12c, first the clad layer dissolves in the coating material, and randomly corrosion initiates along the substrate surface without any noticeable initiation at the interface of the coating and the clad layer. The preferential dissolution of the clad layer corresponds to the increase of zinc found in this transition region, and to the potentiodynamic polarization curves showing that zinc will dissolve preferentially. Moreover, the corrosion degradation in Figure 4.12d is comparable to the degradation observed in the experiments of Figure 4.11. However, due to the typical dissolution of AA7072, a relief is formed on the substrate instead of the selective propagation observed in the phenomenon. The cause of these remaining clad areas is still unknown. These remaining areas are most likely the reason why corrosion does not propagate through the transition

area, but starts at the coating and clad interface towards the aluminium alloy substrate.

To observe whether AA7475C behaves differently from AA7075C and whether the TSA-layer affects the selective corrosion degradation, scribed AA7475CTSA samples were also monitored in-situ. This measurement is performed at longer experimental times over approximately 20 hours, with a lower galvanic current of 4μA, which was also induced by an external fastener. The degradation sequence and process was found similar to that of AA7075C, as shown in Figure 4.12. However, less relief was noticeable at the end of the measurement, meaning that the clad layer dissolves more gradually compared to AA7075C. In order to find the possible reason for this typical degradation and the preferential dissolution of certain areas, a SEM-EDS analysis was performed after the in-situ measurement of AA7075C, as shown in figure Figure 4.13. The EDS analysis was performed with an electron beam energy 20keV, a probe current of 63nA and a working distance at 10mm. The amount of detected elements are displayed in Table 4.7.

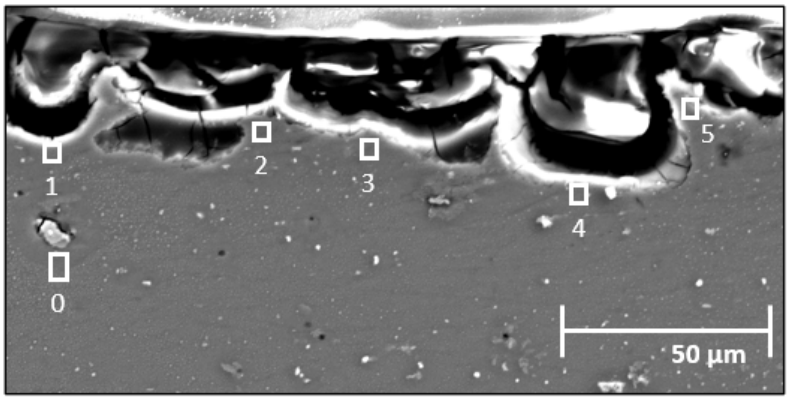

Figure 4.13: SEM-EDS measurement after the in-situ experiment of AA7075C.

Table 4.7: Mass% of elements detected by SEM-EDS per point in AA7075C.

	Al(K)	O(K)	Fe(K)	Cu(K)	Mg(K)	Zn(K)
Area 1	91.6	4.0	0.1	0.4	1.0	2.7
Area 2	71.8	25.5	0.8	0.0	0.0	2.0
Area 3	94.5	3.2	0.3	0.2	0.3	1.5
Area 4	70.1	21.7	0.3	0.3	0.9	3.0
Area 5	93.3	4.4	0.2	0.2	0.4	1.6
Area 0	89.3	2.0	0.1	1.1	2.3	5.2

Figure 4.13 shows four measured areas on AA7075C after the in-situ experiment. Area 0 is the AA7075B substrate material, with the measured elements in good agreement with the theoretical determined values. The element O is higher than the average value of the aluminium oxide layer on aluminium in all measurement. This can be explained by the fact that all areas are measured in the vicinity of a corroded surface or particle. Region 1 to 5 have been measured in the transition region of the clad layer, as indicated by the amount of zinc corresponding to the values previous found in this transition region. Interestingly, the amount of Cu, Fe or Mg measured in these areas is doubled or even four times as much as theoretically reported. It is not known whether Mg exists in this region as a single element or as a particle, such as a strengthening particle or intermetallic. Magnesium as a single elements, the strengthening particles ($MgZn_2$) and intermetallics (Mg_2Si) are

known to be anodic with respect to the aluminium matrix, thereby dissolving preferentially. However, also particles containing Mg were found to be cathodic with respect to the aluminium alloy [11]. Therefore, no unequivocal conclusion can be drawn about the influence of Mg in these regions. In contrast, the elements Cu and Fe are regardless of the appearance cathodic with respect to the aluminium alloy, which means that the surrounding matrix will dissolve preferentially [8; 11]. This enrichment of the diffused elements could be the possible reason for the selective preferential dissolution of AA7072, leaving Cu- and Fe-rich regions that create the relief on the substrate material. The dissolution mechanism of AA7075C is illustrated in Figure 4.14.

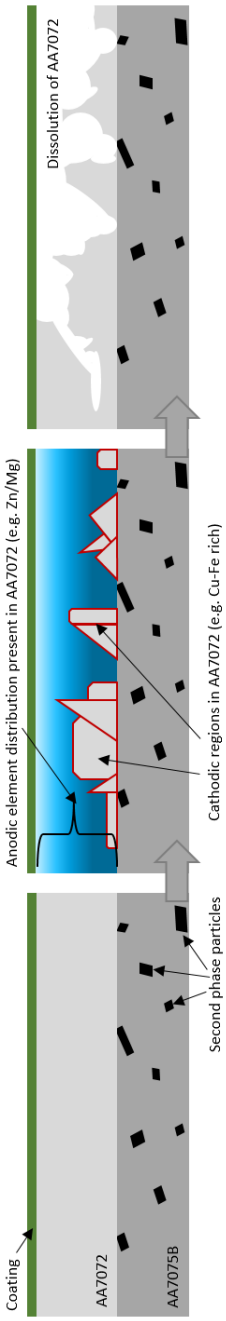

Figure 4.14: Preferential dissolution of AA7072 on AA7075C, leaving a Cu- and Fe- rich relief.

4.2.5 Discussion

This chapter evaluated the simulation of galvanic corrosion step by step, starting with the reproduction and measurement of a representative situation in the aerospace industry and concludes with the observation of a repeatable galvanic corrosion process in-situ. The behaviour of AA7X75C(TSA) alloys under galvanic corrosion condition became comprehensible within the used environmental conditions, and an experimental procedure was created to test galvanic corrosion accelerated under different condition with various alloys.

Although the exact degradation of the phenomenon has not been observed, the preferential dissolution of the clad layer appears to be in the transition region where the zinc content is higher than theoretically claimed. In this transition region, corrosion is observed that initiates through a small path from the interface of the coating and clad layer, or directly without any initiation path being visible. The latter corresponds to the propagation process observed in the phenomenon, where a constant dissolution of this transition region is observed. The Cu- and Fe-rich remnant regions, especially clearly visible in AA7075C, suggest that these elements create the preferential dissolution pathway. If such cathodic regions exist in the transition region, the most electrochemically favourable process would be to dissolve the clad layer toward the clad layer, before forcing propagation through these cathodic regions.

In AA7475CTSA a thicker clad layer is measured, compared to AA7075C and AA7475C. The dissolution of this clad layer appears to be more gradual, leaving less relief remnant. This can be explained by the fact that certain element probably diffused less far into the clad material of AA7475CTSA because of its thickness layer. Therefore, a reason for the occurrence of the phenomenon may be a purely alloy-specific phenomenon, meaning that it depends on the exact manufacturing process in which these cathodic regions are created in the clad layer by the diffusion of certain elements.

Furthermore, the difference in experiments can be the reason of the selective dissolution of the clad layer. In this chapter, fully immersed experiments are performed, essentially always creating electrolyte contact at all exposed interfaces. The NSS (ASTM B117) test is an experiment in which a continuous environment of dense saltwater fog is created. However, the exact onset of the electrolyte contact and the ingress of the electrolyte during corrosion propagation is not always continuous. This could be beneficial for the selective dissolution, as it may reduce continuous galvanic stimulation.

4.3 CORROSION INHIBITION

Developments towards a chromate-free corrosion protection system have been a crucial quest in the aerospace industry for decades. Multiple corrosion inhibiting strategies have been developed for chromate free active protective coatings, such as the traditional "leaching" process, galvanic inhibition and "smart" coating approaches with inhibition through self-healing properties and on-demand inhibitor release. Whereby, the traditional "leaching" mechanism is currently the foundation of aerospace specifications for active protective coatings in the aerospace industry.

There are many chromate-free inhibitors that exhibit activity, but do not perform when incorporated into a coating for various reasons, such as: solubility, efficacy, or compatibility with the binder system. Therefore the leaching capabilities should be considered from the coating/inhibitor perspective and have sufficient solubility and leaching characteristics, rapid and effective formation of an irreversible protective layer in the damaged area and maintain a good coating integrity. The inhibition efficiency and performance of this protective layer in a damaged area can be investigated by various well-known electrochemical techniques [6]. However, the protection stability of such formed layer in accelerated corrosion condition, for instance when it is galvanically stimulated, has not been well studied. Therefore, this chapter discusses the third main objective of this thesis:

- How can inhibition under galvanic corrosion conditions be reliably assessed?

This chapter is divided into two main sections. In the first section, a test procedure will be evaluated to study the performance of the protection layer that can potentially form in a damaged area when corrosion inhibitors are leached from the coating primer. After this process, an experiment is executed to investigate the stability of the protective layer when the specimen is galvanically stimulated. In this experiment, the reduced or inhibiting galvanic current is measured between the tested specimen and an external attached fastener. This is done with several accepted inorganic corrosion inhibitor primers in the aerospace industry, whereby two of the coatings contain the lithium based inhibitor technology.

The second section discusses how inhibition under galvanic corrosion conditions can be reliably assessed without the use of a coating. This test procedure can be used as a quick and first step in testing the galvanic current inhibition efficiency of various corrosion inhibitors. After the efficiency of the inhibitor is found to be sufficient, development can be conducted to implement the corrosion inhibitor in a coating system. This experiment is performed with usual suspects that have found to contain excellent inhibition efficiency on AA2024-T3 and AA7075-T6 [55]. Two of these these well-known "copper" inhibitors are being investigated under galvanic corrosion conditions, namely Benzotriazole and 2-mercaptobenzothiazole. The protective mechanism and reversible nature of these corrosion inhibitors is well discussed in a previous paper [44]. In addition, to find whether there is a preferentially inhibition performance on only the cathode or anode, both electrochemical cells are also separated by a salt-bridge as shown in Figure 3.14.

4.3.1 Corrosion inhibitor coatings

This chapter first examines the efficiency of various coatings with and without corrosion inhibitors in a defect area after being placed in an accelerated corrosion test. This is followed by the two main chapters as explained in the introduction. Finally, this chapter ends with a discussion.

Accelerated corrosion test

To asses the active protective properties, several coatings were artificially damaged and exposed to the NSS according to ASTM B-117 for 504 hours. Figure 4.15 shows the appearance of the scribed areas of the coatings that are applied to AA7075C, AA7475C and AA7475CTSA. Coating A and B are lithium-based coatings containing different lithium salts. Coating C does not contain lithium as corrosion inhibitor but various other inhibitor salts, and coating REF is a clearcoat used as a reference. All panels are tested in duplicate and also checked after 168h. Coating B is also applied with a thicker film (B2t) to AA7475CTSA, as shown in Table 3.3. The defect area is observed identical in degradation to coating B and is therefore not included in Figure 4.15.

Figure 4.15a shows all four coatings on AA7075C after 504 hours of NSS exposure. Coating REF shows the detrimental effect of the corrosive conditions when a coating does not contain any corrosion inhibitor. This degradation appears on AA7075C in a worm-like degradation structure that looks like filiform corrosion. Interestingly, this degradation propagates in the rolling direction of the aluminium alloy. Coating A has nearly clean scribes where a very low degree of darkening and white corrosion products are observed. In addition, only a few small blisters were found along the scribed defect. Coating B exhibits more corrosion in all aspects than Coating A, but Coating C shows clearly the most severe corrosion formation of the corrosion inhibitor coatings tested.

Furthermore, Figure 4.15b shows the defect areas on AA7475C after 504 hours of NSS exposure. In the REF coating again the most severe degradation occurs in the scribe and underneath the coating layer. In contrast to the clearcoat on AA7075C, the degradation is present on AA7475C in blister forms instead of a worm-like structure, which suggest a different corrosion mechanism. Coating A shows almost pristine scribed were no white corrosion product and blisters are seen, only a very lightly darkening can be detected in some spots in the scribe area. Coating B appears darker than Coating A in the scribe, but still no white corrosion products and blisters can be observed. However, in coating C, many small blisters appear along the defect area, leaving white corrosion products in the scribe area.

Lastly, all coatings were applied on AA7475CTSA, as shown in Figure 4.15c. The damaged area on coating REF shows the least corrosion products of all tested the alloys. The damaged area of Coating A appears as pristine as observed on AA7475C. Also, the defect of B and C is relative the same as on AA7475C, however Coating C shows no blisters forming along the damaged area. This can be explained by the thicker clad layer measured on AA7475CTSA compared to AA7475C, reducing the cathode-to-anode ratio of the clad layer and substrate material.

In general, the corrosion inhibition efficiency per aluminum alloy with the same coating: AA7475CTSA > AA7475C > AA7075C. The corrosion inhibitor efficiency per coating decreases from Coating A > Coating B > Coating C > Coating REF, where the lithium based coatings perform more efficiently compared to the coating without lithium as inhibitor.

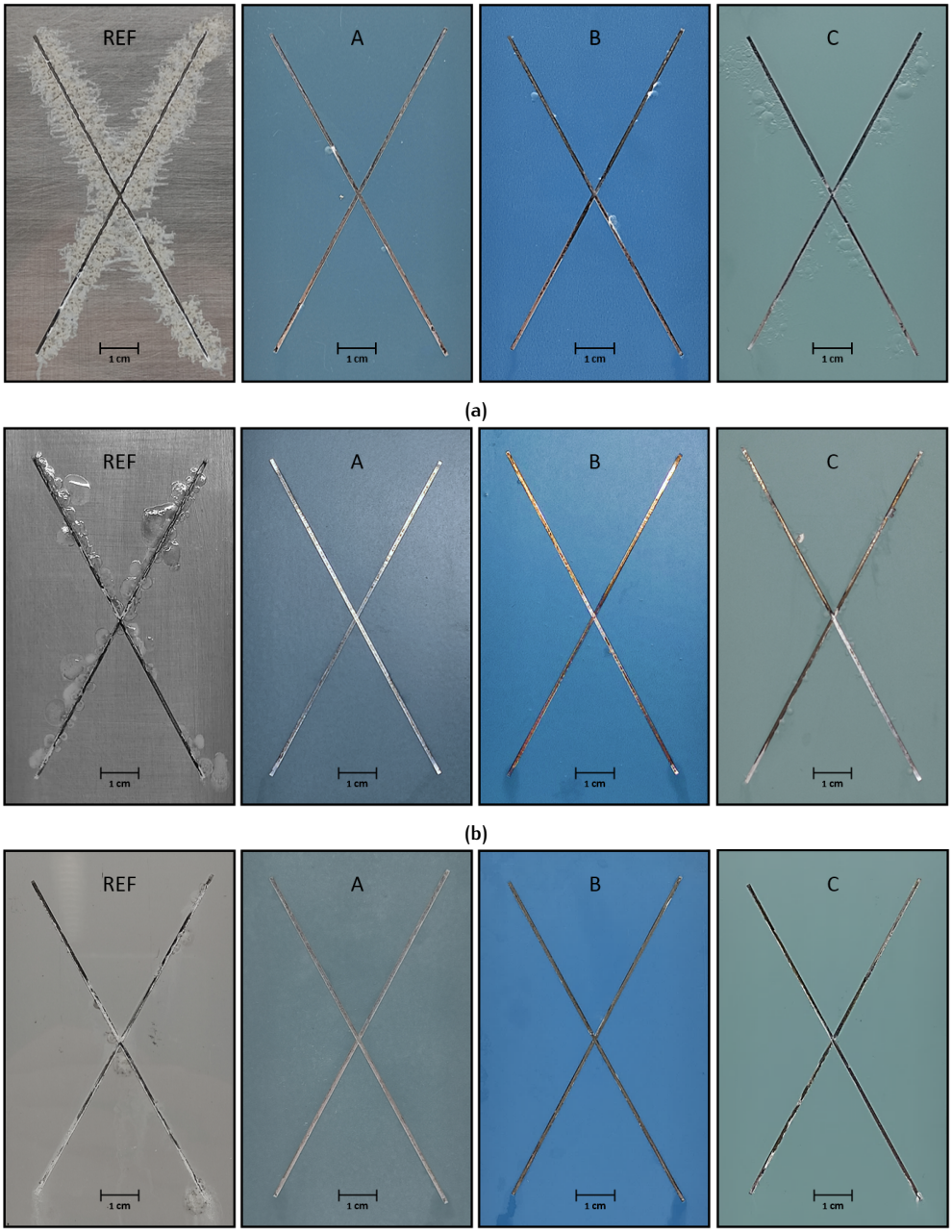

Figure 4.15: Scribed aluminium alloy panels: (a) AA7075C; (b) AA7475C; (c) AA7475CTSA after 504 hours of NSS with different coatings applied.

Determination of the active corrosion protection properties of the coatings

The measurement are performed in the procedure as explained in Figure 3.18. The panels coated with and without leachable corrosion inhibitors were exposed to the NSS according to ASTM-B117 for 168h to activate the corrosion inhibition. The cycle of the measurement started at a stable OCP and was performed 4 times per sample in 0.05M NaCl. The OCP measurement in the cycle is used for screening, and the LPR measurement are used to check whether the EIS values at low frequency (10^{-2}Hz) are in good agreement. EIS can be used to evaluate the corrosion protective properties in the defect area as result of active protective activity of the coating [50]. Every fourth cycle of EIS measurement per sample that was in good agreement with the OCP and LPR is shown in an average in Figure 4.16, with the impedance modulus plots of AA7075C and AA7475C in Figure 4.16a and Figure 4.16b, respectively. The phase angle plot of AA7075C and AA7475C are displayed in Figure 4.16c and Figure 4.16d, respectively. After the EIS measurement, the samples were visually assessed and were all in good agreement with the measured results.

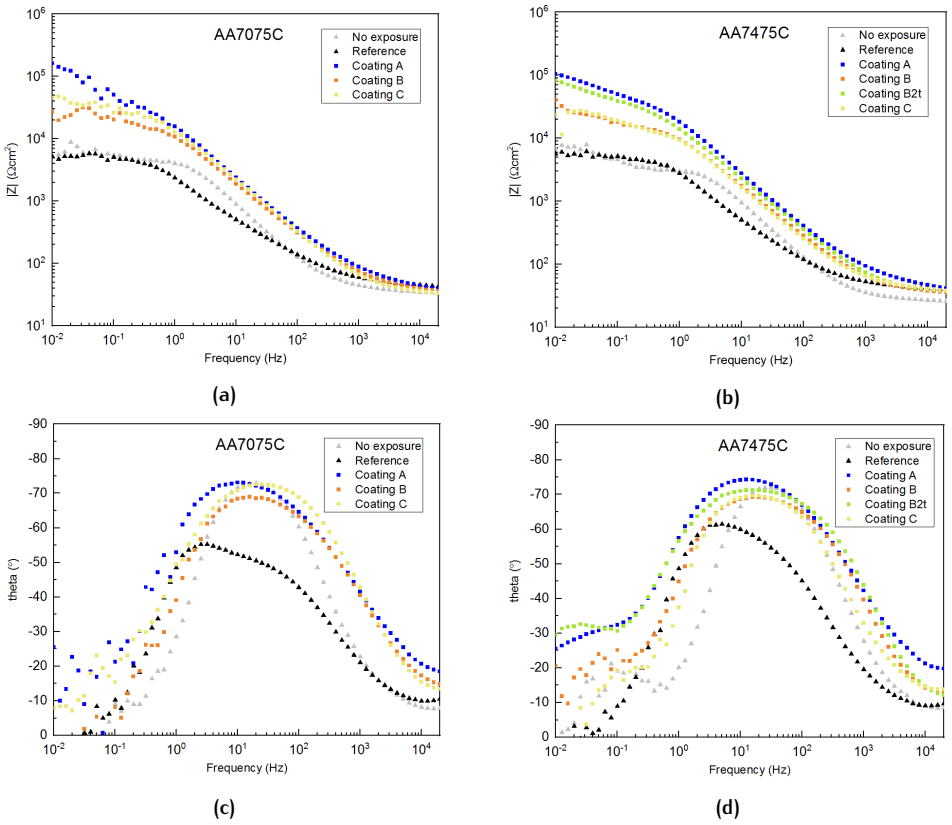

Figure 4.16: Electrochemical impedance spectra of the defect areas of coatings loaded with and without leaching inhibitors measured in 0.05M NaCl: (a) and (b) impedance modulus plots, (c) and (d) phase angle plots.

The "Reference" coating is exposed to the NSS for 168h and the "No exposure" coating is measured unexposed. The Bode plots for both alloys reveal that the impedance of all coatings loaded with corrosion inhibitors show an increase in impedance value in the middle (10^{1}-10^{3}) and low (10^{-1}-10^{-2}) frequency ranges compared to the coatings without corrosion inhibitors. The lower frequency range is related to the corrosion processes of a defect area, and the middle frequencies can be associated with a protective (oxide) layer in the damaged area [50]. This means that all coatings loaded with a corrosion inhibitor achieved active protection in the defect area after the measurement. This way, also the average performance of the different inhibitor coatings can be mutually compared. The inhibition performance

on AA7075C with the highest impedance in these time-constants is: Coating A > Coating C > Coating B, and on AA7475C: Coating A > Coating B2t > Coating B > Coating C.

The accompanying Bode phase angle plots are shown in Figure 4.16c and Figure 4.16d. In the lower frequency range, especially on AA7075C, a lot of electrochemical activity is observed at the defect area, which makes the several measured coatings hard to distinguish. The middle frequencies is associated with the protective (oxide) layer in the defect area. The peak of the phase angle reached in this time-constant demonstrates the impedance of the protective layer. Moreover, the broadening of this peak, or in other words the frequency range in which the highest phase angle remains, together with the increase in impedance modulus expresses the formation of an improving protective layer in the defect region. Important to notice is that all coatings loaded with corrosion inhibitors contain a higher or broader peak in the middle frequency range than the reference coating and measured samples without exposure. This means that all coatings loaded with corrosion inhibitors show the formation of a protective layer and thus corrosion inhibition.

After the formation of a protective layer was measured, the resistance to a galvanically induced current was measured by a ZRA experiment. The aluminium alloy AA7475C shows less activity in the low frequency range in the EIS measurements and in general a more solidly performance than on AA7075 which is also reflected in the NSS tests, therefore the ZRA experiments were performed on AA7475C. Figure 4.17 shows the results of various tests in different solutions and exposed cathodic areas. Note that all lines are single measurements in various solutions, while for the EIS results averages of 3 to 4 samples per coating are taken in the same 3.5%NaCl solution. Moreover, in an EIS measurement, the weakest (corrosion) spot is measured in the defect area, which does not mean that the entire defect area is corroded. Hence, the relative arrangement between the different inhibitor coatings may be different in this experiment.

The essence of this experiment is whether the protective layer in the defect can resist the galvanic polarization generated by the cathodic fastener. In this way, the resistance of a protection layer formed can be assessed when a galvanically current is induced by an external cathode. Figure 4.17a shows all various coatings on AA7475C measured in 3.5%NaCl solution. It can be observed that the reference coatings as well as the coatings loaded with corrosion inhibitors exhibit an almost similar galvanic current within 900 seconds. The reason for this can be that the galvanic pressure which breaks the protective layer is too severe or that the solution is too aggressive for the protective layer formed. Therefore, the same experiment was performed in a less aggressive solution of 0.05M NaCl, as shown in Figure 4.17b. These results show no difference in current with the experiments performed in 3.5% NaCl solution. The only notable observation that can be seen is that Coating A shows an increase in current from the start of the measurements in both measurements. Although this is only observed for a short period of time, it suggests some galvanic corrosion resistance of Coating A. The third experiment is shown in Figure 4.17c and is performed after the samples are placed in a 0.05M NaCl solution overnight. This was done to find out whether the resistance would increase if the measurement were started in equilibrium. However, this has no significant effect on the galvanic corrosion inhibition efficiency. The last experiment was performed with 1/10 of the exposed cathodic surface in 0.05M solution. It can be seen that a clearer distinction can be made between the different measurements, meaning that reducing the cathodic surface gives more control over the measurement. In addition, all coatings loaded with corrosion inhibitors exhibit a lower current than the reference coating for at least 2 hours, and that the measured current starts at a lower value. Although a decrease in the measured galvanic current when 1/10 of the cathodic area is exposed can be observed in the coatings loaded with corrosion

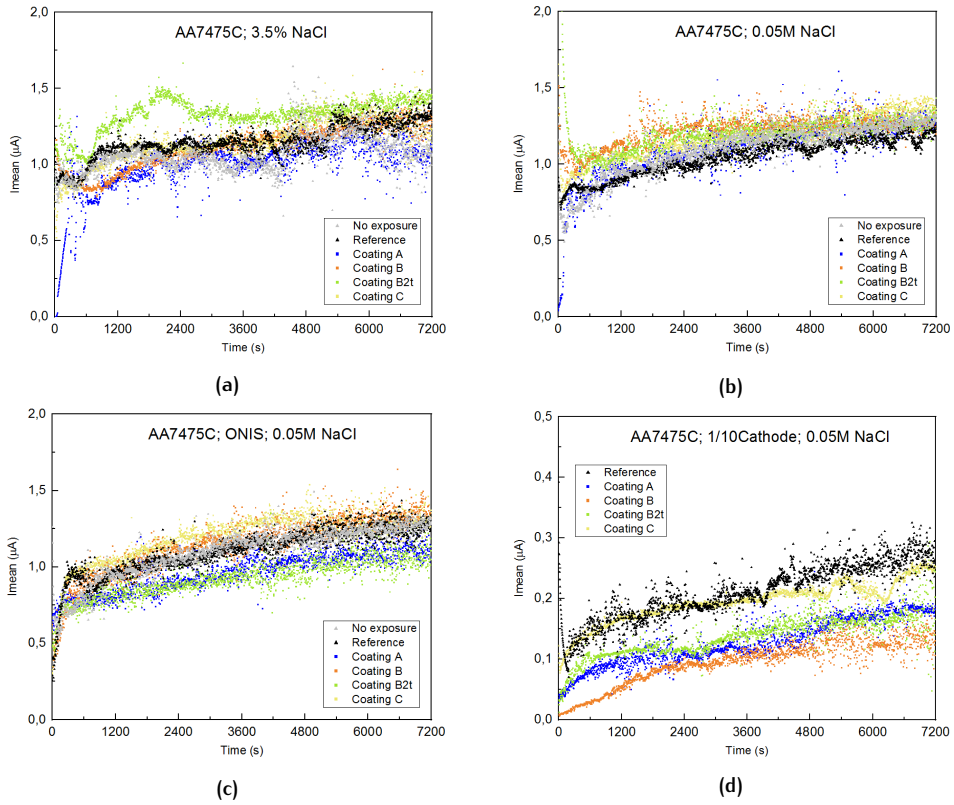

Figure 4.17: ZRA measurements of the protective scribed areas on AA7475C for 2h: (a) in 3.5% NaCl, (b) in 0.05M NaCl, (c) in 0.05M NaCl after begin placed overnight into the solution (ONIS), (d) in 0.05M NaCl with 1/10 of the cathodic exposed area.

inhibitors relative to the reference coating, the galvanic current is not completely inhibited. However, this shows clearly that the size of the exposed area of the cathode matters significantly.

4.3.2 Corrosion inhibition without the use of coatings

The test procedure discussed in this section can be used as a first step in testing the galvanic inhibition efficiency of various corrosion inhibitor solutions. After the efficiency of the inhibitor is found to be sufficient, further development can be performed to implement the corrosion inhibitor in a coating system. In addition, it is discussed how the preferred inhibition of the corrosion inhibitor solution can be tested by separating the cathode and anode using a salt bridge. This allows a clear decision to be made whether a certain corrosion inhibitor that inhibits specific elements is suitable on a material that mainly consists of other alloying elements.

Corrosion protection of aluminium alloys under galvanic corrosion conditions

The inhibition performance of several solution containing corrosion inhibitors were tested by ZRA measurements. Inhibitor solution were made with two usual suspects, namely BTA and 2-MBT, as their inhibitor efficiencies have been shown to be higher than 90% on AA7075-T6 [6]. The concentration of 5mM is the minimum concentration needed to obtain reproducible corrosion inhibition with BTA, and due to the low solubility of 2-MBT in water this concentration is limited to 1mM [44]. Before the measurements started, the electrode to be measured was placed in the solution for 30 minutes. Figure 4.18 shows the performance of the inhibitor solutions tested for 16 hours, whereby the cathode and AA7475C anode is placed together with the solution in one electrochemical cell. The percentages mentioned in this chapter are calculated from averages of the mentioned time intervals of the curves.

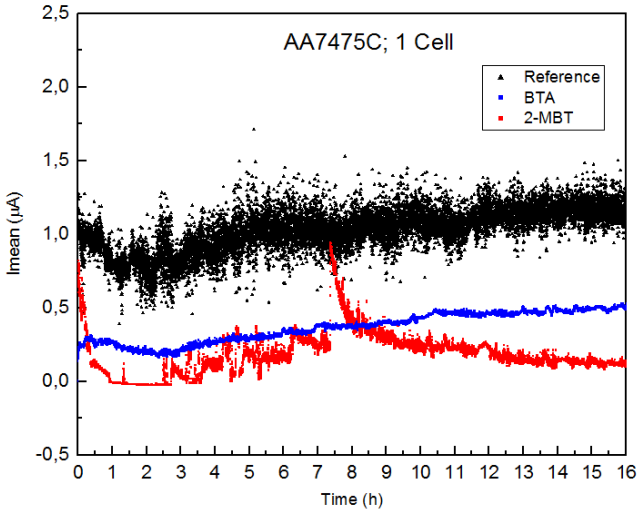

Figure 4.18: The inhibitor solutions tested with the cathode and anode in one electrochemical cell.

The reference measurement (REF) is performed in a 3.5% NaCl solution without the addition of a corrosion inhibitor and corresponds to the coupled current range in the potentiodynamic measurements in Figure 4.8. The measurement performed in BTA solution reduced the galvanic current between the cathode and the anode from approximately 1μA to 0.3μA. The average drop in the percentage of 2-MBT is not representative to measure due to the peak value, but it can be noted that the galvanic inhibitor performance is even better than that of the BTA solution. At approximately 1-2.5 hours, even a negative current is measured, meaning the galvanic current is reversed and corrosion occurs on the cathodically exposed area. This probably explains the peak in current that is observable and can be clarify by the fact that after corrosion on the cathode more cathodic elements remain on the surface (e.g. Cu) producing an increased cathodic current. After a certain period of time, the inhibitor performance of the 2-MBT solution recovered, with the current

on the time interval of 12-16 hours even being reduced by 88% with respect to the reference measurement on this time interval. In addition, no corrosion was visually observed on neither the cathode nor the anode after the 16 hour measurement when corrosion inhibitor solutions were used. In contrast, the reference measurement on both electrodes showed visually corrosion products, which also may explains the difference in noise between the reference measurement and the solutions containing corrosion inhibitors.

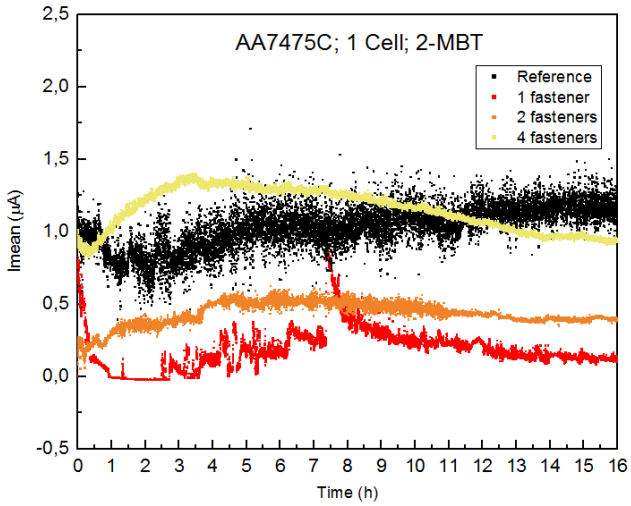

Figure 4.19: The effect of increased cathode area tested with the cathode and anode together with 1mM 2-MBT solution in one electrochemical cell.

The effect of increasing the cathodic exposed surface on the inhibition performance is tested in one electrochemical cell, as shown in Figure 4.19. The 2-MBT corrosion inhibitor solution was tested because it previously showed the best inhibition performance among the tested solutions. By doubling the exposed cathodic area, the measured current is still reduced by approximately 66% on the time interval of 12-16 hours relative to reference measurement. Doubling the exposed cathodic area again increased the current for approximately 75% of the measuring time above the reference measurement. However, at the time interval between 12-16 hours, it dropped to an average current that is 16% lower with respect to the reference. This clearly demonstrates the galvanic current inhibition efficiency of 2-MBT when larger areas are exposed during the corrosion process while the damaged area is kept constant.

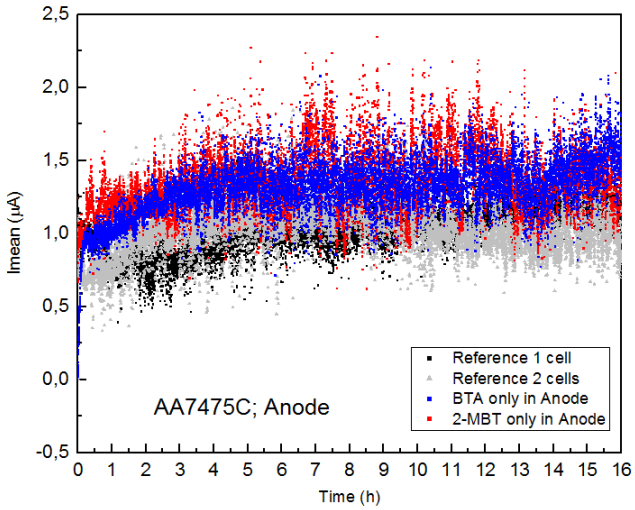

Figure 4.20: The efficiency of the inhibitor solution is tested when only the anode is placed into the solution.

After the measurements were performed in one cell, the cathode and anode are placed in separate cells and connected with a salt-bridge. This allowed to conduct the same ZRA measurement when only the cathode or anode was placed in an inhibitor solution. The first experiment whereby only the anode was placed into the inhibitor solution is shown in Figure 4.20. It can be observed that the reference measurement in one cell and the reference in two cells without the use of an inhibitor solution are in excellent agreement, meaning that the salt-bridge does not have a significant effect on the measurement. Adding the inhibitor solutions only to the anode does not have any effect on the reduction of the galvanic current. In fact, the average current is even increased with approximately 27% for both solutions loaded with corrosion inhibitors with respect to the reference measurement. After the measurement the samples were visually inspected. The fasteners surface had a goldish shine, which suggest an increase of copper on the exposed surface due to self-corrosion. This may explain the increase in current flow that is measured when only the anode is placed in the inhibitor solution.

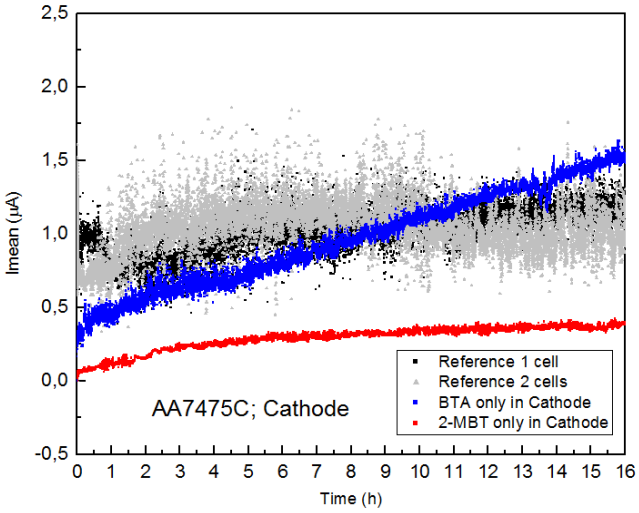

Figure 4.21: The efficiency of the inhibitor solution is tested when only the cathode is placed into the solution.

The addition of the inhibitor solution only to the cathode is shown in Figure 4.21. Relative to the reference measurement, the solution containing BTA was not able to reduce the galvanic corrosion current for the measured time. This shows that BTA only is able the suppress the galvanic corrosion current when it is placed in contact with both the cathode and anode. The solution containing 2-MBT clearly inhibits the galvanic current when only the solution is placed in the electrochemical cell of the cathode. Relative to the reference measurement the galvanic current is reduced with 75%. These finding suggest that 2-MBT is a stronger copper inhibitor, while BTA acts more as a mixed inhibitor on AA7475C. In addition, less noise is observed when the cathode is placed in both solution, whereas much noise is measured when only the anode is inhibited. This suggest that the noise measured can mainly be attributed to the activity on the cathodic surface.

4.3.3 Discussion

The NSS test were used to examine the efficiency of various coatings with and without corrosion inhibitors in a defect area. The corrosion degradation observed on AA7075C after the NSS test shows a worm-like structure on the clearcoat panel. Observing the corrosion degradation on AA7475C and AA7475CTSA after the NSS test shows the formation of blisters when a clearcoat is applied. The cathode-to-anode ratio between AA7075C and AA7475C is similar because approximately the same clad thickness was measured. Since these two mechanisms were also observed when AA7075C and AA7475C(TSA) were galvanostatically degraded, it suggests that the phenomenon in Figure 1.1 is an alloy-specific occurrence. When coatings loaded with corrosion inhibitors are tested, blistering is only observed along the defective area in several cases. This shows that when the corrosion process is inhibited, the corrosion mechanism is also able to change. To explain this transformation, further research is needed.

The EIS data in Figure 4.16 shows that Coating C has on average a higher impedance than Coating B on AA7075C. The impedance of both coatings on AA7475C is relatively close to each other, with Coating B performing slightly better on average than Coating C. Given the NSS results, it shows that less degradation is detected on Coating B than on Coating C on all tested panels. When evaluating all individual LPR results, as shown in Appendix D, it becomes clear that inhibition can be achieved with both coatings, but that this is certainly not always the case. This means that both coatings score well on average compared to the reference, but that an uncertainty is present in the minimum protective properties that can be formed by these coatings in the defect area. Visually this was also observed after the EIS measurements. The inhibitor efficiency of Coating A is the highest of all coatings loaded with corrosion inhibitors tested. The EIS results of Coating A on AA7475C show a significant reduction in the activity compared to Coating A on AA7075C, supporting the less degradation observed in the defect area after the NSS test. Also, less activity is found in individual measurements when the coating thickness was increased, as shown with Coating B2t.

The ZRA experiments on the samples tested with and without coatings showed an almost similar galvanic current in all measurements when only the anode was protected. The measurements became distinguishable and more stable when the exposed cathodic area was reduced or inhibited. This is consistent with the findings in Table 4.6, where increasing the cathodic area also increased the noise of the measurement. This suggests that a lot of activity is present on the cathode surface when no inhibitor is used, meaning that many galvanic cells are likely formed due to the relatively high amount of copper on the AA2017A surface. Because when "copper" inhibitors are used, less noise and a reduction in the galvanic current is measured. In addition, when the inhibitor solutions were tested, the use of separated cells showed the inhibition preference of the tested corrosion inhibitors. In general, it can be concluded that the solution containing 2-MBT performed excellently among the tested solution in reducing the galvanic corrosion current, with less inhibitor used and even when the exposed cathodic area was quadrupled. As a result, an experimental procedure has been created in which corrosion inhibitor solutions can be compared relative to each other. It is important to note in what sense the reduction of galvanic current can be linked to the amount of corrosion degradation in the defective area, or in other words to the exact protective effect of the different inhibitors. For example, the overall inhibitor performance of the defective area may be achieved, but still a relatively high galvanic current may be measured that passes through small defects. Or that the galvanic current is reduced when the corrosion inhibitor solution is added only to the cathode, while the defec-

tive area still corrodes because of the potential difference present in the scribed area. Therefore, a further experiment is proposed in the recommendation section.

5 CONCLUSIONS AND RECOMMENDATIONS

The aim of this work is to gain understanding into the corrosion behaviour of 7XXXClad series aluminium alloys under galvanic corrosion conditions. This is performed as a result of the selective dissolution of the clad layer in AA7475CTSA after a NSS test under accelerated galvanic corrosion conditions. The results and discussion led to mainly the following conclusions per research objective:

- What is the role of zinc in the Clad layer respect to corrosion initiation and propagation?
  Zinc in the clad layer decreases the equilibrium potential and increases the corrosion rate of the clad layer on AA7X75C. A potential difference between pure aluminium and zinc of about 250mV and a current density approximately 80 times higher for zinc was observed. These findings conclude that zinc preferentially dissolves when both elements are in electrical contact in the presence of the electrolyte used. In the clad layer of AA7075C and AA7475C, a distribution of alloying elements from the substrate to the clad surface was measured. Thereby, an increased amount of zinc was found in the region along the substrate and clad layer interface than the theoretical maximum reported. This means that a transition region is present in the clad layer that may be held responsible for the selective dissolution observed.

- How do 7XXXClad alloys behave under galvanic corrosion conditions?
  Potentiodynamic polarization curves have shown that the coupled parameters in a galvanic system can be estimated by Tafel extrapolation of the intersections of the cathodic and anodic curves. The coupled parameters (i.e. mixed potential and coupled current) can be measured using an electrochemical noise measurement in zero resistance ammeter mode. These measured parameters can be applied to simulate the galvanic corrosion degradation in a galvanic system. When galvanostatic polarization is used for this simulation, the degradation of the clad layer appears to be of the same type regardless of the time and amount of induced current. The characteristic relief formed during degradation of the clad layer of AA7075C can be attributed to the increase of cathodic elements found in these remnants regions. Only observing the corrosion degradation of the clad layer after the galvanic experiments does not reveal the exact sequence of dissolution, with much information about the process being lost. To demonstrate this, in-situ experiments can be performed. While simulation of the phenomenon has been partially shown with in-situ experiments, it is not fully observed. Overall, these experiments demonstrate a clear procedure for measuring, simulating and observing the galvanic corrosion degradation in 7XXXC aluminium alloys, and provide a solid foundation for testing different fastener in various sizes.

- How can inhibition under galvanic corrosion conditions be assessed reliably?
  Inhibition of corrosion is studied with and without the use of coatings. A Neutral Salt Spray test (ASTM B-117) was performed to compare the inhibition performance of the various coatings used. The corrosion inhibitor efficiency per coating was measured to decrease from: Coating A $>$ Coating B $>$ Coating C $>$ Coating REF. The corrosion inhibition efficiency per aluminum alloy with the same applied coatings is: AA7475CTSA $>$ AA7475C $>$ AA7075C. In order to measure the galvanic corrosion protection in an artificially created

defect area, an OCP, LPR and EIS measurement over time can be performed. A Neutral Salt Spray can be used to activate the coatings loaded with corrosion inhibitors, because subsequently LPR and EIS experiments demonstrated that inhibition was achieved for all coatings loaded with corrosion inhibitors with respect to a reference measurements. Finally, an electrochemical noise measurement in zero resistance ammeter mode can be performed to measure the resistance of the protective layer formed when a galvanic current was induced with an external cathode. Hereby, a reduction in galvanic current is observed, whereby reducing the cathodic exposed area affects the measurement significantly.

Corrosion inhibitor solutions can be quickly assessed using an electrochemical noise measurement in zero resistance ammeter mode. Moreover, by using a salt-bridge, the inhibition preference of an inhibitor solution can be found specifically at the anode or cathode in a galvanic system. The results showed that BTA could only reduce the galvanic current if both the anode and cathode were inhibited. The solution containing 2-MBT performed excellently in reducing the galvanic corrosion current also in the cathode alone, with less inhibitor dissolved into the solution and even when the exposed cathodic area was quadrupled. Both showed no inhibition in galvanic current when the anode was protected alone. Therefore, generally it can be concluded that limiting the cathodic reactions is of paramount importance to reduce the galvanic corrosion current.

Recommendations

The findings in this thesis warrant the following recommendations for further research:

- Many experiments showed that a possible explanation for the selective dissolution of the phenomenon may be that it is an alloy-specific observation. Simulation of the phenomenon in a 3000 hours NSS test on AA7475CTSA with a chromium (VI) loaded inhibitor coating has not been tested due to the time frame of this thesis and strict limitations when working with chromium (VI). By simulating the galvanic effect with different techniques, the in-situ showed partially the selective dissolution, but the phenomenon was still not fully observed. Moreover, when studying the SEM-EDS line scan results, a different amount of diffuse alloy elements was measured on both AA7072 clad layers, which means that there are large local differences in AA7072. Therefore, to find out whether the phenomenon is alloy specific, simulation of the 3000 hours NSS test would be proposed with different AA7475CTSA alloys obtained from different manufacturers.

- By observing the dissolution of the clad layer in-situ, a lot of information is obtained about the exact degradation process that usually is lost. In this thesis, a fastener was electrically coupled to the substrate materials whereby only the corrosion process was monitored in detail. By adding a potentiostat, measurements can be conducted while monitoring the degradation process. This substantiates the optical observations with measured variation in the galvanic parameters. For example, the amount of Coulombs can be measured needed to dissolve a certain area of the clad layer material, or to observe the potential fluctuations in a galvanostatic experiment that are necessary to keep the current constant for the corrosion initiation or propagation in the clad layer material. In addition, when corrosion inhibitors are tested, the degradation of the anodic scribed material can be observed. The results showed that when only the anode was inhibited, the galvanic currents were comparable to those measured during the reference test. However, this tells not much about the

amount of corrosion degradation caused by this galvanic current on the anodic material, because the inhibitor solution that was added to the anode can still affect the amount of corrosion degradation. By monitoring this in-situ while performing a ZRA measurement, a conclusion may be drawn about the relation between the amount of degradation and the reduction of galvanic current.

- Small material losses after galvanic corrosion degradation can also be measured using an optical profilometer. After the experiments, the coating and corrosion products can be removed by, for example, placing the specimens in a concentrated solution [73]. Then, the weight change can be monitored after a certain time of immersion. When the weight loss between consecutive measurements for instance is less than 0.01g, topographic analysis of the scribed areas on the stripped panels can be performed using an optical profilometer. With these topographic images, the volume loss of the scribed panels can be determined. After subtracting the volume of the pristine scribe, the corroded volume is measured. This makes it possible to relate the volume loss of the material to the total charge measured during galvanic corrosion measurements.

- Many more inhibitor solution have been investigated on the inhibitor performance on AA7075 as discussed in Chapter 2. In this thesis only two well-known "copper" inhibitor solutions have been tested to demonstrate how inhibition of a galvanic current can be measured. The results showed that when both the cathode and anode were inhibited, the best performance in reducing the galvanic current was found. The second highest reduction was measured when only the cathode was inhibited, which could be because of the element of copper is present about twice as often in AA2017 as in AA7475. It would be interesting to investigate corrosion inhibitor solutions that appear to perform better on AA7075 than on AA2024 [55]. This may be due to the higher zinc content in AA7075 and also to the fact that individual phases (particularly $MgZn_2$) contain high concentrations of zinc. This increased inhibition efficiency was found when an amino-group was added in a inhibitor structure [55]. The substrate and clad materials used in this work have zinc as the main alloying element. Therefore, the effect of amino function on the galvanic current inhibition performance is worth further investigating.

BIBLIOGRAPHY

1. A. P. Mouritz, *Introduction to aerospace materials*. Elsevier, 2012.
2. K. Anderson, J. Weritz, and J. G. Kaufman, "7075 and alclad 7075," *JIS*, vol. 4186, p. 4187, 2019.
3. A. International, "Heat treating of aluminum alloys," *ASM Handbook, Volume 4: Heat Treating*, pp. 841–879, 1991.
4. F. Andreatta, *Local electrochemical behaviour of 7xxx aluminium alloys*. Pasmans, 2004.
5. G. E. Totten and D. S. MacKenzie, *Handbook of aluminum: vol. 1: physical metallurgy and processes*. CRC press, 2003.
6. A. E. Hughes, J. M. Mol, M. L. Zheludkevich, and R. G. Buchheit, "Active protective coatings," *Active Protective Coatings: New-Generation Coatings for Metals, Springer Series in Materials Science, Volume 233. ISBN 978-94-017-7538-0. Springer Science+ Business Media Dordrecht, 2016*, 2016.
7. C. Jawalkar, S. Kant, *et al.*, "A review on use of aluminium alloys in aircraft components," *i-Manager's Journal on Material Science*, vol. 3, no. 3, p. 33, 2015.
8. F. Andreatta, H. Terryn, and J. De Wit, "Effect of solution heat treatment on galvanic coupling between intermetallics and matrix in aa7075-t6," *Corrosion Science*, vol. 45, no. 8, pp. 1733–1746, 2003.
9. R. Ayer, J. Koo, J. Steeds, and B. Park, "Microanalytical study of the heterogeneous phases in commercial al-zn-mg-cu alloys," *Metallurgical Transactions A*, vol. 16, no. 11, pp. 1925–1936, 1985.
10. M. Gao, C. Feng, and R. P. Wei, "An analytical electron microscopy study of constituent particles in commercial 7075-t6 and 2024-t3 alloys," *Metallurgical and Materials Transactions A*, vol. 29, no. 4, pp. 1145–1151, 1998.
11. N. Birbilis and R. G. Buchheit, "Electrochemical characteristics of intermetallic phases in aluminum alloys: an experimental survey and discussion," *Journal of the Electrochemical Society*, vol. 152, no. 4, p. B140, 2005.
12. M. K. Cavanaugh, R. G. Buchheit, and N. Birbilis, "Evaluation of a simple microstructural-electrochemical model for corrosion damage accumulation in microstructurally complex aluminum alloys," *Engineering Fracture Mechanics*, vol. 76, no. 5, pp. 641–650, 2009.
13. F. Andreatta, M. Lohrengel, H. Terryn, and J. De Wit, "Electrochemical characterisation of aluminium aa7075-t6 and solution heat treated aa7075 using a microcapillary cell," *Electrochimica Acta*, vol. 48, no. 20-22, pp. 3239–3247, 2003.
14. C. Bartges, "Changes in solid solution composition as a function of artificial ageing time for aluminium alloy 7075," *Journal of materials science letters*, vol. 13, no. 11, pp. 776–778, 1994.
15. J. K. Park and A. Ardell, "Microstructures of the commercial 7075 al alloy in the t651 and t7 tempers," *Metallurgical Transactions A*, vol. 14, no. 10, pp. 1957–1965, 1983.
16. F. Viana, A. Pinto, H. Santos, and A. Lopes, "Retrogression and re-ageing of 7075 aluminium alloy: microstructural characterization," *Journal of Materials Processing Technology*, vol. 92, pp. 54–59, 1999.

17. V. Hansen, O. Karlsen, Y. Langsrud, and J. Gjønnes, "Precipitates, zones and transitions during aging of al-zn-mg-zr 7000 series alloy," *Materials science and technology*, vol. 20, no. 2, pp. 185–193, 2004.

18. F. Andreatta, H. Terryn, and J. De Wit, "Corrosion behaviour of different tempers of aa7075 aluminium alloy," *Electrochimica acta*, vol. 49, no. 17-18, pp. 2851–2862, 2004.

19. E. A. Starke Jr and J. T. Staley, "Application of modern aluminum alloys to aircraft," *Progress in aerospace sciences*, vol. 32, no. 2-3, pp. 131–172, 1996.

20. A. S. El-Amoush, "Intergranular corrosion behavior of the 7075-t6 aluminum alloy under different annealing conditions," *Materials Chemistry and Physics*, vol. 126, no. 3, pp. 607–613, 2011.

21. R. P. Wei, C.-M. Liao, and M. Gao, "A transmission electron microscopy study of constituent-particle-induced corrosion in 7075-t6 and 2024-t3 aluminum alloys," *Metallurgical and Materials Transactions A*, vol. 29, no. 4, pp. 1153–1160, 1998.

22. C.-M. Liao and R. P. Wei, "Galvanic coupling of model alloys to aluminum—a foundation for understanding particle-induced pitting in aluminum alloys," *Electrochimica Acta*, vol. 45, no. 6, pp. 881–888, 1999.

23. S. Yan, G.-L. Song, Z. Li, H. Wang, D. Zheng, F. Cao, M. Horynova, M. S. Dargusch, and L. Zhou, "A state-of-the-art review on passivation and biofouling of ti and its alloys in marine environments," *Journal of materials science & technology*, vol. 34, no. 3, pp. 421–435, 2018.

24. N. Birbilis and R. Buchheit, "Investigation and discussion of characteristics for intermetallic phases common to aluminum alloys as a function of solution ph," *Journal of the Electrochemical Society*, vol. 155, no. 3, p. C117, 2008.

25. N. Birbilis and B. Hinton, "Corrosion and corrosion protection of aluminium," *Fundamentals of Aluminium Metallurgy*, pp. 574–604, 2011.

26. T. I. Wu and J. K. Wu, "Effect of surface finish on the corrosion behavior of commercial 7075 al alloy," *Scripta metallurgica et materialia*, vol. 27, no. 7, pp. 875–880, 1992.

27. G. D. Palkar Aman Manohar, N. K. Sinha, and R. K. Mishra, "Effect of annealing process on the corrosion resistance of aluminium 7075-t6 alloy," *International Research Journal of Engineering and Technology (IRJET) Vol*, vol. 4, pp. 1013–1019, 2017.

28. S. Maitra and G. English, "Mechanism of localized corrosion of 7075 alloy plate," *Metallurgical Transactions A*, vol. 12, no. 3, pp. 535–541, 1981.

29. W. Zhang and G. Frankel, "Transitions between pitting and intergranular corrosion in aa2024," *Electrochimica Acta*, vol. 48, no. 9, pp. 1193–1210, 2003.

30. E. Codaro, R. Nakazato, A. Horovistiz, L. Ribeiro, R. Ribeiro, and L. d. O. Hein, "An image processing method for morphology characterization and pitting corrosion evaluation," *Materials Science and Engineering: A*, vol. 334, no. 1-2, pp. 298–306, 2002.

31. P. Pao, C. Feng, and S. Gill, "Corrosion fatigue crack initiation in aluminum alloys 7075 and 7050," *Corrosion*, vol. 56, no. 10, pp. 1022–1031, 2000.

32. R. A. M. Anaee and M. H. Abdulmajeed, "Tribocorrosion," *Advances in Tribology*, 2016.

33. F. Andreatta, H. Terryn, M. Lohrengel, and J. De Wit, *Use of scanning Kelvin probe force microscopy and microcapillary cell to investigate local corrosion behaviour of 7xxx aluminium alloys*. Woodhead Publishing, Ltd. Cambridge, UK, 2006.

34. M. K. Cavanaugh, J.-C. Li, N. Birbilis, and R. G. Buchheit, "Electrochemical characterization of intermetallic phases common to aluminum alloys as a function of solution temperature," *Journal of The Electrochemical Society*, vol. 161, no. 12, p. C535, 2014.

35. T. Ramgopal, P. Schmutz, and G. Frankel, "Electrochemical behavior of thin film analogs of mg (zn, cu, al) 2," *Journal of the Electrochemical Society*, vol. 148, no. 9, p. B348, 2001.

36. M. Fourmeau, C. D. Marioara, T. Børvik, A. Benallal, and O. S. Hopperstad, "A study of the influence of precipitate-free zones on the strain localization and failure of the aluminium alloy aa7075-t651," *Philosophical Magazine*, vol. 95, no. 28-30, pp. 3278–3304, 2015.

37. J. K. Park and A. Ardell, "Effect of retrogression and reaging treatments on the microstructure of ai-7075-t651," *Metallurgical and Materials Transactions A*, vol. 15, no. 8, pp. 1531–1543, 1984.

38. J. Park and A. Ardell, "Microchemical analysis of precipitate free zones in 7075-a1 in the t6, t7 and rra tempers," *Acta metallurgica et materialia*, vol. 39, no. 4, pp. 591–598, 1991.

39. D. McNaughtan, M. Worsfold, and M. Robinson, "Corrosion product force measurements in the study of exfoliation and stress corrosion cracking in high strength aluminium alloys," *Corrosion Science*, vol. 45, no. 10, pp. 2377–2389, 2003.

40. J. R. Davis, *Corrosion of aluminum and aluminum alloys*. Asm International, 1999.

41. J. Mol, A. Hughes, B. Hinton, and S. Van Der Zwaag, "A morphological study of filiform corrosive attack on chromated and alkaline-cleaned aa2024-t351 aluminium alloy," *Corrosion science*, vol. 46, no. 5, pp. 1201–1224, 2004.

42. J. Mol, B. Hinton, D. Van Der Weijde, J. De Wit, and S. Van Der Zwaag, "A filiform corrosion and potentiodynamic polarisation study of some aluminium alloys," *Journal of materials science*, vol. 35, no. 7, pp. 1629–1639, 2000.

43. J. De Wit, "New knowledge on localized corrosion obtained from local measuring techniques," *Electrochimica Acta*, vol. 46, no. 24-25, pp. 3641–3650, 2001.

44. P. Visser, H. Terryn, and J. M. Mol, "On the importance of irreversibility of corrosion inhibitors for active coating protection of aa2024-t3," *Corrosion Science*, vol. 140, pp. 272–285, 2018.

45. M. Askari-paykani, M. Meratian, M. Shayan, and K. Raeissi, "Effects of heat treatment parameters on microstructural changes and corrosion behavior of al 7075 alclad alloy," *Anti-Corrosion Methods and Materials*, 2012.

46. S. Sun, Q. Zheng, D. Li, and J. Wen, "Long-term atmospheric corrosion behaviour of aluminium alloys 2024 and 7075 in urban, coastal and industrial environments," *Corrosion Science*, vol. 51, no. 4, pp. 719–727, 2009.

47. P. Visser, H. Terryn, and J. M. Mol, "Active corrosion protection of various aluminium alloys by lithium-leaching coatings," *Surface and Interface Analysis*, vol. 51, no. 12, pp. 1276–1287, 2019.

48. O. Gharbi, S. Thomas, C. Smith, and N. Birbilis, "Chromate replacement: what does the future hold?," *npj Materials Degradation*, vol. 2, no. 1, pp. 1–8, 2018.

49. P. Visser, Y. Liu, H. Terryn, and J. Mol, "Lithium salts as leachable corrosion inhibitors and potential replacement for hexavalent chromium in organic coatings for the protection of aluminum alloys," *Journal of Coatings Technology and Research*, vol. 13, no. 4, pp. 557–566, 2016.

50. P. Visser, M. Meeusen, Y. Gonzalez-Garcia, H. Terryn, and J. M. Mol, "Electrochemical evaluation of corrosion inhibiting layers formed in a defect from lithium-leaching organic coatings," *Journal of The Electrochemical Society*, vol. 164, no. 7, p. C396, 2017.

51. K. Marcoen, P. Visser, G. Trindade, M.-L. Abel, J. Watts, J. Mol, H. Terryn, and T. Hauffman, "Compositional study of a corrosion protective layer formed by leachable lithium salts in a coating defect on aa2024-t3 aluminium alloys," *Progress in Organic Coatings*, vol. 119, pp. 65–75, 2018.

52. P. Visser, K. Marcoen, G. Trindade, M. Abel, J. Watts, T. Hauffman, J. Mol, and H. Terryn, "The chemical throwing power of lithium-based inhibitors from organic coatings on aa2024-t3," *Corrosion Science*, vol. 150, pp. 194–206, 2019.

53. Y. Liu, P. Visser, X. Zhou, S. B. Lyon, T. Hashimoto, M. Curioni, A. Gholinia, G. E. Thompson, G. Smyth, S. R. Gibbon, *et al.*, "Protective film formation on aa2024-t3 aluminum alloy by leaching of lithium carbonate from an organic coating," *Journal of The Electrochemical Society*, vol. 163, no. 3, p. C45, 2015.

54. P. Visser, Y. Liu, X. Zhou, T. Hashimoto, G. E. Thompson, S. B. Lyon, L. G. van der Ven, A. J. Mol, and H. A. Terryn, "The corrosion protection of aa2024-t3 aluminium alloy by leaching of lithium-containing salts from organic coatings," *Faraday discussions*, vol. 180, pp. 511–526, 2015.

55. T. Harvey, S. Hardin, A. Hughes, T. Muster, P. White, T. Markley, P. Corrigan, J. Mardel, S. Garcia, J. Mol, *et al.*, "The effect of inhibitor structure on the corrosion of aa2024 and aa7075," *Corrosion science*, vol. 53, no. 6, pp. 2184–2190, 2011.

56. E. S. Lower, "Speciality corrosion inhibitors," *Anti-Corrosion Methods and Materials*, 1995.

57. G. Bereket and A. Yurt, "The inhibition effect of amino acids and hydroxy carboxylic acids on pitting corrosion of aluminum alloy 7075," *Corrosion Science*, vol. 43, no. 6, pp. 1179–1195, 2001.

58. A. Yurt, G. Bereket, and C. Ogretir, "Quantum chemical studies on inhibition effect of amino acids and hydroxy carboxylic acids on pitting corrosion of aluminium alloy 7075 in nacl solution," *Journal of Molecular Structure: THEOCHEM*, vol. 725, no. 1-3, pp. 215–221, 2005.

59. W. Liu, A. Singh, Y. Lin, E. E. Ebenso, L. Zhou, and B. Huang, "8-hydroxyquinoline as an effective corrosion inhibitor for 7075 aluminium alloy in 3.5% nacl solution," *Int. J. Electrochem. Sci*, vol. 9, no. 10, pp. 5574–5584, 2014.

60. W. A. Alloys, "International alloy designations and chemical composition limits for wrought aluminum and," 2015.

61. S. Tickoo, *SOLIDWORKS 2020 for Designers*. Cadcim Technologies, 2020.

62. P. H. Barry, T. M. Lewis, and A. J. Moorhouse, "An optimised 3 m kcl salt-bridge technique used to measure and validate theoretical liquid junction potential values in patch-clamping and electrophysiology," *European Biophysics Journal*, vol. 42, no. 8, pp. 631–646, 2013.

63. P. Vanysek, "Electrochemical series," *CRC handbook of chemistry and physics*, vol. 8, 2000.

64. H. P. Hack, *Galvanic corrosion*, vol. 978. ASTM International, 1988.

65. S. C. Dexter, "Galvanic corrosion," 1999.

66. R. Johnsen, "Experience with the use of copper alloys in seawater systems on the norwegian continental shelf," in *Corrosion Behaviour and Protection of Copper and Aluminium Alloys in Seawater*, pp. 62–72, Elsevier, 2007.

67. R. Shi, F. Liang, E. Lazo, and M. Kozdras, "Effect of brazing temperature on electrochemical performance and zinc diffusion of aa7072 clad in tri-layer aluminum brazing sheet aa7072/3003/4343," *SAE transactions*, pp. 859–867, 2005.

68. J. LTD., "Sem qa document," -.

69. L. Yan, Y. Zhang, X. Li, Z. Li, F. Wang, H. Liu, and B. Xiong, "Effect of zn addition on microstructure and mechanical properties of an al–mg–si alloy," *Progress in Natural Science: Materials International*, vol. 24, no. 2, pp. 97–100, 2014.

70. E. S. Skilbred, "Corrosion of nickel-aluminium bronze-how does the different alloying elements effect the corrosion properties?," Master's thesis, NTNU, 2016.

71. P. Natishan and W. O'grady, "Chloride ion interactions with oxide-covered aluminum leading to pitting corrosion: a review," *Journal of the electrochemical society*, vol. 161, no. 9, p. C421, 2014.

72. H. Tsukamoto, Y. Komiya, H. Sato, and Y. Watanabe, "Effect of compositional gradient on mechanical properties in aluminum/duralumin multi-layered clad structures," in *Micro/Nano Materials, Devices, and Systems*, vol. 8923, p. 89230Q, International Society for Optics and Photonics, 2013.

73. Z. Feng and G. Frankel, "Galvanic test panels for accelerated corrosion testing of coated al alloys: part 2—measurement of galvanic interaction," *Corrosion*, vol. 70, no. 1, pp. 95–106, 2014.

A ELECTROCHEMICAL BEHAVIOUR AA7072

As explained in Section 4.1, the electrochemical behaviour of AA7072 on both aluminium substrates appears to be slightly different. The OCP measurements are shown in Figure A.1 and the PP curves in Figure A.2. The derived values of both graphs are summarized in Table A.1.

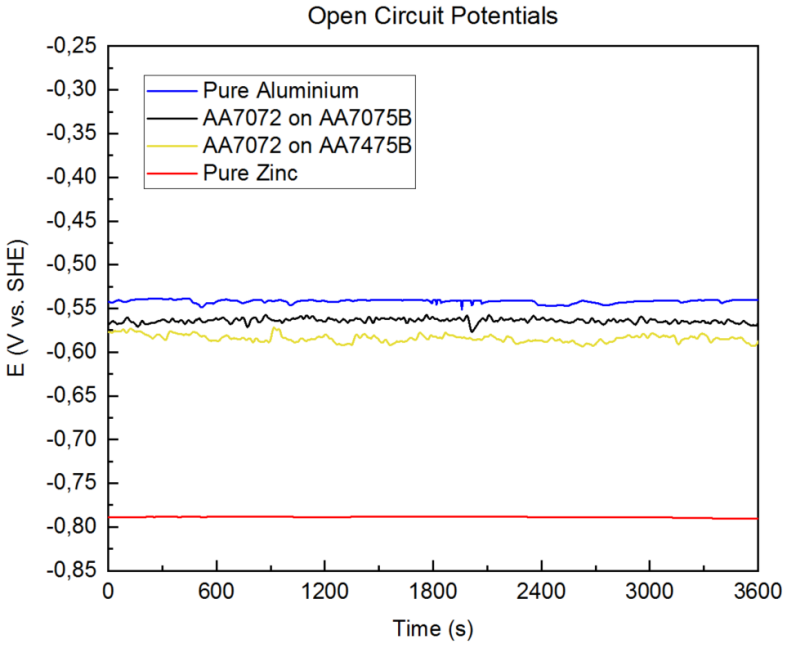

Figure A.1: Open circuit potentials of AA7072 on AA7075B, AA7072 on AA7475B, pure aluminium and zinc in 3.5% NaCl.

The OCP value measured from AA7072 on AA7075B is -0.56V, and -0.58V when AA7072 was measured on AA7475B. This means that on the exposed surface, a higher amount of anodic elements or a lower amount of cathodic elements is likely to be present in AA7072 on AA7475B. According to the line-scans performed on both alloys, an increased amount of zinc is measured close to the surface of AA7072 on AA7475B. This may be the reason for the decreased OCP value of AA7072 on AA7475B, as zinc was found to decrease the equilibrium potential of AA7072.

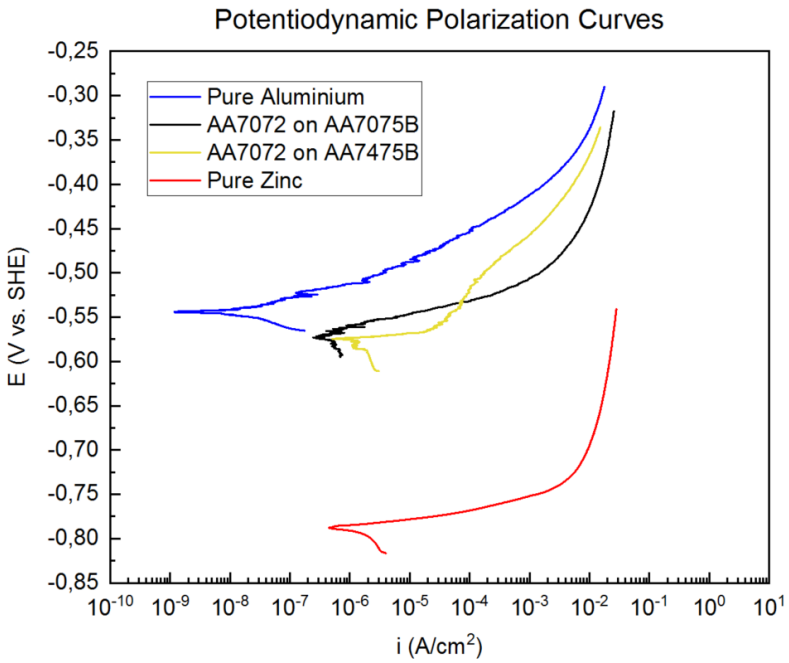

Figure A.2: Potentiodynamic polarization curves of AA7072 on AA7075B, AA7072 on AA7475B, pure aluminium and zinc in 3.5% NaCl.

The Ecorr values in the PP curves are in good agreement with the measured Eocp values. It can be observed that the current density differs with approximately a factor of 3 when comparing AA7072 on both substrates. This may also be contributed to the increased amount of zinc detected in AA7072 on AA7475B close to exposed surface. In addition, the polarization curve of AA7072 on AA7475B starts with a clear pitting behaviour and is even more active when compared to the curve of AA7072 on AA7075B. However, when a certain current density is reached, some passive behaviour can be observed. The reason for this active behaviour may be the fast dissolution of the increased amount of anodic elements such as zinc on the surface, as the curve of pure zinc shows the same active behaviour. The behaviour of pure aluminium is less active and increases more gradually. Thus, at a certain point, the anodic elements on the exposed surface can be dissolved, leaving mainly aluminium in contact with the electrolyte. This may change the anodic behaviour to a more passive behaviour as observed in the AA7072 on AA7475B curve.

Table A.1: Electrochemical parameters obtained from OCP and PP measurements with standard errors

	Eocp (V)	Ecorr (V)	icorr (A/cm^2)
Aluminium (99.99%)	-0.54 $\pm$0.01	-0.54 $\pm$0.01	2.1 $\pm$0.7 x 10^{-8}
AA7072 on AA7075B	-0.56 $\pm$0.00	-0.57 $\pm$0.00	4.8 $\pm$0.3 x 10^{-7}
AA7072 on AA7475B	-0.58 $\pm$0.00	-0.58 $\pm$0.00	1.4 $\pm$0.4 x 10^{-6}
Zinc (>99.95%)	-0.79 $\pm$0.00	-0.79 $\pm$0.00	1.7 $\pm$0.1 x 10^{-6}

B MICROSTRUCTURE AA7075B

The chemical composition of several particles on the AA7075B substrate have been investigated using SEM-EDS. The Secondary Electron Composition (SEC) image can be seen in Figure B.1 and the BEC image is shown in Figure B.2. By the detection of different electrons (e.g. secondary or backscattered), a different volume can be measured. When comparing both images on AA7075B, three different particles can be distinguished, namely:

1. Black coloured particles on the SEC image that also appear black on the BEC image (002/004/007);

2. White coloured particles on the SEC image that also appear white on the BEC image (003/005/008);

3. White coloured particles on the SEC image that turn to black on the BEC image (001/006).

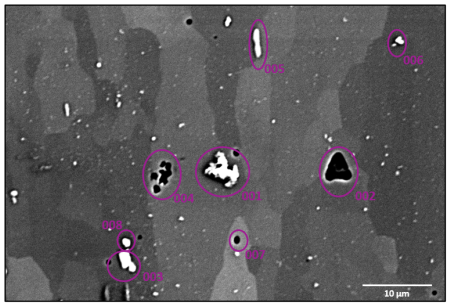

Figure B.1: SEM-EDS image in SEC mode of various particles on AA7075B.

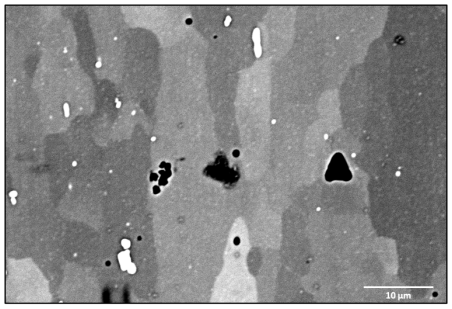

Figure B.2: SEM-EDS image in BEC mode of various particles on AA7075B.

The elements detected on the particles measured are listed in Table B.1. Particles according to number 1 appear to be oxides, with an increased amount of Mg, Si or Cu being detected. These may be second phase particles in the AA7075 substrate which have undergone corrosion [11]. Particles considering number 2 are rich in Cu and Fe, whereby no increased amount of oxygen is measured. These particles can be related to the Cu- and Fe-rich intermetallic particles in the aluminum substrate [8]. Particles at number 3 are only a combination of Si and O. Also, these particles change color when switching between the detected electrons. This suggests that these particles are on the substrate surface and may be formed during polishing by the OP-S solution.

Table B.1: Mass% of elements detected on the particles by SEM-EDS.

Particle	O(K)	Al(K)	Si(K)	Zn(L)	Mg(K)	Fe(L)	Cu(L)	Na(K)
001	16.9	70.2	9.0	3.1	0.0	0.0	0.0	0.7
002	23.3	11.8	33.7	0.0	31.3	0.0	0.0	0.0
003	0.7	45.4	0.0	0.0	0.0	22.6	31.3	0.0
004	17.4	72.1	0.8	5.6	0.0	0.0	3.6	0.5
005	0.5	66.7	0.0	3.8	0.0	23.3	5.5	0.4
006	3.8	89.7	1.5	4.1	0.0	0.0	0.0	0.9
007	8.5	73.4	7.1	3.7	6.7	0.0	0.0	0.6
008	0.7	62.7	0.0	0.0	0.0	16.4	20.3	0.0

C SEM-EDS PER POINT

The number of points per purple line correspond to the numbers of the Vlines in Figure 4.4. Table C.1 till Table C.5 are related to the linescan on AA7075C. Table C.6 till Table C.10 are the measured points of the five purple lines on AA7475C.

Table C.1: Mass% of elements detected by SEM-EDS from line 001 on AA7075C.

Line 001	O	Al	Fe	Cu	Si	Mg	Zn	Na
Point 1	0.6	91.9	0.0	0.0	0.0	2.2	4.7	0.7
Point 2	0.0	90.0	0.0	1.9	0.0	2.2	5.9	0.0
Point 3	1.2	89.7	0.2	1.7	0.0	1.9	5.3	0.0
Point 4	0.0	92.5	0.1	1.3	0.0	1.6	4.6	0.0
Point 5	0.0	94.4	1.5	0.6	0.0	0.8	2.8	0.0
Point 6	0.0	97.6	0.0	0.4	0.0	0.3	1.7	0.0
Point 7	0.9	97.8	0.0	0.0	0.2	0.0	1.2	0.0
Point 8	0.5	98.5	0.0	0.0	0.0	0.0	1.0	0.0
Point 9	0.0	99.0	0.0	0.0	0.0	0.0	1.0	0.0
Point 10	0.6	98.3	0.0	0.0	0.0	0.0	1.1	0.0

Table C.2: Mass% of elements detected by SEM-EDS from line 002 on AA7075C.

Line 002	O	Al	Fe	Cu	Si	Mg	Zn	Na
Point 1	0.5	91.8	0.0	0.0	0.0	2.4	5.4	0.0
Point 2	0.0	89.6	0.0	2.0	0.0	2.3	6.0	0.0
Point 3	0.0	93.2	0.0	0.0	0.0	2.1	4.1	0.6
Point 4	0.7	95.4	0.0	0.0	0.0	0.0	3.4	0.6
Point 5	0.5	97.0	0.0	0.0	0.0	0.0	2.2	0.4
Point 6	0.6	97.9	0.0	0.0	0.0	0.0	1.4	0.0
Point 7	0.5	98.4	0.0	0.0	0.0	0.0	1.1	0.0
Point 8	0.5	98.5	0.0	0.0	0.0	0.0	1.0	0.0
Point 9	0.5	98.5	0.0	0.0	0.0	0.0	1.0	0.0
Point 10	0.6	98.5	0.0	0.0	0.0	0.0	1.0	0.0

Table C.3: Mass% of elements detected by SEM-EDS from line 003 on AA7075C.

Line 003	O	Al	Fe	Cu	Si	Mg	Zn	Na
Point 1	0.0	92.3	0.0	0.0	0.0	2.4	5.3	0.0
Point 2	0.6	91.9	0.0	0.0	0.0	2.2	4.6	0.6
Point 3	0.7	92.7	0.0	0.0	0.0	2.0	4.0	0.6
Point 4	0.7	57.3	36.2	5.8	0.0	0.0	0.0	0.0
Point 5	0.9	96.4	0.0	0.0	0.2	0.0	2.2	0.3
Point 6	0.6	98.0	0.0	0.0	0.0	0.0	1.3	0.2
Point 7	0.5	98.4	0.0	0.0	0.0	0.0	1.1	0.0
Point 8	0.0	99.0	0.0	0.0	0.0	0.0	1.0	0.1
Point 9	0.6	98.5	0.0	0.0	0.0	0.0	0.9	0.1
Point 10	0.6	98.4	0.0	0.0	0.0	0.0	1.0	0.0

Table C.4: Mass% of elements detected by SEM-EDS from line 004 on AA7075C.

Line 004	O	Al	Fe	Cu	Si	Mg	Zn	Na
Point 1	0.5	91.8	0.0	0.0	0.0	2.3	5.4	0.0
Point 2	0.6	92.1	0.0	0.0	0.0	2.2	4.5	0.6
Point 3	0.7	92.6	0.0	0.0	0.0	2.0	4.1	0.7
Point 4	0.7	95.3	0.0	0.0	0.0	0.0	3.4	0.6
Point 5	1.9	94.9	0.0	0.0	0.7	0.0	2.2	0.3
Point 6	0.5	98.1	0.0	0.0	0.0	0.0	1.5	0.0
Point 7	0.5	98.3	0.0	0.0	0.0	0.0	1.2	0.0
Point 8	0.6	98.4	0.0	0.0	0.0	0.0	1.0	0.0
Point 9	0.6	98.4	0.0	0.0	0.0	0.0	1.1	0.0
Point 10	0.6	98.5	0.0	0.0	0.0	0.0	1.0	0.0

Table C.5: Mass% of elements detected by SEM-EDS from line 005 on AA7075C.

Line 005	O	Al	Fe	Cu	Si	Mg	Zn	Na
Point 1	0.0	92.4	0.0	0.0	0.0	2.3	5.3	0.0
Point 2	0.0	92.4	0.0	0.0	0.0	2.3	4.7	0.7
Point 3	0.5	92.7	0.0	0.0	0.0	2.0	4.3	0.6
Point 4	0.0	96.0	0.0	0.0	0.0	0.0	3.5	0.5
Point 5	0.0	97.3	0.0	0.0	0.0	0.0	2.3	0.3
Point 6	0.6	97.8	0.0	0.0	0.0	0.0	1.6	0.0
Point 7	0.5	98.4	0.0	0.0	0.0	0.0	1.1	0.0
Point 8	0.6	98.4	0.0	0.0	0.0	0.0	1.0	0.0
Point 9	0.7	98.4	0.0	0.0	0.0	0.0	0.9	0.0
Point 10	0.9	92.2	5.6	0.0	0.2	0.0	1.0	0.0

Table C.6: Mass% of elements detected by SEM-EDS from line 001 on AA7475C.

Line 001	Al	Fe	Cu	Si	Mg	Zn
Point 1	88.6	0.3	2.1	0.2	2.3	6.5
Point 2	89.4	0.0	2.0	0.0	2.3	6.3
Point 3	89.5	0.3	1.9	0.0	2.3	6.0
Point 4	89.8	0.3	2.0	0.0	2.0	5.9
Point 5	91.5	0.0	1.6	0.1	1.8	5.0
Point 6	93.1	0.2	1.0	0.1	1.4	4.2
Point 7	95.2	0.0	0.5	0.1	0.9	3.3
Point 8	96.6	0.0	0.4	0.0	0.5	2.5
Point 9	97.6	0.0	0.1	0.2	0.3	1.9
Point 10	97.9	0.3	0.0	0.1	0.1	1.5
Point 11	98.5	0.0	0.0	0.1	0.1	1.3

Table C.7: Mass% of elements detected by SEM-EDS from line 002 on AA7475C.

Line 002	Al	Fe	Cu	Si	Mg	Zn
Point 1	89.2	0.0	2.0	0.0	2.3	6.5
Point 2	89.3	0.0	2.1	0.0	2.3	6.3
Point 3	89.4	0.2	2.0	0.0	2.2	6.2
Point 4	90.5	0.0	1.8	0.1	2.1	5.6
Point 5	91.9	0.1	1.4	0.1	1.7	4.8
Point 6	93.0	0.1	1.1	0.1	1.5	4.3
Point 7	95.3	0.0	0.7	0.1	0.8	3.1
Point 8	97.0	0.0	0.2	0.0	0.5	2.3
Point 9	97.5	0.0	0.3	0.1	0.3	1.9
Point 10	98.2	0.0	0.1	0.2	0.1	1.5
Point 11	98.1	0.0	0.2	0.3	0.1	1.3

Table C.8: Mass% of elements detected by SEM-EDS from line 003 on AA7475C.

Line 003	Al	Fe	Cu	Si	Mg	Zn
Point 1	88.7	0.1	2.0	0.1	2.4	6.7
Point 2	88.8	0.0	2.1	0.1	2.5	6.6
Point 3	89.6	0.0	2.1	0.0	2.2	6.1
Point 4	90.2	0.0	1.9	0.0	2.0	5.9
Point 5	91.6	0.1	1.4	0.0	1.8	5.0
Point 6	93.2	0.0	1.1	0.1	1.4	4.1
Point 7	95.5	0.0	0.4	0.1	0.9	3.2
Point 8	97.0	0.0	0.1	0.0	0.5	2.4
Point 9	98.1	0.0	0.0	0.0	0.2	1.7
Point 10	98.1	0.0	0.1	0.1	0.2	1.5
Point 11	98.4	0.0	0.1	0.0	0.1	1.4

Table C.9: Mass% of elements detected by SEM-EDS from line 004 on AA7475C.

Line 004	Al	Fe	Cu	Si	Mg	Zn
Point 1	89.0	0.0	2.1	0.1	2.3	6.5
Point 2	89.4	0.0	2.0	0.0	2.3	6.3
Point 3	89.5	0.2	2.1	0.0	2.2	6.1
Point 4	90.9	0.1	1.6	0.0	2.0	5.4
Point 5	91.3	0.0	1.7	0.1	1.8	5.2
Point 6	93.2	0.0	1.2	0.1	1.4	4.1
Point 7	94.9	0.3	0.5	0.1	0.9	3.3
Point 8	96.4	0.2	0.3	0.2	0.5	2.5
Point 9	97.7	0.0	0.2	0.1	0.3	1.9
Point 10	98.1	0.0	0.1	0.1	0.2	1.6
Point 11	98.2	0.0	0.2	0.1	0.1	1.5

Table C.10: Mass% of elements detected by SEM-EDS from line 005 on AA7475C.

Line 005	Al	Fe	Cu	Si	Mg	Zn
Point 1	89.3	0.0	1.8	0.0	2.4	6.5
Point 2	88.6	0.0	2.1	0.7	2.3	6.4
Point 3	89.4	0.0	2.0	0.1	2.1	6.3
Point 4	90.6	0.0	1.7	0.1	2.1	5.6
Point 5	91.6	0.0	1.5	0.1	1.8	5.0
Point 6	93.5	0.0	1.0	0.1	1.4	4.1
Point 7	95.1	0.0	0.6	0.1	0.9	3.3
Point 8	95.5	0.9	0.5	0.1	0.5	2.5
Point 9	97.7	0.0	0.1	0.1	0.3	1.8
Point 10	98.3	0.0	0.0	0.1	0.2	1.4
Point 11	98.2	0.4	0.0	0.1	0.1	1.3

D COATING B AND C

The LPR measurements on the defect area per sample of Coating B and C are displayed in Table D.1. On average, it can be established that the polarization resistance measured on Coating C is sightly higher than on Coating B on both aluminium alloy substrates. When observing at all individual measurements, it becomes clear that the resistance range of both coatings fluctuates and overlaps. This means that, on average, Coating C appears to be more effective in the inhibition of the defect area, but that individual measurements clearly show that Coating B appears to have a higher polarization resistance in several cases than Coating C. Therefore, an unambiguous conclusion cannot be drawn about which coating performs in general better according to the LPR and EIS measurements. Only that a higher resistance is measured for both coatings than measured in the reference measurements. The subsequent EIS curves are in good agreement with the LPR values.

Table D.1: Linear Polarization Resistance values of Coating B and C on AA7475C.

Material	Coating	Average LPR	sample	LPR (ohms*cm^2)
AA7075C	B	2.2 x 10^4	1	9.4 x 10^3
			2	1.5 x 10^4
			3	1.0 x 10^4
			4	5.4 x 10^4
	C	3.6 x 10^4	1	6.5 x 10^4
			2	3.3 x 10^4
			3	1.4 x 10^4
			4	3.2 x 10^4
AA7475C	B	5.2 x 10^4	1	3.7 x 10^4
			2	3.7 x 10^4
			3	1.0 x 10^5
			4	3.5 x 10^4
	C	6.5 x 10^4	1	1.6 x 10^5
			2	2.0 x 10^4
			3	2.1 x 10^4

COLOPHON

This document was typeset using LaTeX. The document layout was generated using the arsclassica package by Lorenzo Pantieri, which is an adaption of the original classicthesis package from André Miede.